The Henryk Niewodniczański
Institute of Nuclear Physics
Polish Academy of Sciences
ul. Radzikowskiego 152, 31-342 Kraków

From Classical to Plasma Tomography

Jakub Bielecki

Habilitation dissertation

Table of Contents

Glossary

AIC	Akaike Information Criterion
ART	Algebraic Reconstruction Technique
BP	Back-Projection
BPF	Back-Projection Filtering
CBP	Convolution Back-Projection
CC	Charge Comparison
CPU	Central Processing Unit
CT	Computed Tomography
DAQ	Data Acquisition System
DEMO	Demonstration Power Station
DT2	2nd Deuterium-Tritium Campaign
EC	Electron Cyclotron
ECHR	Electron Cyclotron Resonance Heating
ENIAC	Electronic Numerical Integrator and Computer
FBP	Filtered Back-Projection
FDK	Feldkamp, Davis, Kress
FIR	Far Infrared
FoV	Field of View
FPGA	Field Programmable Gate Array
FW	Fast Wave (magnetosonic wave)
GA	Genetic Algorithms
GCV	Generalised Cross-Validation
GPU	Graphics Processing Unit
GSS	Golden Section Search
GSVD	Generalised Singular Value Decomposition
HFS	High Field Side
HRTS	High Resolution Thomson Scattering
HSX	Helically Symmetric Experiment
HXR	Hard X-Ray
ICF	Inertial Confinement Fusion
ICRH	Ion Cyclotron Resonance Heating
IFFT	Inverse Fast Fourier Transform
ITER	International Thermonuclear Experimental Reactor
JET	Joint European Torus

Glossary

LH	Lower Hybrid
LHCD	Lower Hybrid Current Drive
LHD	Large Helical Device
LIDAR	Light Detection and Ranging
LoS	Line of Sight
LU	Lower Upper (decomposition)
MC	Monte Carlo
MCF	Magnetic Confinement Fusion
MCNP	Monte Carlo N-Particle Transport Code
MFI	Minimum Fisher Information
MHD	Magnetohydrodynamics
MPPC	Multi-Pixel Photon Counters
MRI	Magnetic Resonance Imaging
NBI	Neutral Beam Injection
NIF	National Ignition Facility
PRESS	Predicted Residual Error Sum of Squares
PET	Positron Emission Tomography
PF-24	Plasma Focus PF-24 device
RF	Radio-Frequency
RMS	Root Mean Square
SART	Simultaneous Algebraic Reconstruction Technique
SIRT	Simultaneous Iterative Reconstruction Technique
SPECT	Single-Photon Emission Computed Tomography
SVD	Singular Value Decomposition
SW	Slow Wave
SXR	Soft X-Ray
TFTR	Tokamak Fusion Test Reactor
TR	Tikhonov Regularisation
WEST	W Environment in Steady-state Tokamak

List of Symbols

ω	Angular wave frequency	$\mathbf{B}$	Magnetic field
A_i	Atomic mass of a species i	R	Major radius of a tokamak
J_m	Bessel functions of the first kind	m_s	Mass of species s
q_s	Charge of species s	a	Minor radius of a tokamak
$v_{\parallel}$	Component of the ion velocity parallel to the magnetic field	P_m	Mutation probability in the GA-based method
$k_{\parallel}$	Component of the wave vector parallel to the magnetic field	ω_{pe}	Natural plasma electron angular frequency
Z_e	Effective ionic charge of plasma	ω_{pi}	Natural plasma ion angular frequency
$\mathbf{E}$	Electric field	l	Noise level
ω_{ce}	Electron cyclotron angular frequency	N_H	Number of discrete elements of the reconstructed function in the horizontal direction
$\tilde{P}_\theta(s)$	Filtered projection at angle θ		
$f_{BPF}(x,y)$	Function $f(x,y)$ reconstructed using the back-projection filtering method	N_V	Number of discrete elements of the reconstructed function in the vertical direction
$f_{BP}(x,y)$	Function $f(x,y)$ reconstructed using the back-projection method	N_d	Number of lines of sight (detectors)
$f_{CBP}(x,y)$	Function $f(x,y)$ reconstructed using the convolution back-projection method	f_{obj}	Objective function
		I_p	Plasma current
$f_{FBP}(x,y)$	Function $f(x,y)$ reconstructed using the filtered back-projection method	n_e	Plasma electron density
		T_e	Plasma electron temperature
$f(x,y)$	Function to be reconstructed	n_i	Plasma ion density
$\mathbf{W}$	Geometrical (contribution, weighting) matrix	T_i	Plasma ion temperature
C_H	Height of a random block for cross-over operation in the GA-based method	ϵ_p	Plasma permittivity tensor
		M	Population size in the GA-based method
ω_{ci}	Ion cyclotron angular frequency	$P_\theta(s)$	Projection at angle θ
ρ_L	Larmor radius of ions	Q	Ratio between the energy released from plasma to the energy delivered into plasma
p	Line integral		

List of Symbols

λ	Regularisation parameter
c	Speed of light in vacuum
C_s	Start point of a random block for cross-over operation in the GA-based method
S_r	Survival rate in the GA-based method
$\mathscr{A}$	The Abel transform
$\mathscr{F}$	The Fourier transform
$\mathscr{R}$	The Radon transform
τ_e	Thermal energy confinement time
T	Threshold value (in convergence criterion)
N_p	Total number of elements for the discrete representation of the neutron emissivity
$\mathbf{p}$	Vector representing the available data along lines of sight (projections)
$\mathbf{k}$	Wave vector
C_W	Width of a random block for cross-over operation in the GA-based method

List of Figures

List of Figures

List of Figures

List of Figures

List of Tables

1. Preface

This monograph is an attempt at a comprehensive treatment of tomographic reconstruction methods with the special emphasis on the application in fusion research. Therefore, the main volume of the book is devoted to tomographic inversion methods that are either commonly used in the fusion research or they have just been developed and published by me or other researchers. However, detailed explanation and discussion of plasma tomography principles would not have been possible without giving an introduction to classical tomographic reconstruction methods. By these classical methods, I mean here analytical and algebraic methods commonly applied not only in medicine but also in many different fields such as geophysics, bioscience or material science.

Inversion methods applied in plasma tomography significantly differ from classical ones. This is mostly due to the nature of the data collected in tomographic experiments carried out with fusion devices. The algebraic reconstruction method, shortly described in Chapter 5, can be considered as a link between classical tomographic methods described in the preceding part of the book and reconstruction methods that are specific to fusion research. In fact, most of the reconstruction methods used in fusion science belong indeed to the class of algebraic methods. However, due to the fact that measured data sets are sparse and the reconstruction problem is strongly ill-posed, specific methods that include a regularisation are required. This is shown and discussed in Chapter 6.

My main motivation in publishing this work was a desire to share, with the widest possible readership, a comprehensive monograph on plasma tomography. I would expect the target audience to be primarily academics, with a special emphasis on graduate and PhD students from plasma physics and fusion research community. I hope that this book can serve as a self-contained resource for PhD students wishing to extend their knowledge on plasma tomography. I tried to present as many practical applications as possible, focusing mostly on the recent advances made with tokamak devices.

I assume the Reader is familiar with the basic concepts of plasma physics and thermonuclear fusion, as well as with basic mathematical apparatus such as linear algebra. The introductory chapters and proofs of presented theorems should help the Reader to immerse into the ideas presented through the book. For the sake of clarity, some detailed information and additional proofs are postponed to the appendices.

Preparing this monograph, I used my knowledge and experience acquired during my work in the Department of Radiation Transport Physics of the Institute of Nuclear Physics, Polish Academy of Sciences as well as the experience gained during my two-year-long stay in the Culham Centre For Fusion Energy (CCFE), Oxfordshire UK.

I would like to express my gratitude to the many people who helped me through this book - to all those who provided support and offered comments, allowed me to quote their remarks and assisted in the editing, proofreading and design. I would like to kindly thank my colleagues from Department of Radiation Transport Physics, IFJ PAN and colleagues from Neutron&Gamma group, CCFE. I would like to thank especially Prof. U. Woźnicka, Prof. K. Drozdowicz and Prof. W. Królas for their invaluable support and precious guidance. I would like to kindly thank Prof. M. Scholz for many long hours of scientific discussions. Last but not least, I am also very grateful for the wonderful editorial support and guidance I received from dr hab. Janusz Lekki. Above all however, I want to thank My Family which supported and encouraged me in spite of all the time it took me away from them.

2. A brief history of computed tomography against developments in fusion plasma physics

Tomographic methods and fusion science have been developing in parallel. Undoubtedly the most important event in history of tomography was the invention of the computed tomographic (CT) scanner. It was done by Sir Godfrey Newbold Hounsfield in year 1968 as a prototype device and introduced into medical practice in 1971. Independently, Allan MacLeod Cormack worked on the theoretical aspects of tomographic inversion from projections obtained with X-rays. The developed techniques were practically applied using an experimental device constructed by himself. The results of his work were published in 1963 in Journal of Applied Physics [Cormack 1963] and later in Physics of Medical Biology Journal [Cormack 1973]. In 1979 Hounsfield and Cormack received the Nobel Prize in Physiology or Medicine. However, construction of the medical CT scanner would not have been possible without the contribution of many researches from several different fields, such as mathematics, physics or computer science. In fact, discoveries made in those fields are intertwined with advances in computed tomography. Thus, to discuss the history of CT it is necessary to provide at least a brief but more general overview of this scientific puzzle.

The description of mathematical backgrounds of a function reconstruction from its projection can be traced back to work of Norwegian mathematician Niels Henrik Abel. In his paper from 1823 and its continuation from year 1826, he considered the problem of determination of the shape of a hill from travel time that a material point spends to move from the hill in the gravitational field. The problem is a generalisation of the tautochrone problem solved earlier by Christiaan Huygens. By this problem Abel was led to an integral transform – the so-called Abel transform – which is used also nowadays for the inversion of neutron or X-ray plasma emissivity from its projection when spherical or cylindrical symmetry can be assumed. The Abel transform is described in details in Section 4.5 of this book. An extension of Abel's idea was the Radon transform introduced in 1917 by an Austrian mathematician Johann Radon. The Radon transform is, similarly to Abel's one, an integral transform. It takes an arbitrary function on the plane to a two dimensional function defined on the space of lines in the plane, which value at the particular line is given by the line integral of the function over that line. A formal definition of the Radon transform is given in Section 4.3. Even by intuition it is easy to link this transform to the phenomenon of image creation on X-ray sensitive films when an object is exposed to radiation. Radon also provided a formula for the inverse transform and generalised

the problem to three dimensions. It should be stressed here that the Radon transform is the basis for most of the modern tomographic methods used in medical CT.

Physical background, not only for the construction of the CT scanner and development of tomographic methods but also for broadly defined medical imaging, was created with discovery of X-ray by Wilhelm Conrad Röntgen in 1895. However, it is interesting to note that for the first time X-rays were used for an industrial and not medical application, as Röentgen produced a radiograph of a set of weights in a box to show it to his colleagues. The news of Röntgen's discovery immediately aroused an immense interest in the public and also initiated intense research in several directions. Physicians and physicists began, as early as January 1896, to use X-rays on patients to investigate the skeleton and subsequently the lung and other organs. This was the birth of radiology. In 1901 Röntgen was awarded the very first Nobel Prize in Physics. The award was officially *in recognition of the extraordinary services he has rendered by the discovery of the remarkable rays subsequently named after him*. X-rays and radioactivity were at the origin of the scientific revolution at the end of the 19th and the beginning of the 20th centuries. Over the years more advanced X-ray sources were used for imaging of the human body. The significant improvements of the X-ray tube design are attributed to Thomas Edison. The initial enthusiasm about the new possibilities of X-ray application in medical diagnostics was gradually cooled down when physicians and researchers realised limitations of the two-dimensional imaging. Just a year after the discovery of X-rays by Röntgen, Elihu Thomson from General Electric proposed stereoscopy. The technique he proposed involved taking two X-ray pictures, displaced with respect to each other, of a patient who remained motionless. The diagnostician could then use a stereoscope to view both the images simultaneously to give a depth perspective. The significant contribution to the improvement of X-ray imaging techniques was also made by a Polish researcher from the Krakow Clinic of Internal Medicine - Dr Karol Mayer. In 1916 he performed several experiments to obtain stratigraphic images using a moving X-ray tube and a stationary film cassette. This was a process which resembles scanning in computed tomography procedure. A similar imaging procedure was also described and patented earlier in 1915 by Carlo Baese, an engineer from Florence. The technique proposed by Baese was based on the simultaneous movement of the tube and X-ray film cassette. In 1922 A.E.M. Bocage obtained a patent entitled *Methods and equipment for obtaining radiological images of cross-sections of the body not obscured by tissue structures in front of or behind the cross-section*. During the same period, B.G. Ziedses des Plantes conducted research into his concept of planigraphy, which was put into practice by Massiot in 1935. Later in 1963 a German doctor Willy Kuhn used gamma radiation to obtain a sliced image of tissues, but the way to modern tomographic scanners was still unreachable due to lack of a computing machine.

The complete description of history of computer development is definitively beyond the scope of this book. The reader may wish to refer to other publications for more details

[Ceruzzi 2003]. The mathematical foundations of modern computer science began to be laid by Kurt Gödel with his incompleteness theorem published in 1931. In this theorem, he showed that there were limits to what could be proved and disproved within a formal system [Gödel 1931]. In 1935, at Cambridge University, Alan Turing created the principle of the modern computer. He described an abstract digital computing machine consisting of a limitless memory and a scanner that moves back and forth through the memory, reading, symbol by symbol, what it finds and writing further symbols [Turing 1936]. The actions of the scanner are dictated by a program of instructions that is stored in the memory in the form of symbols. It was Turing's revolutionary concept of stored-program that gives a possibility of the machine to modify its own program. Today the concept is known as the universal Turing machine. In the United States the Hungarian-American mathematician John von Neumann shared Turing's dream of building a universal stored-program computing machine. Von Neumann had learned of the universal Turing machine before the war. He and Turing came to know each other during years 1936-1938, when they both were working at Princeton University. Von Neumann contributed to a new understanding of how practical and fast computers should be organised and built, giving principles for future generations of high-speed digital computers.

The first officially recognised programmable electronic computer was built at the Moore School at the University of Pennsylvania. It was called the Electronic Numerical Integrator and Computer - ENIAC. The project of creation of the computing machine started in 1943 and stemmed from military needs - fast calculation of firing tables for artillery. One of the first ENIAC programs also included a study of the feasibility of the thermonuclear weapon. ENIAC was completed in 1945 and ran approximately 200% over budget. However, in reality, the first computer was built three years earlier. It was constructed during the war at the Bletchley Park centre by a group of telephone engineers under the direction of Max Newman. The existence of the computer, called Colossus I, was kept secret until 1976. Just to give the impression of the technology from that time let us recall some facts. ENIAC consisted of 40 panels and weighed approximately 30 tons. It was programmed manually by setting thousands of switches by hand. ENIAC could not store programs or data, and problems had to be solved in stages, with the results punched on cards that were fed back. It was extremely unreliable machine in today's meaning - longest continuous period of operation without a failure was 116 hours. The average mobile phone is roughly 40 000 000 times smaller, 120 000 times lighter and consumes 40 000 times less power than ENIAC. And even though the direct comparison is very difficult, the average mobile phone would be probably thousands times more powerful than ENIAC. But none of today's electronic technology would have appeared without its contribution.

The further development of computing machines was stimulated by invention of the transistor by William Shockley, John Bardeen and Walter H. Brattain of Bell Laboratories in 1948 and the integrated circuit at Intel under the direction of Ted Hoff in 1969.

In parallel, the first computer languages appeared. In 1953 Grace Hopper developed the first computer language, which eventually became known as COBOL and in 1954 the FORTRAN programming language was born. Hounsfield first research prototype CT scanner, constructed in 1967, required nine days to obtain the data and two and a half hours to compute the image. The resolution of the image was as low as 80 × 80 pixels. Hounsfield used algebraic techniques, described in Chapter 5. The reconstructed CT image was noisy and affected by artefacts. The further development in reconstruction algorithms resulted in application of convolution back-projection algorithms (see Section 4.11) created by Ramachandran and Lakshminarayanan [Ramachandran 1971] and later popularised by Shepp and Logan [Shepp 1974]. The class of back-projection methods is described in Chapter 4. Back-projection algorithms considerably reduced the reconstruction time and gave more accurate results. By 1972, when Hounsfield introduced its first generation commercial prototype head scanner, scanning speed had been reduced to five minutes and the reconstruction time to 20 seconds. Since that time, an enormous progress in radiation sources and detection systems has been made.

Gradually, digital computers became powerful enough to store and display digital images. Since the 1990s, computerised radiography and digital radiography have been replacing X-ray films. Further development of X-ray imaging was stimulated by utilisation of synchrotron radiation. At first, synchrotron radiation was treated as a parasitic effect. The first accelerators were built by particle physicists in the 1930s. They were used in the field of high-energy or nuclear physics. Synchrotron radiation was seen for the first time at General Electric in the United States in 1947 in a new, at that time, type of particle accelerator - synchrotron. The observation of the synchrotron radiation was first considered as a drawback for nuclear experiments since it caused the particles to lose energy that was so precious to discover new particles and phenomena. However, it was then recognised in the 1960s as light with exceptional properties that overcame the shortcomings of the known X-ray sources such as X-ray tubes. In the mid- to late 1970s, scientists began to discuss ideas for using synchrotrons to produce extremely bright X-rays. These discussions led to the construction of the so-called second-generation synchrotrons dedicated solely to the production of electromagnetic radiation. It was followed by third-generation synchrotrons that use insertion devices - wigglers and undulators providing several orders of magnitude higher flux than simple bending magnets. Impressive progress continues with the development and construction of free electron lasers with the peak brilliance of billions times higher than that of conventional X-ray sources. Computed micro- and nano-tomography techniques that utilise synchrotron radiation are nowadays almost standard experimental tools for scientist from diverse fields such as physics, medicine, bioscience, geoscience and material science.

When the dream about the practical tool capable of giving non-destructive insight into the human body and other structures was coming true, another scientific challenge appeared. People have always been dreaming about an energy source that is practically

inexhaustible, relatively cheap, producing low or no radiation or environmental hazard and capable of producing large amount of energy in a stable fashion. Such possibilities could be opened by nuclear fusion - a nuclear reaction in which light elements form heavier elements. At the beginning of 20th century scientists obtained the first insights into the physics of sunshine. When the Sun and other stars transmute matter, tirelessly transforming hydrogen into helium by the process of fusion, they release colossal amounts of energy. Einstein provided the first clues on how the Sun works in 1905 with his famous equation derived from his special theory of relativity. The equation predicted that the conversion of a small amount of mass could yield a very large amount of energy with the conversion factor being the square of the speed of light. The key experimental observation was made in 1920 by British chemist Francis William Aston who took precise measurements of the masses of atoms. This work was seized upon by Sir Arthur Eddington, a British astrophysicist, who realised that by fusing hydrogen into helium, the Sun would release around 0.7% of the mass into energy. In 1939, German physicist Hans Bethe completed the picture with a quantitative theory explaining the generation of fusion energy in stars. Having an access to similar energy system would be like bringing the Sun down to earth to provide abundant energy for millions of years. The world scientific community is convinced that fusion power can be achieved in the relatively not too distant future. However, nuclear fusion represents the frontier of today's science and technology.

On the Sun - a large fusion power reactor - the nuclei of atoms are fused as they are compressed together by the force of the Sun's gravity. On Earth however, the same process must be achieved using a similar ionised gas called plasma that makes up the Sun, but without the benefit of the huge gravitational force. This is due to negligible mass of plasma that we are able to use in the experiments on earth, compared to mass of the Sun. Plasma must be confined and simultaneously heated to very high temperatures. There are two schools of plasma confinement – using magnetic fields or the internal force of powerful beams like lasers. In the latter case plasma must be compressed to extreme density. In this book we will focus mostly on magnetically confined plasma, since such a long-living plasma requires special diagnostics and tomographic methods are very useful in this case.

In early stages, fusion research was kept secret. That was because of the military significance of an uncontrolled fusion device – the H-bomb. In 1952, the United States tested the world's first H-bomb which was soon thereafter detonated also by the Soviet Union. However, three years earlier, in 1950 Igor Kurchatov, director of the Soviet weapon program, convinced Soviet leaders that significant resources should be devoted to the development of controlled fusion energy. In the United States the work on the same problem begun under the leadership of Edward Teller and others. In 1956 a turning point came. A Soviet Union delegation led by First Secretary of Soviet Communist Party - Nikita S. Khrushchev, Prime Minister of the USSR - Nikolai A. Bulganin and

Igor Kurchatov visited the United Kingdom. On April 25, Kurchatov gave a lecture at Harwell located just nearby today's Culham Science Centre in Oxfordshire. At that time Harwell was the leading research centre of the UK's Atomic Energy Research Establishment. He presented the full experimental and theoretical details of the Soviet fusion research to an audience of western scientists. A similar declassification came a few months later with the lecture of a Soviet academician L. Artsimovich given to an audience in Stockholm. Partly under the influence of the openness of Kurchatov's lecture, in early 1957 the UK decided to declassify thermonuclear research. Also significant parts of the US program were declassified and made public. It can be frankly said that Kurchatov and Artsimovich's presentations accelerated fusion research program in the West. Among the presented information was the concept of Soviet fusion device – tokamak (rus. тороидальная камера с магнитными катушками — toroidal chamber with magnetic coils). In the late 1940s, Soviet researcher Andrei Sakharov proposed that fusion plasma can be confined in a doughnut-shaped vessel by magnetic fields. In this geometry, an electrical current is induced in the plasma to transform the circular magnetic field into helical spirals winding around plasma doughnut. Initially, the Soviet scientists struggled with the presence of impurities in the plasma (by the way, even now it is still a significant issue for the fusion device operation). Finally, in 1969 the Soviet tokamak research program achieved a major success in plasma heating. At first Soviet reports on the achieved plasma temperature were taken with a pinch of salt in the West. The situation changed when a team of British scientists invited to USSR used advanced laser techniques and found that the tokamak was producing even higher temperatures than originally stated.

Another leading concept of magnetic confinement fusion (MCF) is the stellarator device. It was invented by Lyman Spitzer in 1958 and built the next year at what later became the Princeton Plasma Physics Laboratory. It is somehow similar to the tokamak device. The stellarator is also a doughnut-shaped magnetic 'plasma container', but the helical twist in the magnetic field lines is not generated by introducing an electrical current in the plasma, as in the tokamak device. Instead, required twist to the magnetic field lines is achieved solely with external coils. Even though the magnet coils and plasma itself have a complicated shape, there is a major advantage of this design. The tokamak's induced current is exhausted within minutes, requiring a pulse-mode operation. In a stellarator, the magnetic cage is produced with a single coil system, without a longitudinal net-current in the plasma and hence without a transformer. This makes stellarators suitable for continuous operation. Technical difficulties prevented the construction of large-scale stellarators in the 1950s and 1960s. Much better results from tokamak devices led to them falling from favour in the 1970s. In the 1990s interest in the stellarator design reappeared, and a number of new devices have been built. Some important modern stellarator experiments are Wendelstein 7-X in Germany, the Helically Symmetric Experiment (HSX) in the USA, and the Large Helical Device (LHD) in Japan.

In the 1970s the construction of large-scale tokamaks was approved, including a European collaboration to build the biggest machine to date – the Joint European Torus (JET). In the 1980s, Soviet general secretary Mikhail Gorbachev proposed to US president Ronald Reagan that the superpowers might collaborate to build ITER - The International Thermonuclear Experimental Reactor. In the 1990s, however, policy-makers' enthusiasm for grand energy research projects wavered against a background of sustained low oil prices. A key step was taken in November 2006 when a much-revised ITER plan was finally agreed as a seven-party international collaboration (EU, China, India, Japan, Russia, South Korea and the US). Construction of the ITER Tokamak complex started in 2013.

Experiments with actual fusion fuel - a mix of the hydrogen isotopes - deuterium and tritium – began in the early 1990s in the Tokamak Fusion Test Reactor (TFTR) in Princeton, US, and the Joint European Torus (JET) in Culham, UK. JET marked a key step in international collaboration, and in 1991 achieved the world's first controlled release of fusion power. Three tokamak devices played a special role in history of modern fusion research. They are: Japan Atomic Energy Research Institute Tokamak-60 (JT-60) in Naka, Japan (1985 to present), Tokamak Fusion Test Reactor in Princeton, New Jersey, US, (1982–1997) and aforementioned Joint European Torus JET in Culham UK (1984 to present). Together these three machines have demonstrated the scientific fundamentals of fusion power production. Researchers at JT-60 (and latter at Tore Supra and WEST tokamak) demonstrated that it should be possible to extend the duration of tokamak discharge by means of an external current drive. This would be an important step towards continuous electricity generation. In JET, TFTR and JT-60 scientists have approached the long-sought 'break-even point', where a device releases as much energy as it is required to produce fusion. So far, JET has achieved the highest level of fusion energy production (Figure 2.1). In 1997, JET produced around 64% of the amount of energy being fed into the plasma (denoted by $Q = 0.64$) [Dickson 1997]. This refers to the total energy released by the reaction, 4/5 of which is taken up by the emitted neutrons, providing the heat for electricity generation. Only when the plasma reactions release five times more of energy that is put in ($Q > 5$), the internal heating power is greater than the supplied power. Clearly a power station needs to produce vastly more energy than it consumes (e.g. $Q \sim 50$). ITER's objective is to release 10 times as much energy as it will use to initiate the fusion reaction ($Q = 10$). For 50 MW of input power, ITER will generate 500 MW of output power. ITER will pave the way for the Demonstration Power Plant (DEMO). As research continues in other fusion installations worldwide, scientists hope that DEMO will put fusion power into the grid by the end of this century.

In late 80s tomographic inversion and fusion research converged into a powerful tool. Since then tomography inversion has been used routinely for studying of plasma radiation. Various tomographic algorithms have been developed, with those based on Tikhonov regularisation being among the fastest while still providing reliable results [Bielecki 2015]. In tokamak plasma research, the soft X-ray (SXR) tomography has been used

for investigating plasma shape and physical processes occurring inside the plasmas. The X-ray tomography also allows access to the spatio-temporal transient phenomena due to magnetohydrodynamic (MHD) activities, which play an important role in plasma confinement. Hard X-ray tomography has been used to study the high-energy tail of the electron distribution function in a thermonuclear plasma. Studying this tail is of particular interest when the electron distribution function is non-Maxwellian. Tomographic reconstruction of plasma emission in the hard X-ray (HXR) energy range, which corresponds to the domain of acceleration of the energetic electrons by radio frequency waves (so-called Lower Hybrid (LH) or Electron Cyclotron (EC) plasma heating), provides also a considerable insight on the wave propagation and absorption [Peysson 2001]. Neutron plasma tomography is a useful technique for localisation of a plasma axis, study of the response to MHD plasma instabilities and determination of plasma total neutron yield and alpha-particle birth profile. Other types of plasma tomographic inversion, commonly applied at tokamak devices, include bolometry [Konoshima, 2001] and visible light computerised tomography [Goswami 2014].
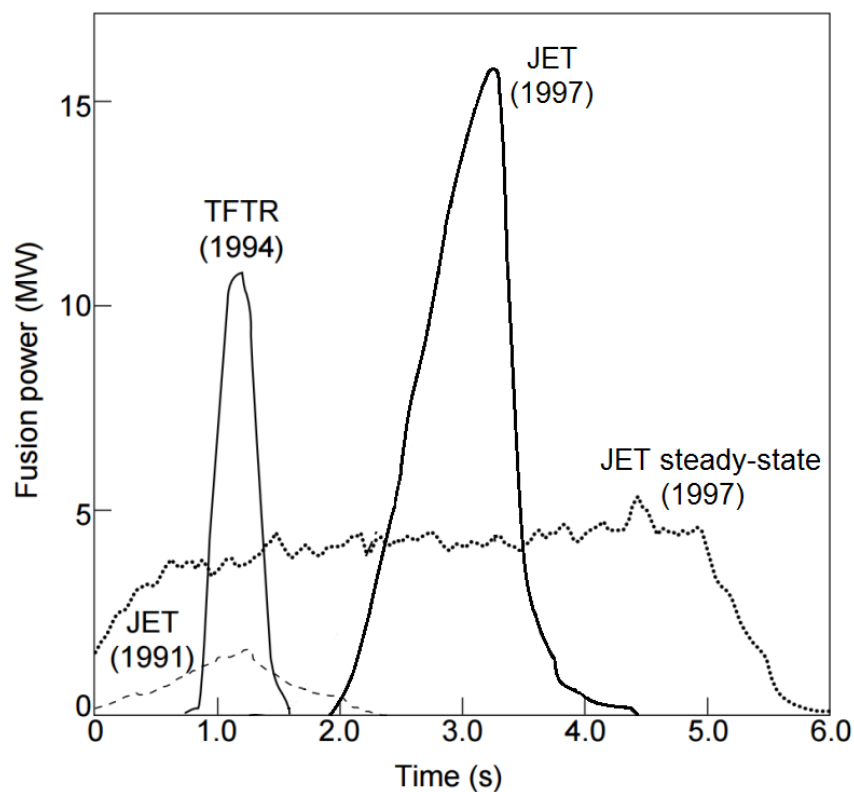
Figure 2.1 Time trace of the record fusion power achieved at JET in 1997 (Q ≈ 0.64) and the power achieved during steady-state operation in 1997. For comparison, time traces of the record fusion power achieved at TFTR tokamak in 1994 and during the JET operation in 1991 are also plotted [Ongena 2016].

3. Various types of tomography

Since the appearance of computed tomography, it has been playing an important role in many research fields. Originating from the medical field, CT has been gradually introduced in various applications, evolving and adapting to scientific problems. Currently, tomographic methods are used for imaging of various objects and structures which dimensions can span over several orders of magnitude. Different physical phenomena are utilized in different types of tomography. The variety of CT types used in modern science is so large that it is difficult to provide a systematic classification. Moreover, the division of CT methods can be multifaceted. During the last decade, there has been an avalanche of publications on different aspects of computed tomography. Table 3.1 summarizes commonly applied types of tomographic techniques providing relevant references. The list however is by no means exhaustive and each position could be a topic of a separate monograph.

Very generally, tomographic methods can be divided into transmission and emission techniques. In transmission tomography, an external source (typically of radiation, such as X-rays or neutrons, but also of ultrasound wave, electrical current etc.) of known intensity and location is used. The radiation is transmitted through the object to measure its attenuation or scattering properties. For instance, in the absorption X-ray CT, dense materials such as bones have higher attenuation coefficient than soft tissue. In this case, the quantity of interest is the spatial distribution of linear attenuation coefficient at some energy or range of energies. In transmission tomography different shapes of the incident radiation beam can be used. On this basis, we can distinguish between pencil-, parallel-, fan- or cone-beam geometry. A schematic comparison of these geometrical configurations is shown in figure 3.1. The tomographic reconstruction algorithms must take into account these geometrical aspects. In case of pencil- and planar fan-beam geometry, an additional scanning with the object (or equivalently with the source and detector) is needed. The modification of classical CT is the microtomography method that allows imaging of objects with very fine spatial resolution. More details about this method can be found in a series of publications [Bielecki 2013; Bielecki 2012; Bielecki 2009]. Microtomography (as well as submicro- and nano-imaging) very often utilizes synchrotron radiation due to its advantageous properties such as high intensity, high collimation and adjustable monochromatic energy spectrum when a tunable monochromator is applied [Bielecki 2013].

Table 3.1. Common types of tomographic techniques

Name	Physical phenomenon	Physical quantity measured	Scientific disciplines	Transmission /Emission	References
X-ray absorption CT	X-ray absorption	Linear attenuation coefficient for X-rays	Medicine	Transmission	[Kak 2001]
X-ray absorption microtomography	X-ray absorption	Linear attenuation coefficient for X-rays	Various (geophysics, biology, material science, archaeology, cultural heritage etc.)	Transmission	[Bielecki 2013] [Bielecki 2012] [Bielecki 2009]
Neutron tomography	Absorption of thermal neutrons	Linear attenuation coefficient for thermal neutrons	Various (wood- and soil-physics, geology material science, paleontology, archaeology and cultural heritage, nuclear technology etc.)	Transmission	[Anderson 2009]
Positron Emission Tomography	Positron annihilation	Gamma ray emissivity from electron-positron annihilation	Medicine	Emission	[Waterstram-Rich 2016] [Wernick 2004]
Single photon emission tomography	Gamma ray emission	Gamma ray emissivity of gamma-emitting radioisotope	Medicine	Emission	[Wernick 2004]
Magnetic resonance tomography	Nuclear magnetic resonance	Nuclear magnetic moment	Medicine	Emission/ transmission	[Bushong 2014] [Hashemi 2003] [Westbrook 2011]
Electrical resistivity tomography	Electric current	Electrical resistivity	Geophysics	Transmission	[Perrone 2014]
Electrical impedance tomography	Electric current	Electrical conductivity, electrical permittivity, electrical impedance	Medicine	Transmission	[Brown 2003]
Ultrasound tomography	Propagation, reflection and attenuation of ultrasound waves	Ultrasound attenuation coefficient, speed of sound (from time-of-flight measurements)	Medicine	Emission	[Gemmeke 2007]
Electron tomography	Electron attenuation and scattering	Electron attenuation coefficient	Nanoscience, biology, material science	Transmission	[Ercius 2015]
Plasma soft X-ray tomography	Plasma X-ray emission	X-ray emissivity	Plasma physics, thermonuclear fusion	Emission	[Anton 1996] [Granetz 1988] [Granetz 1985]
Plasma hard X-ray tomography	Plasma X-ray emission	X-ray emissivity	Plasma physics, thermonuclear fusion	Emission	[Peysson 2001] [Gnesin 2008]
Plasma neutron tomography	Plasma neutron emission	Neutron emissivity	Plasma physics, thermonuclear fusion	Emission	[Bielecki 2015] [Craciunescu 2008]
Plasma gamma-ray tomography	Plasma gamma emission e.g. from deuterons or alphas reactions with plasma impurities	Gamma emissivity	Plasma physics, thermonuclear fusion	Emission	[Kiptily 2006]
Plasma bolometry	Plasma radiative energy loss	Radiated power	Plasma physics, thermonuclear fusion	Emission	[Konoshima 2001]
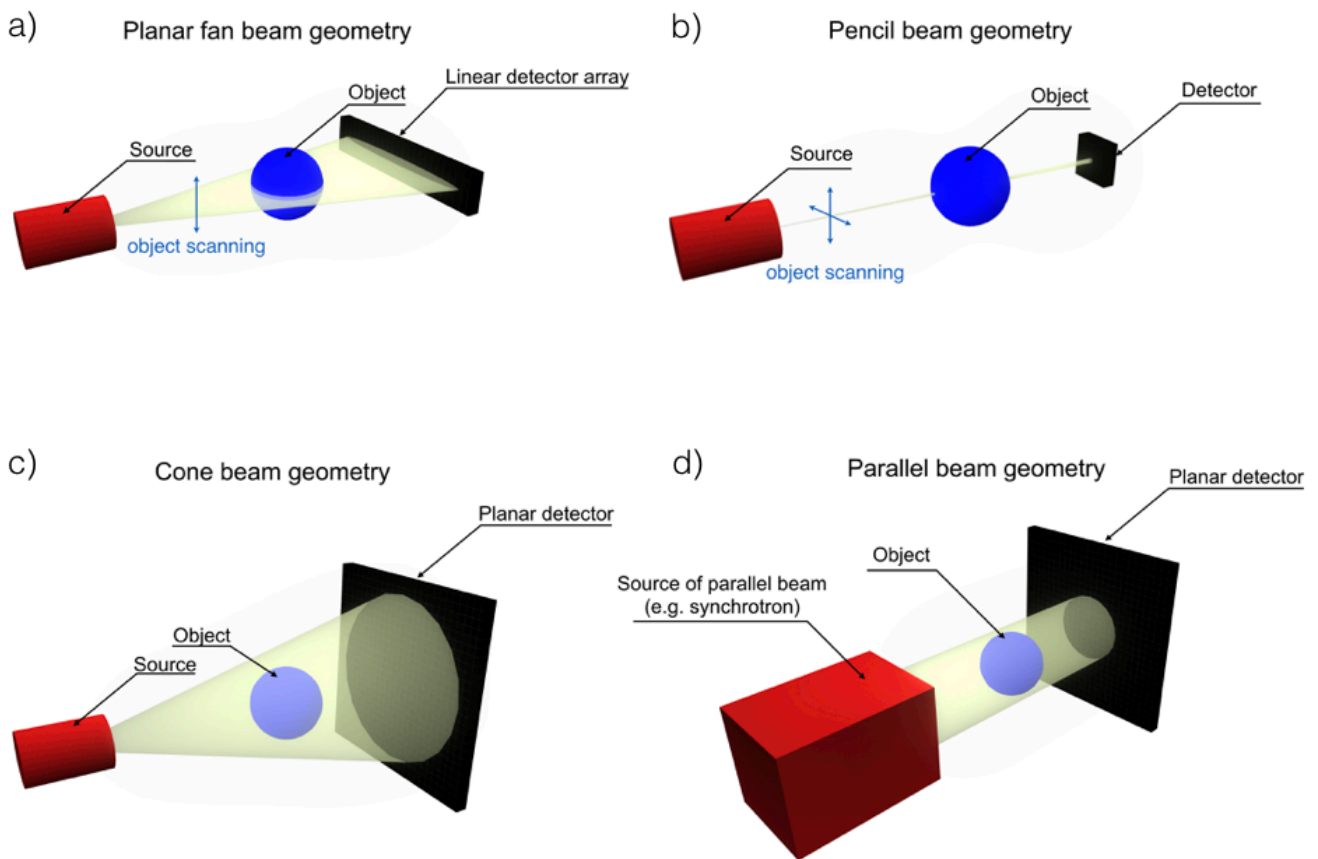
Figure 3.1 Various beam geometries in CT. a) Planar fan beam. In this case, to obtain full 3D reconstruction of the object, scanning in vertical direction is required. b) Pencil beam. Scanning in two perpendicular directions is required. c) Commonly used in commercial CT systems cone-beam configuration. d) Parallel-beam geometry. This configuration is often employed at synchrotron beamlines.

Another modification of X-ray CT arose from the fact that materials having different elemental compositions can be represented in a tomographic image by the same (or very similar) value. This is because the reconstructed linear attenuation coefficient is not unique for any given material, but is a function of the material composition, energy of photons interacting with the material, and the mass density of the material. In general, the attenuation of any material represented by X-ray tomographic image is caused by a combination of photoelectric and Compton effects. The photoelectric effect predominates at lower photon energies and is heavily energy-dependent. Compton scattering occurs almost independently of the photon energy at energies exceeding 30 keV. The photoelectric effect is related to high atomic numbers, whereas the Compton effect is predominantly related to the density of the material. Therefore, the impact of these two mechanisms varies at different energy levels. Thus, the problem can be partly overcome by attenuation measurements acquired with different energy spectra, along with

the use of the known changes in attenuation between the two spectra. This, the so-called dual-energy tomography helps to differentiate and to quantify material composition.

Similarly to X-ray tomography, transmission neutron tomography involves the production of three-dimensional images by the detection of the absorbance of neutrons produced by a neutron source. Typically, the spatial resolution of neutron tomographic systems is lower than X-ray systems (down to ~25 μm). X-ray and neutron tomography are complementary methods. They show different characteristics of the imaged object due to differences in neutron and X-ray interaction with the material of investigated object. Contrary to X-rays, neutrons interact significantly with some light materials (e.g., hydrogenous substances, boron or lithium) and penetrate heavy materials with minimal attenuation. This makes neutron tomography particularly sensitive to samples with low abundance of hydrogenous materials.

Among transmission methods, we can also distinguish absorption-contrast and phase-contrast (refraction) methods. Tomographic techniques listed above belong to absorption methods. It is however possible to exploit differences in the refractive index of materials, rather than attenuation coefficient, to differentiate between investigated structures. This phase-contrast imaging is used extensively in optical microscopy. In X-ray tomography, phase-contrast can be used to image structures with similar attenuation coefficients that could appear in absorption as almost uniform. This is very useful in biological, medical and geological applications. Contrast-phase variations in the X-rays emerging from the object have to be eventually converted into intensity variations at an X-ray detector. This can be done in several ways. The so-called propagation-based phase-contrast techniques use free-space propagation in order to enhance object edges [Zaprazny 2012]. The propagation-based phase contrast methods usually require special phase-retrieval algorithms. Several of them have been developed. While this topic is beyond the scope of this book, the paper by Nugent [Nugent 2007] is an excellent summary of phase-retrieval techniques in X-ray imaging. Talbot interferometry uses a set of diffraction gratings to measure the derivative of the phase. X-ray Talbot interferometry has the advantage that it functions with polychromatic cone-beam X-rays [Momose 2006]. Differential phase measurements are also performed in diffraction-enhanced imaging that uses an analyzer crystal [Kitchen 2007]. X-ray interferometry uses a crystal interferometer to measure the phase directly [Bonse 1965; Beckmann 1995; Momose 1995].

In emission tomography, no external source is used – the investigated object is the source of radiation itself. A classic example of emission tomography is Positron Emission Tomography (PET), widely applied in medicine. PET consists in detection of pairs of gamma rays emitted by positron-emitting radionuclide – so-called tracer, which is introduced into a patient body on a biologically active molecule. Imaging of the local tracer concentration is possible due to the unique properties of positron decay

and annihilation. After the emission from the parent nucleus, the energetic positron traverses a few millimeters through the tissue until it becomes thermalized by electrostatic interaction between the electrons and the atomic nuclei of the media and combines with a free electron to form a positronium. The positronium decays by annihilation, generating a pair of gamma rays which travel in nearly opposite directions. Each of these photons carries an energy of 511 keV. The photons are detected in coincidence using pairs of collinearly aligned detectors. The other example of emission tomography is Single-photon Emission Computed Tomography (SPECT) also commonly used in medicine. SPECT also requires delivery of a gamma-emitting radioisotope into the patient bloodstream. Gamma rays, emitted from the radioisotope located in a patient body, are registered using a gamma camera. Multiple projections - from multiple angles - are acquired, allowing tomographic reconstruction. SPECT is similar to PET in its use of radioactive tracer material and detection of gamma rays. In contrast to PET, however, the tracers used in SPECT emit gamma radiation that is measured directly, whereas PET tracers emit positrons that annihilate with electrons producing two gamma photons to be emitted in opposite directions. A PET scanner detects these emissions coincident in time, which allows achieving higher spatial resolution than SPECT. On the other hand, SPECT is a significantly less expensive technique than PET. This is because the method uses longer-lived and more easily obtained radioisotopes than PET.

A separate class of tomographic methods is Magnetic Resonance Tomography. Magnetic resonance imaging is based on the fact that certain atomic nuclei (hydrogen mostly used in clinical practice) can absorb and emit radio-frequency (RF) radiation when exposed to external electric fields. The subject of MRI is definitely beyond the scope of this book.

Figure 3.2. An example of emission tomography – Positron Emission Tomography. A positron emitted by radionuclide travels very short distance before it annihilates and generates the pair of gamma rays each of energy of 511 keV. The two almost back-to-back emitted photons are registered in coincidence by two external scintillation detectors in order to determine both activity and location of the positron emitter.

The interested Reader is referred to many excellent monographs on this topic [Bushong 2014; Hashemi 2003; Westbrook 2011].

Since thermonuclear plasma emits a wide range of electromagnetic waves as well as particle radiation, plasma tomography relays mostly on emission techniques. However, in some cases, external beams are also used on fusion devices, e.g. to recover the spatial electron density distribution from far infrared (FIR) interferometric measurements [Doyle 1986]. Tomographic techniques routinely applied at fusion devices (tokamaks and stellarators) include: soft and hard X-ray tomography, gamma tomography, neutron tomography and bolometry. The distinction between soft and hard energy range is made according to different origins of the measured photons and different physical phenomena involved. This will be explained in details in the following chapters of the book. Further information on neutron, gamma and X-ray detection systems at modern tokamak devices is presented in Section 6.2 of the book.

4. Reconstruction methods in classical tomography

Reconstruction of a tomographic image relies on the application of a dedicated mathematical method to retrieve the original spatial distribution (in 2D or 3D) of desired quantity in investigated object (e.g. linear attenuation coefficient or any other quantity from the third column of Tab. 3.1), based on the results of measured line-integrated values. In this book, we distinguish between 'classical' reconstruction methods and a separate class of methods used in fusion science, where the reconstruction is typically preformed from sparse data sets and an appropriate regularisation method is required. The latter methods are disused in detail in Chapter 6. Here we focus on 'classical' reconstruction methods that fall into two categories: analytical or iterative. Among analytical methods a few of them are presented in the subsequent part of the chapter, namely: direct Fourier inversion method, back-projection (BP) method, and its modifications commonly applied in medical CT: back-projection filtering (BPF) method, filtered back-projection (FBP) method and convolution back-projection (CBP) method. In turn, the iterative methods use the differences between the measured data and the calculated data to update an image in an iterative manner. The initial reconstructed images (a guess or an image given by BP method) are refined and modified iteratively until certain criteria are met. One example of an iterative method - Algebraic Reconstruction Technique is discussed in Chapter 5. In general, the analytical approach such as FBP is less perfect, albeit much faster and thus it has become the golden standard in reconstruction methods for diagnostic CT.

4.1 General definition of the tomographic inversion problem

Let us start the discussion on tomographic reconstruction methods with a simple intuitive example. Let us assume that our image to be reconstructed is 2D and consists of 64 (8×8) unit-area elements (pixels). Only 2 out of 64 elements have values different than zero and arbitrary equal to 1. The situation is shown in Figure 4.1a. To relate this simplified image with some physical reality let us assume that the image represents the X-ray linear attenuation coefficient given in arbitrary units. Moreover, to further simplify our discussion, let us assume that we have measured only two perpendicular projections of the object. The projections created by the registration of the X-rays passing through the object along two perpendicular directions are presented in Figure 4.1b. According to back-projection method, in the first step, we assign to all image elements in a given column the same average value associated with the vertical projection. This is equivalent to smearing out or,

as the name of the method indicates, back-projecting of the measured projection along the original paths of the rays over the image grid. This process of back-projecting of the vertical projection is schematically shown in Figure 4.1c. Similarly, we repeat the procedure for the horizontal projection, summing up, for every image element, the values resulted from every back-projection process. This is shown in Figure 4.1d. The image resulting from back-projecting of both available projections is illustrated in Figure 4.1e. Using such a limited data set (two projections only!) we are able to reconstruct the location of both non-zero elements of the original image. However, it is important to note that, as a result of the reconstruction, we also obtained artifacts in the form of four streaks and two artificial points. It can be shown that performing more projection measurements, and using them for reconstruction does not prevent this situation. In the general case, an image reconstructed by simple back-projection method carries the information on the original image distorted (blurred) by factor $\dfrac{1}{|r|}$, where r is the distance from the origin. This will be formally shown in the subsequent part of this chapter.
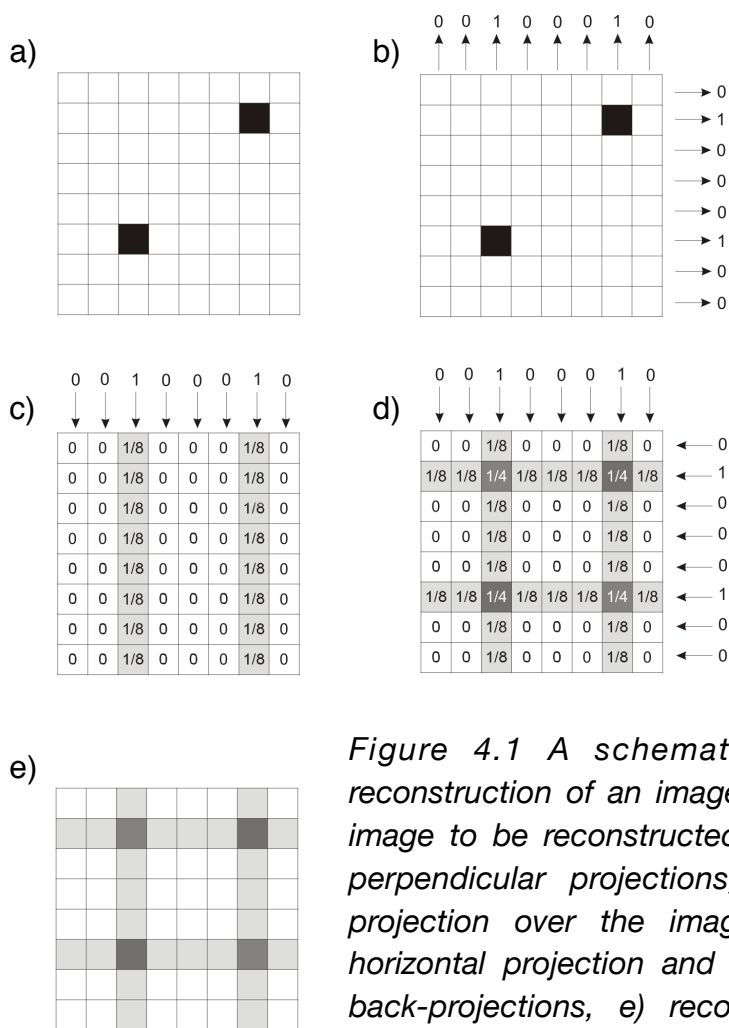
Figure 4.1 A schematic illustration of back-projection reconstruction of an image composed of two points. a) Original image to be reconstructed, b) Results of measurements of two perpendicular projections, c) back-projecting of the vertical projection over the image plane, d) back-projecting of the horizontal projection and summing up contributions from both back-projections, e) reconstructed image affected by streak artefacts.

4.2 Line integrals and projections

In order to discuss further the analytical reconstruction methods, we have to introduce some formal definitions. We will use the coordinate system shown in Figure 4.2. For the sake of simplicity, we will focus on two-dimensional case. Let (x, y) be the Cartesian coordinates, and $f(x, y)$ be a compactly supported continuous function on $\mathbb{R}^2$. For given $f(x, y)$ and given (θ, s) we define a line integral as a value of:

$$p = \int_L f(x, y) dl, \qquad (4.2.1)$$

where L is a straight line defined by (θ, s) parameters shown in Figure 4.2 and l is the path along given line L. A projection $P_\theta(s)$ is a set of line integrals for all values of parameter s. An example of projection $P_{(\theta=45°)}(s)$ for $\theta = 45°$ is also illustrated in Figure 4.2.
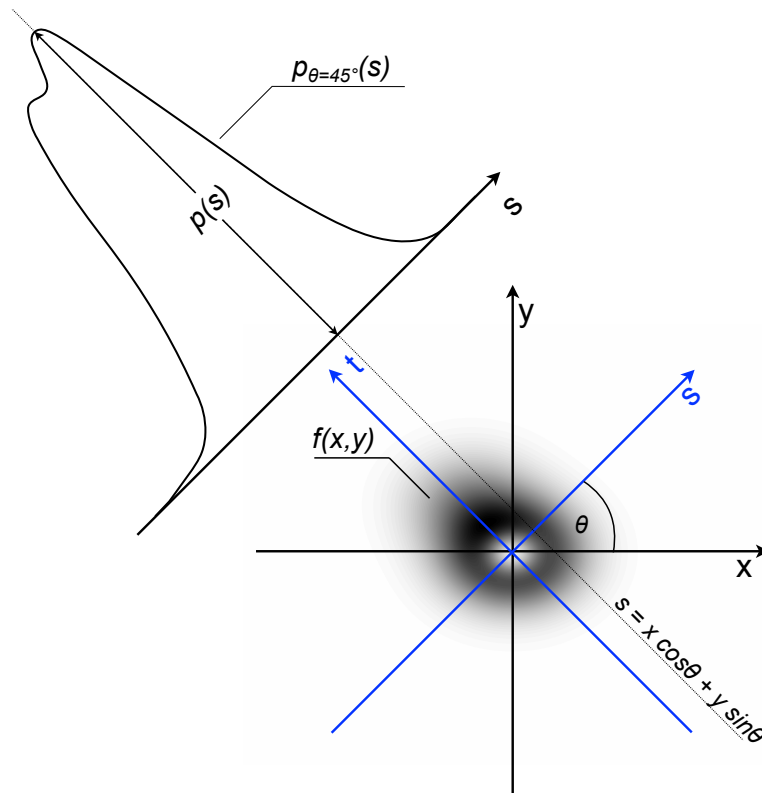
Figure 4.2 The coordinate systems and an example of a line integral and projection for $\theta = 45°$. (s, t) is the rotated system.

4.3 The Radon Transform

The Radon transform P of $f(x, y)$ in two dimensions is given by:

$$P = \mathscr{R}f = \int_L f(x, y)dl, \tag{4.3.1}$$

for all lines L. $\mathscr{R}$ designates here the Radon transform operator, l is the path along line L. Function $f(x, y)$ can be interpreted e.g. as the local neutron or X-ray emissivity (i.e. the number of neutrons or X-ray photons emitted by a unit plasma volume per unit time) in a poloidal cross-section of plasma confined in a tokamak. L would be then a viewing line through the plasma and $p(s)$ the experimentally measured line-integrated emissivity. In case of absorption medical CT, function $f(x, y)$ can be identified with a distribution of the linear attenuation coefficient in a cross-section of a human body.

In computed microtomography or medical CT, where either a scanned object or equivalently an X-ray source and a detector are being rotated, it is very useful to perform transformation from (x, y) coordinate system to the rotated system (s, t) (see Figure 4.2). In plasma tomography, where neither plasma nor a detection system can be rotated, we have to deal with multiple, angularly distributed Lines of Sight (LoS) of a detection system (see. Section 6.2). The relationships between the two systems are following:

$$(x, y) \rightarrow (s, t) \qquad\qquad (s, t) \rightarrow (x, y)$$

$$s = x\ cos(\theta) + y\ sin(\theta) \qquad\qquad x = s\ cos(\theta) - t\ sin(\theta)$$

$$t = -x\ sin(\theta) + y\ cos(\theta) \qquad\qquad y = s\ sin(\theta) + t\ cos(\theta), \tag{4.3.2}$$

where θ denotes the angle between axes x and s .

Using (s, θ) parametrisation, the Radon transform can be expressed as:

$$P(s, \theta) = \int_{-\infty}^{\infty} \int_{-\infty}^{\infty} f(x, y)\delta(xcos(\theta) + ysin(\theta) - s)dxdy, \tag{4.3.3}$$

where δ denotes the Kronecker delta. The pair of (s, θ) quantities can be considered as coordinates on the space of all lines in $\mathbb{R}^2$.

The graphical representation of the Radon transform of the $f(x, y)$ function from Figure 4.2 is shown in Figure 4.3. In tomographic terms, this graphical representation of the Radon transform is called sinogram.

The plot is called sinogram for the following reason:

Theorem:

The Radon transform of an isolated point is a sinusoidal function of θ with the amplitude of the sinusoid being the distance of the point from the origin.

Proof:

Let an isolated point function be represented by 2D Dirac function:

$$f(x, y) = \delta(x - x_0)\delta(y - y_0). \tag{4.3.4}$$

Then, the Radon transform:

$$P(s, \theta) = \int_{-\infty}^{\infty} \int_{-\infty}^{\infty} \delta(x - x_0)\delta(y - y_0)\delta(x\cos(\theta) + y\sin(\theta) - s)dxdy. \tag{4.3.5}$$

Thus*,

$$P(s, \theta) = \delta(x_0\cos(\theta) + y_0\sin(\theta) - s). \tag{4.3.6}$$

$P(s, \theta)$ does not vanish only for:

$$s = x_0\cos(\theta) + y_0\sin(\theta). \tag{4.3.7}$$

Substituting:

$$x_0 = C\sin\phi; \quad y_0 = C\cos\phi, \tag{4.3.8}$$

$$s = C \sin\phi \cos\theta + C \cos\phi \sin\theta = C \sin(\phi + \theta), \tag{4.3.9}$$

where:

$$x_0^2 + y_0^2 = C^2\sin^2\theta + C^2\cos^2\theta = C^2, \tag{4.3.10}$$

$$C = \sqrt{x_0^2 + y_0^2}. \tag{4.3.11}$$

---

* Strictly product of two delta functions is not well defined, however the relationship can be deduced noting that each projection is a function that is zero everywhere except at a single point at some location s, which is dependent on θ.

The sinogram of any object is the superposition of all the sinusoids, each weighted by the value $f(x, y)$. This can indicate that there should be enough information in the sinogram to recover the original function $f(x, y)$, providing that we are able to unscramble all of those sinusoids. The definition of the Radon transform can be also generalised to higher dimensions [Deans 1978], however for all applications presented in this textbook it is satisfactory to focus solely on 2D Radon transform.
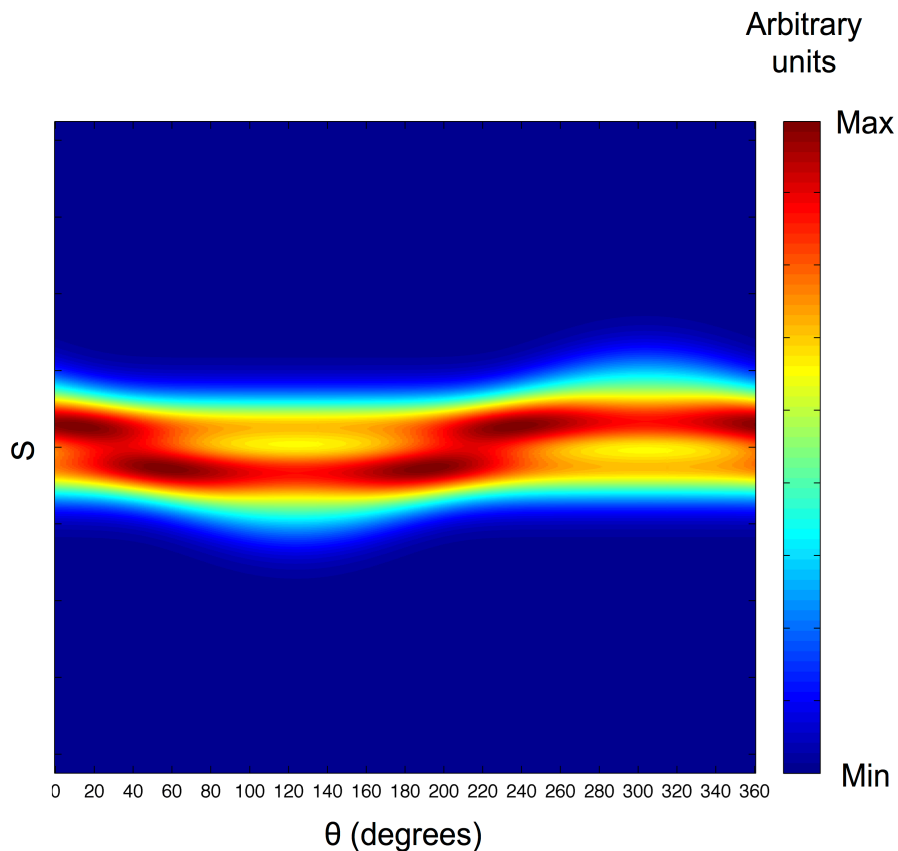
Figure 4.3 Sinogram as a graphical representation of the Radon transform of function $f(x, y)$ presented in Figure 4.2.

4.4 Properties of the Radon transform

The following list shows (without proofs) a few basic properties of the Radon transform. This list however is by no means exhaustive. The Reader interested in a more mathematical treatment is referred to the textbook of Helgason [Helgason 1999].

Let us assume that: $\mathscr{R}: f(x,y) \to P(s,\theta)$. Then, the following properties of the Radon transform hold:

1) Linearity: If $\mathscr{R}: g(x,y) \to Q(s,\theta)$, then, $\mathscr{R}: \alpha f + \beta g \to \alpha P(s,\theta) + \beta Q(s,\theta)$, $\qquad$ (4.4.1)

2) Translation: $\mathscr{R}: f(x - x_0, y - y_0) \to P(s - x_0 cos\theta - y_0 sin\theta, \theta)$, $\qquad$ (4.4.2)

3) Rotation: $\mathscr{R}: f(xcos\theta' + ysin\theta', -xsin\theta' + ycos\theta') \to P(s, \theta - \theta')$, $\qquad$ (4.4.3)

4) Magnification: $\mathscr{R}: f(\alpha x, \alpha y) \to \dfrac{1}{|\alpha|} P(\alpha s, \theta)$, for $\alpha \neq 0$, $\qquad$ (4.4.4)

5) Flips: $\mathscr{R}: f(-x, y) \to P(s, \pi - \theta)$, $\mathscr{R}: f(x, -y) \to P(-s, \pi - \theta)$,

The last two properties are special cases of the more general affine scaling property of the Radon transform [Fessler 2014].

6) The projection-integral theorem: for a scalar function $z : \mathbb{R} \to \mathbb{R}$:

$$\int P(s,\theta) \, z(s) ds = \int \left(\int f(s \, cos\theta - t \, sin\theta, s \, sin\theta + t \, cos\theta) dt \right) z(s) \, ds = \int\int f(x,y) z(xcos\theta + ysin\theta) dx dy$$

(4.4.5)

In the special case when $z(s) = 1$ we obtain:

7) Volume conservation: $\int P(s,\theta) ds = \int\int f(x,y) dx dy = F(0,0) \quad \forall \theta$, $\qquad$ (4.4.6)

where $F(x,y)$ denotes the Fourier transform of function $f(x,y)$.

4.5 The Abel transform

The Abel transform designated by the operator $\mathscr{A}$ is a special case of the 2D Radon Transform, valid when the function being transformed is rotationally symmetric. Figure 4.4 shows graphical interpretation of the Abel transform in 2D.

If function $f_a(\vec{r})$ is independent of the polar angle θ in polar coordinates $\vec{r} = (r, \theta)$ i.e. $f_a(x, y) = f_a(\vec{r}) = f_a(r)$, then all projection directions are equivalent. Thus, without losing generality, we can choose projection parallel to the x axis. Then, the Radon transform defined by Eq. 4.3.1 becomes:

$$\mathscr{R} f_a(r) = \mathscr{A} f_a(r) = P_a = \int_{-\infty}^{\infty} f_a(r) dy \tag{4.5.1}$$

Since: $x^2 + y^2 = r^2$ and $dy = \dfrac{r}{y} dr$,

$$P_a(x) = 2 \int_{|x|}^{\infty} f(r) \frac{r}{\sqrt{r^2 - x^2}} dr, \tag{4.5.2}$$

where we used symmetry properties of $f_a(r)$. Equation 4.5.2 is explicit form of the Abel transform.
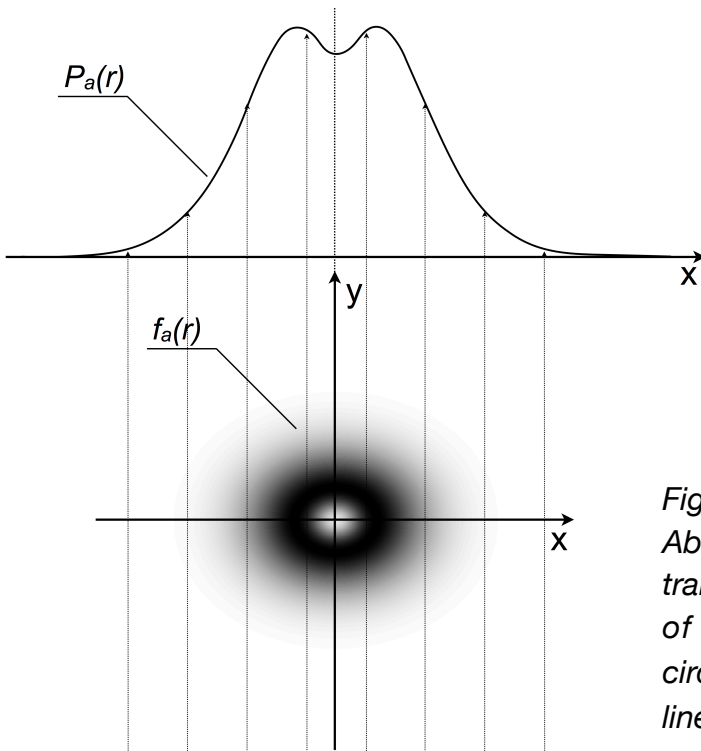
Figure 4.4 *Geometrical interpretation of the Abel transform in two dimensions. The Abel transform can be considered as a process of projection (i.e. integration) of the circularly symmetric function $f_a(r)$ along the lines of sight.*

4.6 Fourier Slice Theorem

Perhaps the most important theorem in computed tomography states that:

> Theorem:
>
> The 1D Fourier transform of a parallel projection $P_\theta(s)$ of function $f(x, y)$ is equal to 1D slice of the 2D Fourier transform of function $f(x, y)$ through the origin in the Fourier space evaluated at angle θ.
>
> Proof:
>
> 2D Fourier transform of function $f(x, y)$ is given by:
>
> $$\mathscr{F}(f(x, y)) = F(u, v) = \int_{-\infty}^{\infty} \int_{-\infty}^{\infty} f(x, y)e^{(-2\pi i(ux+vy))}dxdy, \tag{4.6.1}$$
>
> where (u, v) are frequency variables. Without loss of generality we can choose $\theta = 0$ (projection parallel to x axis), thus $y = 0$.
>
> From Eq. 4.6.1 we obtain:
>
> $$F(u,0) = \int_{-\infty}^{\infty} \int_{-\infty}^{\infty} f(x, y)e^{-2\pi iux}dxdy. \tag{4.6.2}$$
>
> Since the phase factor is now independent of y, we can split the integral as follows:
>
> $$F(u,0) = \int_{-\infty}^{\infty} \left[\int_{-\infty}^{\infty} f(x, y)dy \right] e^{-2\pi iux}dx. \tag{4.6.3}$$
>
> We can recognise the term in the brackets as the equation for a projection along lines of constant x i.e. projection at angle $\theta = 0$:
>
> $$P_{\theta=0}(x) = \int_{-\infty}^{\infty} f(x, y)dy. \tag{4.6.4}$$
>
> Substituting the above equation into Eq. 4.6.3, we obtain:
>
> $$F(u,0) = \int_{-\infty}^{\infty} P_{\theta=0}(x)e^{-2\pi iux}dx. \tag{4.6.5}$$

Now, let us define projection at an angle $\theta = 0$ as $P_{\theta=0}(s) = P_{\theta=0}(x)$ and its Fourier transform:

$$\mathscr{F}(P_{\theta=0}(x)) = S_{\theta=0}(u) = \int_{-\infty}^{\infty} P_{\theta=0}(x)e^{-2\pi iux}dx\,. \qquad (4.6.6)$$

Thus, the right-hand side of Eq. 4.6.5 represents 1D Fourier transform of the projection $P_{\theta=0}(x)$. Thus, we found the following relationship:

$$F(u,0) = S_{\theta=0}(u)\,. \qquad (4.6.7)$$

This result however is independent of the orientation between the object and the coordinate system i.e. if the (s,t) coordinate system is rotated by an angle θ, the Fourier transform of the projection from Eq. 4.6.6 is equal to 2D Fourier transform of the object along a line that is rotated by θ:

$$F(\rho,\theta) = S_{\theta}(\rho)\,. \qquad (4.6.8)$$

The theorem is illustrated in Figure 4.5. Using this figure, the theorem can be paraphrased as follows: The Fourier transform of projection $P_{\theta}(s)$ gives the values of $F(u,v)$ along BB' line in Figure 4.5.
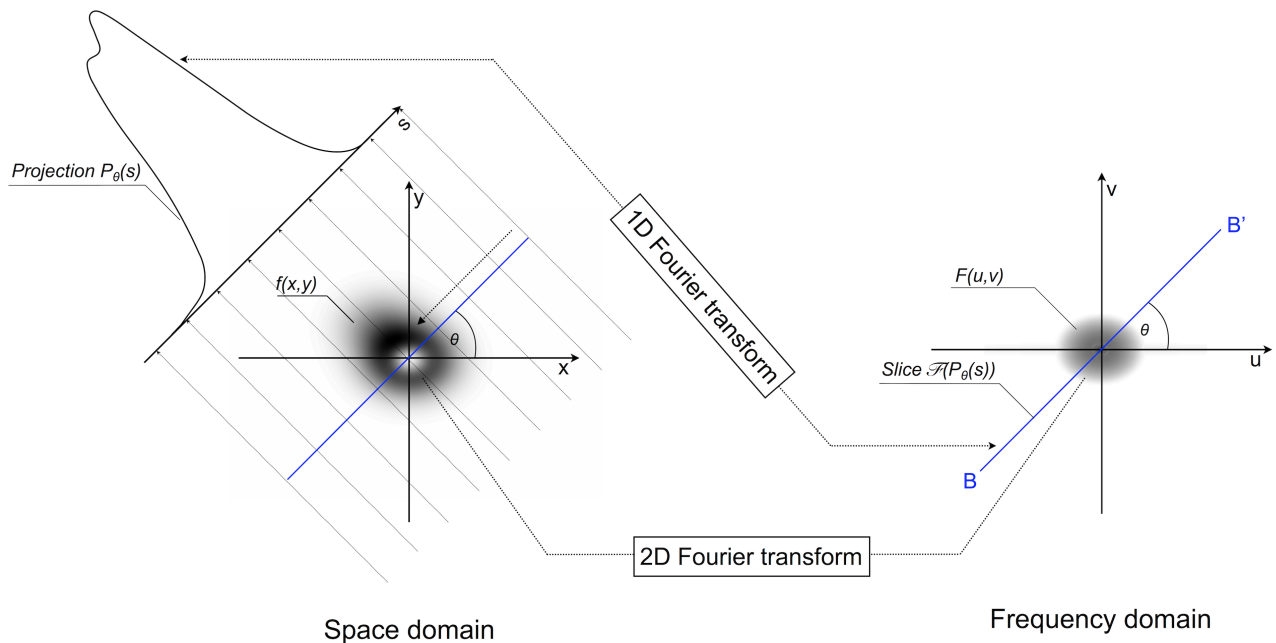
Figure 4.5 Illustration of the Fourier Slice Theorem.

4.7 Direct Fourier reconstruction

The tomographic reconstruction can be directly based on the Fourier Slice theorem. To reconstruct function $f(x, y)$ from a set of its projections $\{P_{\theta_1}(s), P_{\theta_2}(s), ..., P_{\theta_N}(s)\}$, at first we have to calculate 1D Fourier transforms of each projection: $\{S_{\theta_1}(\rho), S_{\theta_2}(\rho), ..., S_{\theta_N}(\rho)\}$. Using the Fourier Slice Theorem we can determine the values of 2D Fourier transform $F(u, v)$ of the function $f(x, y)$ on radial lines defined by the set of $\{\theta_1, \theta_2, ..., \theta_N\}$, as shown in Figure 4.6. Only if an infinite number of projections are taken, then $F(u, v)$ would be known at all points in the (u, v) plane. Then, the function $f(x, y)$ can be recovered using the inverse 2D Fourier transform:

$$f(x, y) = \int_{-\infty}^{\infty} \int_{-\infty}^{\infty} F(u, v) e^{(2\pi i(ux+vy))} du\, dv, \qquad (4.7.1)$$

In practice, the implementation is based on the Inverse Fast Fourier Transform (IFFT) [Brigham 2002]. The 2D IFFT requires Cartesian samples while Fourier Slice Theorem relationship is intrinsically polar. Moreover, the projections are measured with a finite resolution. This means that only a finite number of values along the radial lines defined by the set of $\{\theta_1, \theta_2, ..., \theta_N\}$ is known. Thus, the proper interpolation is needed. We leave the detailed discussion on the numerical implementation of the method, since it is not crucial for the general understanding of the topic. The Direct Fourier reconstruction method provides good results if the measured projections $\{P_{\theta_1}(s), P_{\theta_2}(s), ..., P_{\theta_N}(s)\}$ are noiseless. In practice however, the required interpolation can introduce some artefacts. Moreover, the method involves computationally demanding 2D Fourier Transform.
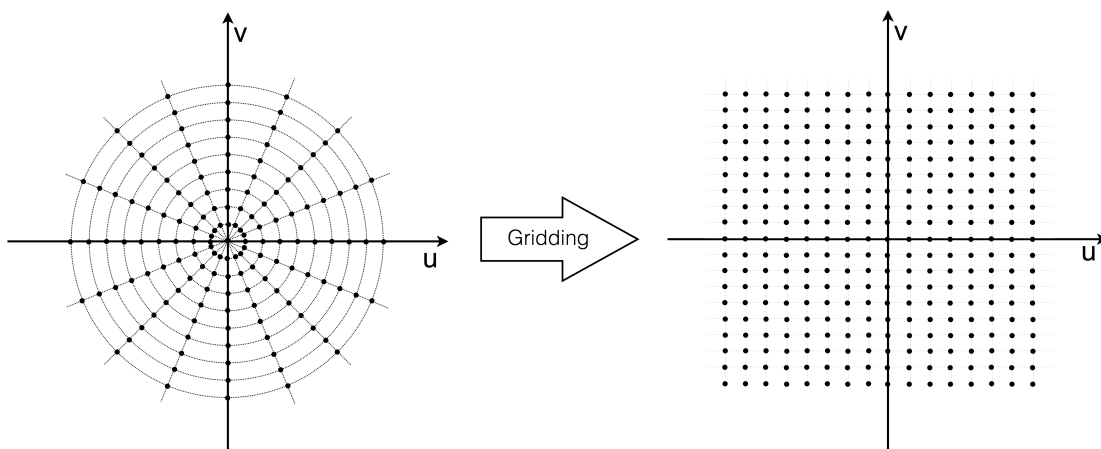
Figure 4.6 Illustration of the polar samples and interpolation onto Cartesian coordinates in the direct Fourier reconstruction method.

4.8 Back-projection

As it was shown in Section 4.3, the Radon transform maps the original object function $f(x,y)$ into its sinogram $P(s,\theta)$. In Chapter 4.1, in order to recover the function $f(x,y)$ from $P(s,\theta)$, we used back-projection method in a simple and intuitive way. In this approach, we take each sinogram value and 'smear' it back into object space along the corresponding ray. Formally, the back-projection operation for the parallel beam is given by:

$$f_{BP}(x,y) = \int_0^\pi h(\theta)\, P(x\, cos\theta + y\, sin\theta, \theta)d\theta. \qquad (4.8.1)$$

In the above equation we introduced a user-chosen weight $h(\theta)$ for angle θ. This kind of weighting is useful when different projections have different signal to noise ratio. However, in the simplest case we can simply assume that $h(\theta) = 1$.

We will demonstrate now the fact which was announced in the beginning of the chapter – the function reconstructed using back-projection method $f_{BP}(x,y)$ is a severely blurred version of the original function $f(x,y)$. At first, let us note that the back-projection operation is linear and shift-invariant:

$$f_{BP}(x-c, y-d) = \int_0^\pi h(\theta)\, P\big((x-c)cos\theta + (y-d)sin\theta, \theta\big)d\theta = \int_0^\pi h(\theta)\, P(r - c\, cos\theta - d\, sin\theta, \theta)d\theta, \quad (4.8.2)$$

where we used property 2 of the Radon transform presented in Section 4.4. Due to this shift-invariant, it is sufficient to examine the behaviour of $f_{BP}(x,y)$ only in a single point. For simplicity let us choose $(x,y) = (0,0)$. Then, the reconstructed image of the point is given by:

$$f_{BP}(0,0) = \int_0^\pi h(\theta')\, P(0,\, \theta')d\theta' = \int_0^\pi h(\theta')\left[\int_{-\infty}^\infty f(0\, cos\theta' - l\, sin\theta', 0\, sin\theta' + l\, cos\theta')dl\right]d\theta' =$$

$$= \int_0^\pi \int_{-\infty}^\infty \frac{h((\theta + \pi/2)mod\pi)}{|r|} f(0 - rcos\theta, 0 - rsin\theta)|r|drd\theta, \qquad (4.8.3)$$

where we made the following variable change: $\theta' = (\theta + \pi/2)mod\pi$, $l = \begin{cases} r & \text{if } \theta' \in \left[\frac{\pi}{2}, \pi\right] \\ -r & \text{if } \theta' \in \left[0, \frac{\pi}{2}\right) \end{cases}$.

Using previously mentioned shift invariant property, we obtain the following formula for back-projected image:

$$f_{BP}(x,y) = \int_0^\pi \int_{-\infty}^\infty \frac{h((\theta + \frac{\pi}{2})mod\pi)}{|r|} f(x - rcos\theta, y - rsin\theta)|r|drd\theta. \tag{4.8.4}$$

The equation shows that the function reconstructed using back-projection method is the convolution of $g(r,\theta) = \dfrac{h((\theta + \frac{\pi}{2})mod\pi)}{|r|}$ and $f(x,y)$ in polar coordinates. In the common case of unmodified projections, when $h(\theta) = 1$, we can notice that the function reconstructed using back-projection method is the original function blurred by the $\dfrac{1}{|r|}$ term. Function $\dfrac{1}{|r|}$, plotted in Figure 4.7, can be treated as the point-spread function. The heavy tails of this function limit the ability to interpret tomographic images reconstructed by simple back-projection method.
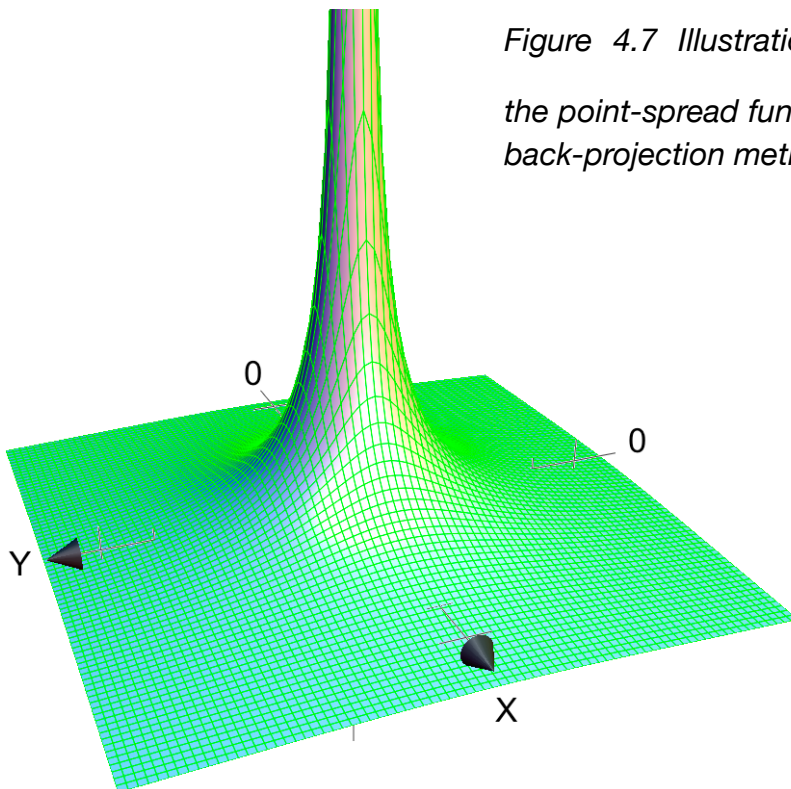
Figure 4.7 Illustration of the $\dfrac{1}{|r|}$ function that is the point-spread function in case of reconstruction by back-projection method.

Using Equation 4.8.4 and the convolution theorem (see Appendix 1), we can obtain the following relationship in the frequency domain:

$$F_{BP}(\rho, \Theta) = G(\rho, \Theta)F(\rho, \Theta),\qquad(4.8.5)$$

where $F_{BP}(\rho, \Theta)$ is the polar form of the 2D Fourier transform of $f_{BP}(r, \theta)$, $F(\rho, \Theta)$ is the polar form of the 2D Fourier transform of $f(r, \theta)$ and $G(\rho, \Theta)$ is the polar form of the 2D Fourier transform of the point-spread function $g(r, \theta)$.

Next, let us present and prove the following theorem:

Theorem:

The Fourier transform of $\dfrac{1}{|r|}$ is $\dfrac{1}{|\rho|}$.

Proof:

$$\mathscr{F}\left(\frac{1}{|r|}\right)\mathscr{F} = \left(\frac{1}{\sqrt{(x^2+y^2)}}\right) = \int_{-\infty}^{\infty}\int_{-\infty}^{\infty}\frac{1}{\sqrt{(x^2+y^2)}}e^{-2\pi i(xu+vy)}dxdy =$$

$$= \int_{-\infty}^{\infty}\int_{0}^{\pi}\frac{1}{r}e^{-2\pi i(ur\cos\theta+vr\sin\theta)}rdrd\theta = \int_{0}^{\pi}\delta(u\cos\theta + v\sin\theta)d\theta.\qquad(4.8.6)$$

To evaluate the above integral we use the following relationship:

$$\int\delta\big(f(x)\big)dx = \frac{1}{|f'(x_0)|},\qquad(4.8.7)$$

where x_0 is defined by equation: $f(x) = 0$ and f' denotes derivative of f.

Since $(u\cos\theta + v\sin\theta)' = -u\sin\theta + v\cos\theta$, then $\theta_0 = arctan\left(-\dfrac{u}{v}\right)$.

Thus,

$$\mathscr{F}\left(\frac{1}{|r|}\right) = \frac{1}{|-u\sin\left(arctan\left(-\frac{u}{v}\right)\right) + v\cos\left(arctan\left(-\frac{u}{v}\right)\right)|} = \frac{1}{\left|\dfrac{\frac{u^2}{v}+v}{\sqrt{1+\frac{u^2}{v^2}}}\right|} = \frac{u^2+v^2}{\sqrt{u^2+v^2}} = \frac{1}{|\rho|}\qquad(4.8.8)$$

where we used the fact that: $sin(arctan(x)) = \dfrac{x}{\sqrt{1+x^2}}$ and $cos(arctan(x)) = \dfrac{1}{\sqrt{1+x^2}}$.

In the more general case, the point-spread function given in Equation 4.8.4 has the following Fourier transform:

$$\mathscr{F}\big(g(r,\theta)\big) = \mathscr{F}\left(\frac{1}{|r|}\big(h(\theta + \pi/2)mod\,\pi\big)\right) = \frac{1}{|\rho|}h(\Theta)\,. \qquad (4.8.9)$$

The proof of the above theorem is deferred to Appendix 2.

Thus, in the general case the frequency-space relationship between the original object function and the function reconstructed using back-projection method is:

$$F_{BP}(\rho, \Theta) = \frac{h(\Theta)}{|\rho|}F(\rho, \Theta), \qquad (4.8.10)$$

Equation 4.8.10 suggests that high spacial frequencies are attenuated by the $\dfrac{1}{|\rho|}$ factor.

4.9 Back-projection filtering method

As it was shown in the previous section, the image function reconstructed by simple back-projection method is a highly blurred version of the original image function. Equation 4.7.9 however, gives us a hint how to improve this situation. Again, for the sake of simplicity let us assume the user-defined filter function in a simplest form of $h(\theta) = 1$. Then, using Equation 4.8.10 we can deduce the formula for the 2D Fourier transform of the image function reconstructed by back-projection filtering method $f_{BPF}(x, y)$:

$$F_{BPF}(u, v) = \sqrt{u^2 + v^2} F_{BP}(u, v), \tag{4.9.1}$$

where $F_{BP}(u, v)$ is the 2D Fourier transform of the back-projected image and the filter with frequency response $|\rho| = \sqrt{u^2 + v^2}$ is called the cone filter due to its shape. Equation 4.9.1 indicates the following steps of reconstruction. In the first step, we compute $f_{BP}(x, y)$ by simple back-projection of $P(s, \theta)$. Then, we compute 2D Fourier transform of $f_{BP}(x, y)$ in order to get $F_{BP}(u, v)$. Next, we apply the cone filter in the Fourier domain using Equation 4.9.1. The cone filter cancels out the DC component of $f(x, y)$, however it can be recovered using the volume conservation property of the Radon transform (Eq. 4.4.6). In the end, we calculate the inverse 2D transform of $F_{BPF}(u, v)$ to recover $f_{BPF}(x, y)$. This flow of back-projection filtering reconstruction method is summarised in Figure 4.8.

Back-projection: $f_{BP}(x, y) = \int_0^\pi h(\theta) P(x\cos\theta + y\sin\theta, \theta) d\theta$

2D Fourier transform: $F_{BP}(u, v) = \mathcal{F}\left(f_{BP}(x, y)\right)$

Application of the cone filter: $F_{BPF}(u, v) = \sqrt{u^2 + v^2} F_{BP}(u, v)$

Inverse 2D Fourier transform: $f_{BPF}(x, y) = \mathcal{F}^{-1}\left(F_{BPF}(u, v)\right)$
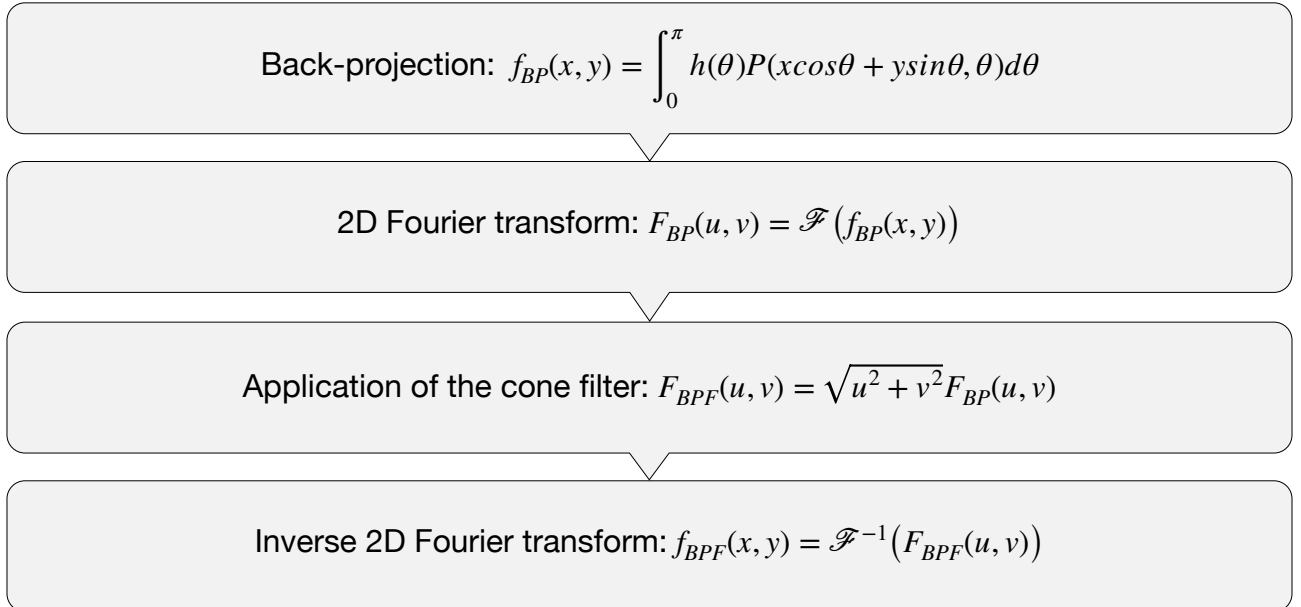
Figure 4.8 Flow of the back-projection filtering reconstruction method.

The method is called back-projection filtering because at first the sinogram is back-projected and then the cone filter is applied to deconvolve the blurring $\frac{1}{|r|}$ term.

The back-projection filtering method however, has a few disadvantages. First of all, it should be noted that function $f_{BP}(x, y)$ has unbounded spatial support. This is true even when the original function $f(x, y)$ has a finite support due to the tails of the $\frac{1}{|r|}$ term. Thus, the support of $f_{BP}(x, y)$ must be truncated in any practical application of the method due to the finite size of computer memory. Also, in practice, $f_{BP}(x, y)$ has to be computed using a significantly larger matrix size than is needed to store the final result of $f_{BPF}(x, y)$. A large grid increases the computational costs of both the back-projection step and the 2D Fourier transform needed for the filtering. This disadvantage can be overcome by interchanging the filtering and back-projection phases as discussed in the next section.

Another disadvantage of the method is caused by the cone filter itself. In practice, using the cone filter only would severely amplify high frequency components, increasing noise level. To counteract this, the cone filter is usually apodised in the frequency domain with a windowing function. In this case Eq. 4.9.1 becomes:

$$F_{BPF}(u, v) = A(u, v)\sqrt{u^2 + v^2}F_{BP}(u, v), \qquad (4.9.2)$$

where $A(u, v)$ is a low-pass filter.

4.10 Filtered back-projection method

As it was shown in the previous section, reconstruction of the original function using back-projecting and filtering has some drawbacks. However, thanks to the Fourier Slice Theorem, we can move the filtration step before the back-projection. Indeed, we can also recover the original function $f(x, y)$ in the following way:

$$f_{FBP}(x, y) = \iint F(u, v)e^{2\pi i(xu+yv)}du\,dv = \int_0^\pi \int_{-\infty}^\infty F(\nu cos\theta, \nu sin\theta)e^{2\pi i\nu(xcos\theta+ysin\theta)}|\nu|d\nu d\theta =$$

$$= \int_0^\pi \int_{-\infty}^\infty S_\theta(\nu)e^{2\pi i\nu(xcos\theta+ysin\theta)}|\nu|d\nu d\theta = \int_0^\pi \tilde{P}_\theta(xcos\theta + ysin\theta)d\theta \qquad (4.10.1)$$

In the first step of Equation 4.10.1 we changed (u, v) frequency variables to polar variables (ν, θ). In this case ν denotes radial variable along the line defined by Fourier Slice Theorem. In the second step we utilised the Fourier Slice Theorem: $F(\nu cos\theta, \nu sin\theta) = S_\theta(\nu)$ and in the third step we defined the filtered projection as:

$$\tilde{P}_\theta(s) = \int_{-\infty}^\infty S_\theta(\nu)|\nu|e^{2\pi i\nu s}d\nu. \qquad (4.10.2)$$

Equation 4.10.1 suggests the following, alternative method of the reconstruction. At first, for each projection angle θ, we compute the 1D Fourier transform of the projection $\{P_{\theta_1}(s), P_{\theta_2}(s), ..., P_{\theta_N}(s)\}$ to form $\{S_{\theta_1}(\nu), S_{\theta_2}(\nu), ..., S_{\theta_N}(\nu)\}$. Then, we multiply each Fourier transform by $|\nu|$ in order to obtain $\{|\nu|S_{\theta_1}(\nu), ..., |\nu|S_{\theta_N}(\nu)\} = \{\tilde{S}_{\theta_1}(\nu), ..., \tilde{S}_{\theta_N}(\nu)\}$. Next, for each θ, we have to compute the inverse 1D Fourier transform of $\tilde{S}_\theta(\nu)$ in order to obtain the set of filtered projection $\{\tilde{P}_{\theta_1}(s), ..., \tilde{P}_{\theta_N}(s)\}$. In the end, we perform back-projection of the filtered sinogram using the definition of back-projection operator (Eq. 4.8.1). The flow of the filtered back-projection reconstruction method is presented in Figure 4.9.

It is worth noting that a filtered projection $\tilde{P}_\theta(s)$ can have both positive and negative values contrary to a 'normal' projection $P_\theta(s)$ that obviously has only nonnegative values. This allows a destructive interference to occur in the regions where the image function is supposed to be zero. These regions however would be non-zero when the simple back-projection of unfiltered projections is used, due to the blurring $\dfrac{1}{|r|}$ term. An example of filtered and unfiltered projections of a simple square phantom model is shown in Figure 4.10.

Figure 4.9 Flow of the filtered back-projection reconstruction method.
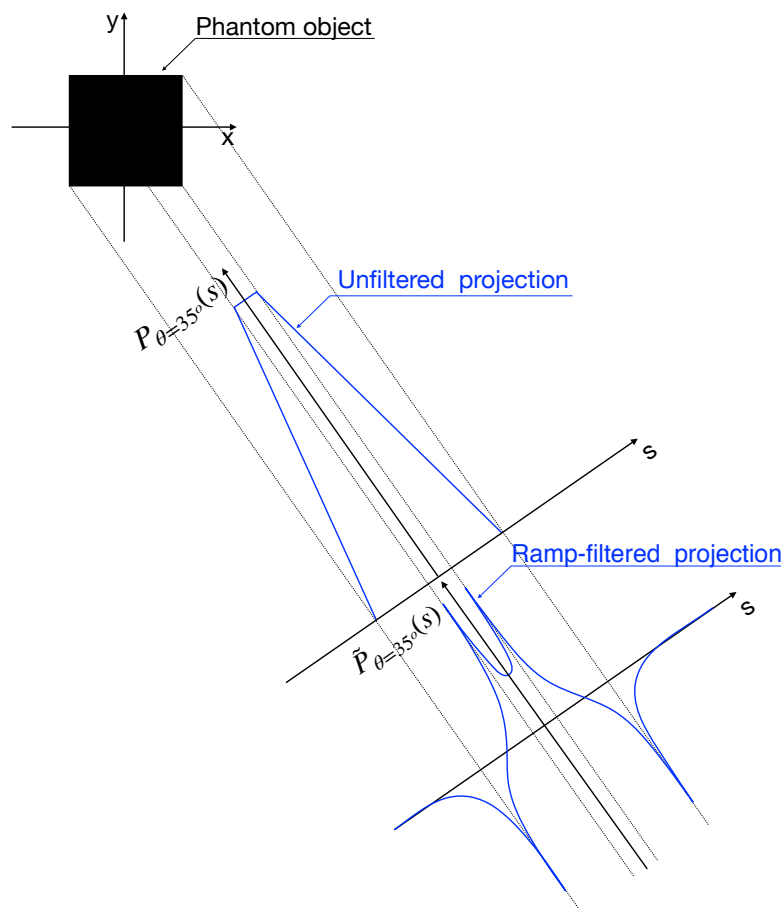
Figure 4.10 An example of filtered and unfiltered projection of a simple square model. The filtered projection features negative values allowing a destructive interference to occur in the regions where the original image is supposed to be zero.

4.11 Convolution back-projection

As it was mentioned earlier the ramp filter $|\nu|$ severely amplifies noise. Thus in practice, the filter is replaced (apodised with a windowing function) by a numerically more stable counterpart. In this case Equation 4.10.2 is replaced by:

$$\tilde{P}_\theta(s) = \int_{-\infty}^{\infty} S_\theta(\nu)A(\nu)|\nu|e^{2\pi i \nu s}d\nu, \tag{4.11.1}$$

where $A(\nu)$ is a one dimensional low-pass filter. Alternatively, this filtering operation can be done in the spatial domain by the following radial convolution:

$$\tilde{P}_\theta(s) = P_\theta(s) * h_a(s) = \int P_\theta(s')h_a(s - s')ds', \tag{4.11.2}$$

where the filter kernel $h_a(r)$ is the inverse Fourier transform of $H_a(\nu) = A(\nu)|\nu|$ i.e:

$$h_a(s) = \int_{-\infty}^{\infty} A(\nu)|\nu|e^{2\pi i \nu s}d\nu. \tag{4.11.3}$$

Using the formula for the back-projection of filtered projections from the previous section (Eq. 4.10.1) and Equation 4.11.2 we can define the method of convolution back-projection:

$$f_{CBP} = \int_0^\pi P(s,\theta) * h_a(x\cos\theta + y\sin\theta)d\theta = \int_0^\pi \int P(s,\theta)h_a(x\cos\theta + y\sin\theta - s)ds\,d\theta. \tag{4.11.4}$$

The simplest example is to use a spatially band-limited function. Such a function can be considered as an apodisation of the ramp filter $|\nu|$ with rectangular band-limiting window function $A(\nu) = rect\left(\dfrac{\nu}{2\nu_0}\right)$, where ν_0 is the maximum spatial frequency. This filter function is called Ram-Lak after names of two Indian physicists Ramachandran and Lakshminarayan [Ramachandran 1971]. Another commonly used filter is the so-called Shepp-Logan filter [Shepp 1974] named after an American mathematician Larry Shepp and an American electrical engineer Benjamin F. Logan. The filter is the result of multiplication in the frequency domain of the ramp filter by a $sinc$ function. Figure 4.11a presents the shapes of Ram-Lak and Shepp-Logan functions in the frequency domain, while Figure 4.11b shows their impulse response function. There are more filter functions commonly used in CT. The more complete list is given in Appendix 9.3.
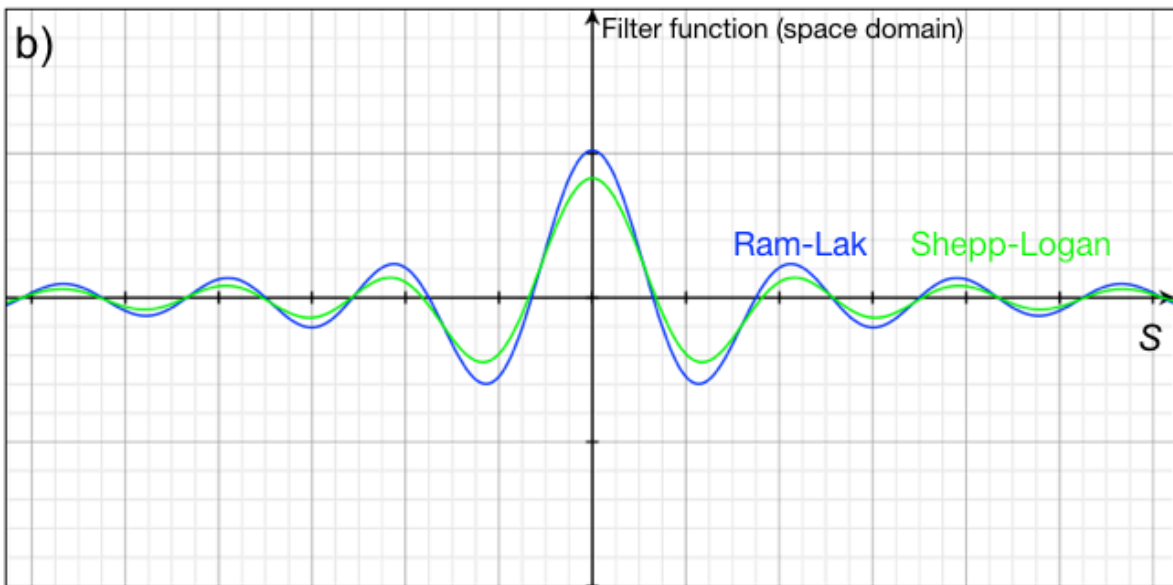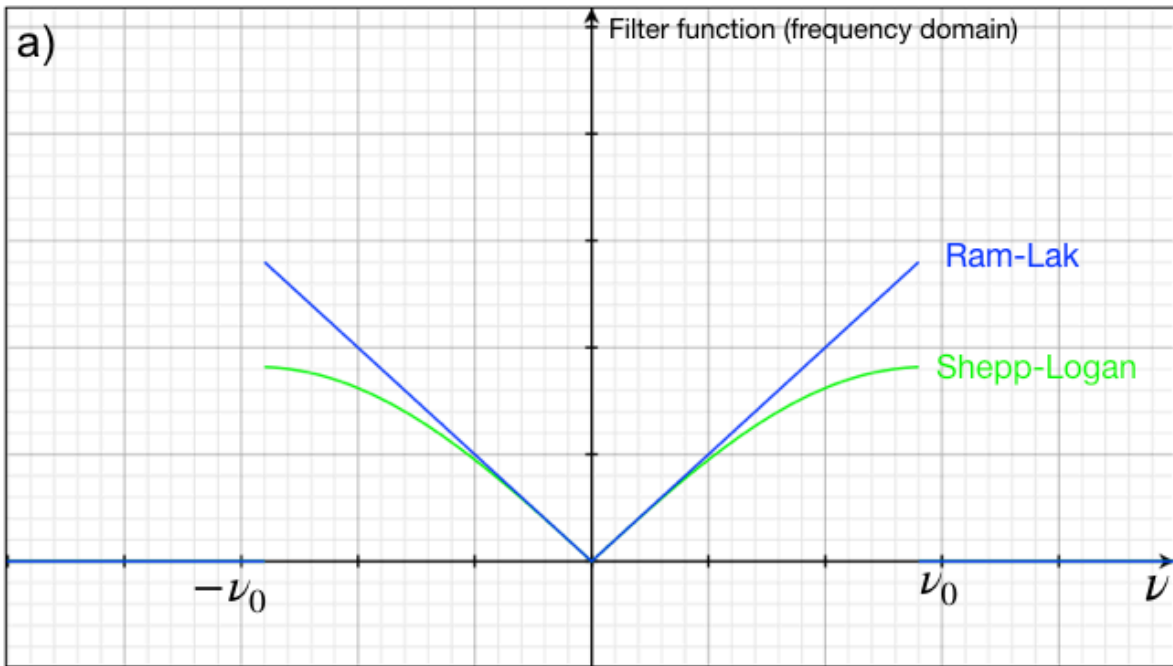
Figure 4.11 Ram-Lak and Shepp-Logan filter functions (a) and their impulse response functions (b).

4.12 Fan beam tomography

The preceding sections were focused on the analytic reconstruction methods for 2D parallel beam (parallel projections). This is a very important case because it gives a relatively simple insight into the reconstruction methods and has been practically realised in synchrotron tomography. However, most of modern commercial CT scanners rely on fan beam or cone beam geometry. In this section, we derive the filtered back-projection method for the fan beam geometry. The succeeding section presents the most popular method in case of cone-beam geometry.

A simple approach to reconstruct the original object from equiangular fan beam projections would be to rebin every fan beam projection into parallel beam ones. For each sinogram collected using a fan beam geometry $P_f(\gamma, \beta)$, we can find an equivalent sinogram of parallel beam $P(s, \theta)$ that has the same rays orientation as rays of the fan beam sinogram. For this purpose, the following relationships illustrated in Figure 4.12a are used:

$$\theta = \gamma + \beta, \tag{4.12.1}$$

$$s = D sin\gamma, \tag{4.12.2}$$

where D is the focal length, β is the angle between the source and the reference axis, and the angle γ gives the location of a ray within the fan.
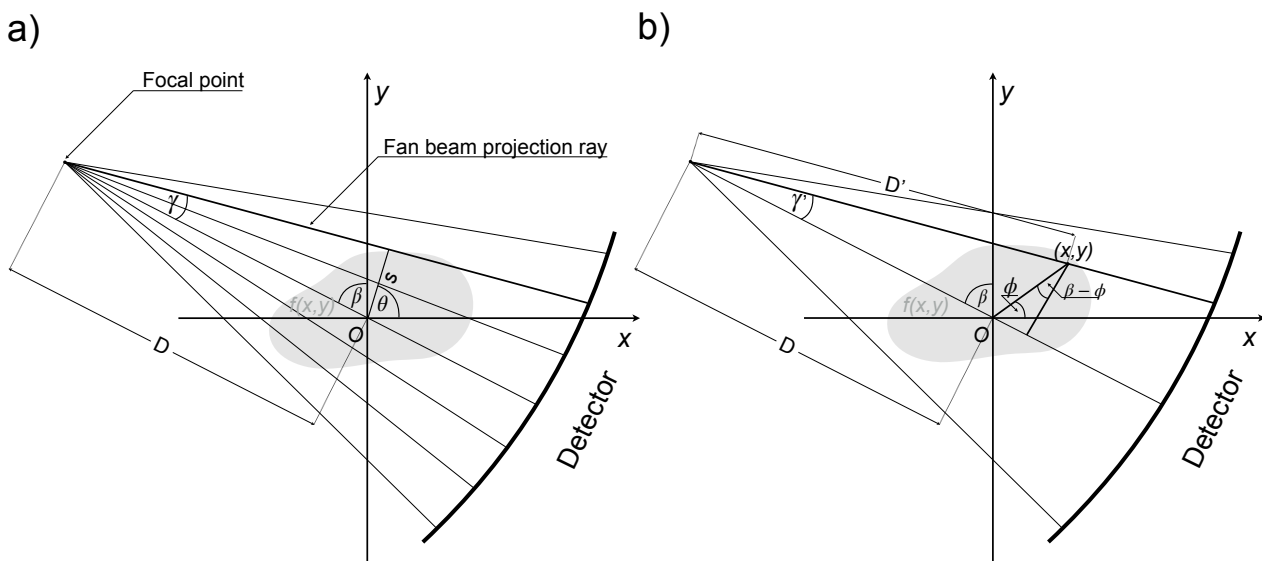
Figure 4.12 Equiangular fan-beam geometry. a) θ, s, γ, β and D relationships, b) β, γ', and D' relationships.

After this simple rebinning of the fan beam projections into the parallel beam format, we can use an algorithm for parallel beam. In practice, this approach requires data interpolation when changing coordinates. Such an interpolation typically introduces some errors. Thus, in order to obtain accurate results it is advantageous to start with an analytical expression for the parallel beam reconstruction and substitute the parallel projection by fan beam counterpart, changing variables by calculation of the proper Jacobian. Reconstruction method for the parallel beam geometry can be written as:

$$f(x, y) = \int_0^{\pi} \int P(s, \theta) h(x cos\theta + y sin\theta - s) ds d\theta, \qquad (4.12.3)$$

where the filter kernel $h(s)$ is the inverse Fourier transform of $|\nu|$:

$$h(s) = \int_{-\infty}^{\infty} |\nu| e^{2\pi i s} d\nu. \qquad (4.12.4)$$

This method only requires the parallel projections collected over 180°. However, projections collected over 360° also can be used. Then, Eq. 4.12.3 becomes:

$$f(x, y) = \frac{1}{2} \int_0^{2\pi} \int P(s, \theta) h(x cos\theta + y sin\theta - s) ds d\theta. \qquad (4.12.5)$$

Since it is easier to use polar coordinates (r, ϕ) (Fig. 4.12b) rather than Cartesian coordinates (x, y), we substitute:

$$x = r cos\phi \qquad\qquad y = r sin\phi. \qquad (4.12.6)$$

Equation 4.12.5 can be re-written as:

$$f(r, \phi) = \frac{1}{2} \int_0^{2\pi} \int P(s, \theta) h(r cos(\theta - \phi) - s) ds d\theta. \qquad (4.12.7)$$

Changing variables using expressions 4.12.1 and 4.12.2 and calculating Jacobian $\begin{vmatrix} cos\theta & -sin\theta \\ sin\theta & cos\theta \end{vmatrix} = D cos\gamma$, we obtain:

$$f(r, \phi) = \frac{1}{2} \int_0^{2\pi} \int_{-\pi/2}^{\pi/2} P_f^{(ea)}(\gamma, \beta) h(r cos(\beta + \gamma - \phi) - D sin\gamma) D cos\gamma d\gamma d\beta, \qquad (4.12.8)$$

where $P_f^{(ea)}(\gamma, \beta)$ is an equiangular fan beam Radon transform. The above equation describes the reconstruction method for the fan beam geometry. However, the inner integral over γ is not in the convolution form. Thus, in the next steps we convert the integral over γ to a convolution with respect to γ. For a given reconstruction point (r, ϕ) we can define a distance D' from the source to the point and the angle γ' of the ray that

passes through the point, as shown in Figure 4.12b. Then the argument of h can be rewritten as $r\cos(\beta + \gamma - \phi) - D\sin\gamma = D'\sin(\gamma' - \gamma)$ [Kak 2001] and Eq. 4.12.8 becomes:

$$f(r, \phi) = \frac{1}{2} \int_0^{2\pi} \int_{-\pi/2}^{\pi/2} P_f^{(ea)}(\gamma, \beta) h(D'\sin(\gamma' - \gamma)) D\cos\gamma \, d\gamma \, d\beta. \tag{4.12.9}$$

Using Eq. 4.12.4 we obtain:

$$h(D'\sin\gamma) = \int_{-\infty}^{\infty} |\nu| e^{2\pi i \nu D' \sin\gamma} d\nu. \tag{4.12.10}$$

Now, by making the following substitution:

$$\nu' = \nu \frac{D'\sin\gamma}{\gamma}, \tag{4.12.11}$$

we can write:

$$h(D'\sin\gamma) = \left(\frac{\gamma}{D'\sin\gamma}\right)^2 \int_{-\infty}^{\infty} |\nu'| e^{2\pi i \nu' \gamma} d\nu' = \left(\frac{\gamma}{D'\sin\gamma}\right)^2 h(\gamma). \tag{4.12.12}$$

Using the above formula, Eq. 4.12.9 can be written as:

$$f(r, \phi) = \int_0^{2\pi} \frac{1}{D'^2} \int_{-\pi/2}^{\pi/2} P_f^{(ea)}(\gamma, \beta) h_f(\gamma' - \gamma) \cos\gamma \, d\gamma \, d\beta, \tag{4.12.13}$$

where we defined:

$$h_f = \frac{D}{2} \left(\frac{\gamma}{\sin\gamma}\right)^2 h(\gamma). \tag{4.12.14}$$

Equation 4.12.13 is the foundation of the fan-beam convolution back-projection algorithm for the equiangular rays geometry.

In case of equally spaced detectors array (equidistant rays), the final equation is slightly different, due to differences in mathematical manipulation:

$$f(r, \phi) = \frac{1}{2} \int_0^{2\pi} \frac{1}{U^2} \int_{-\infty}^{\infty} \frac{D}{\sqrt{D^2 + t^2}} P_f^{(ed)}(t, \beta) h_f(t' - t) \, dt \, d\beta, \tag{4.12.15}$$

where: $P_f^{(ed)}(t, \beta)$ is an equidistant fan beam Radon transform and:

$$U = \frac{D + r\sin(\beta - \phi)}{D}, \tag{4.12.16}$$

$$t' = \frac{Dr\cos(\beta - \phi)}{D + r\sin(\beta - \phi)},$$

and t is shown in Figure 4.13.
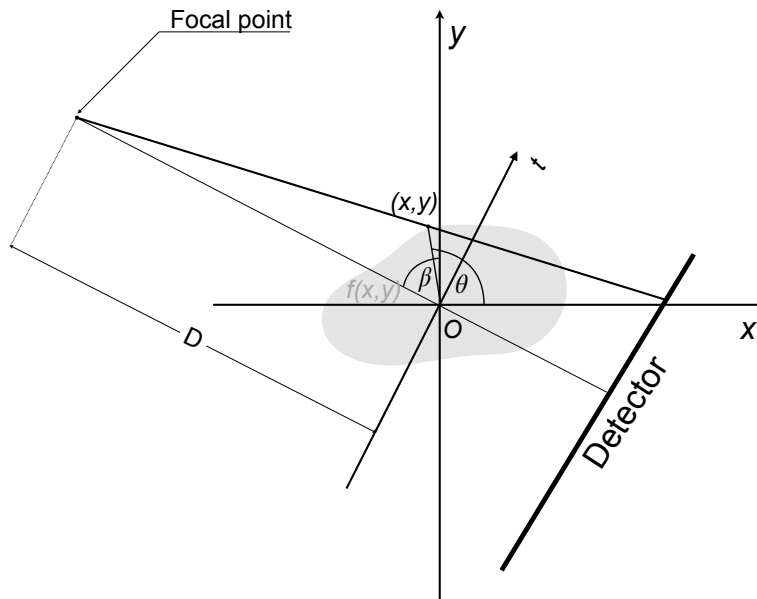
Figure 4.13 Equidistant fan-beam geometry.

In this case fan projections are represented in terms of distance t rather than angular location given by γ angle. The basic concept of the reconstruction however remains similar. More details on this second case can be found in [Kak 2001].

4.13 Cone beam tomography

Most of the conventional X-ray sources such as X-ray tubes produce a conical beam of radiation. Using such beams in CT has the main advantage of the reduction of time needed for projections collection. In this case, ray integrals are measured through every point in the object in the time it takes to measure a single slice in a fan-beam geometry. To present a method of topographic reconstruction in case of the cone-beam at first we have to extend the definition of projection to 3D case. A single ray in 3D is uniquely defined by the intersection of two planes:

$$s = x cos\theta + y sin\theta \qquad (4.13.1)$$

$$r = -(-x sin\theta + y cos\theta) sin\gamma + z cos\gamma \qquad (4.13.2)$$

A new coordinate system (s, t, r) is obtained by two rotations of the (x, y, z) coordinate system:

$$\begin{bmatrix} s \\ t' \\ r \end{bmatrix} = \begin{bmatrix} 1 & 0 & 0 \\ 0 & cos\gamma & sin\gamma \\ 0 & -sin\gamma & cos\gamma \end{bmatrix} \begin{bmatrix} cos\theta & sin\theta & 1 \\ -sin\theta & cos\theta & 0 \\ 0 & 0 & 0 \end{bmatrix} \begin{bmatrix} x \\ y \\ z \end{bmatrix} \qquad (4.13.3)$$

The first rotation is by θ angle around z axis to form (s, t, z) coordinate system, the second rotation is by γ angle around s axis (out of (s, t) plane) to form (s, t', r) coordinate system. These operations are illustrated in Figure 4.14.
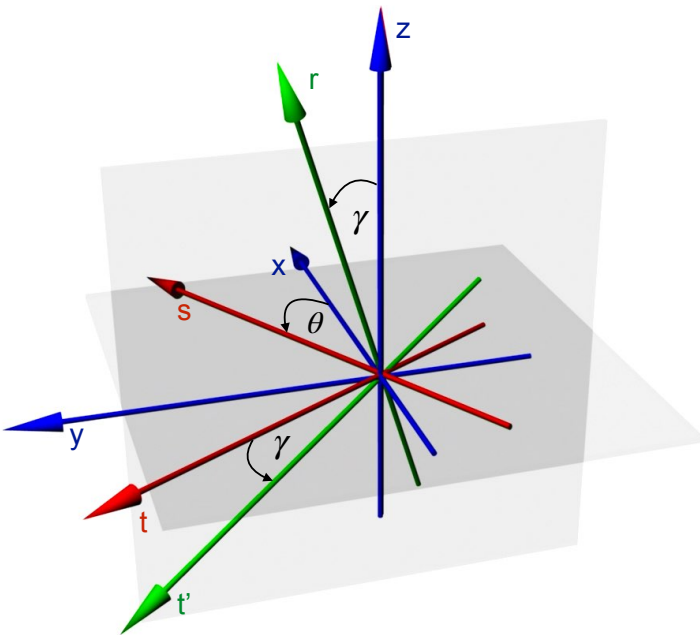
Figure 4.14 In the 3D cone beam tomography, to simplify geometrical considerations, the coordinate system is rotated. The first rotation of (x, y, z) system (in blue) is, as in the 2D case, by θ angle around z axis to form (s, t, z) coordinate system (in red). The second rotation is preformed by γ angle around s axis to form (s, t', r) coordinate system (in green).

A 3D parallel projection of the function f can be now expressed as:

$$P_{\theta,\gamma}(s, r) = \int f(s, t, r)dt \, . \tag{4.13.4}$$
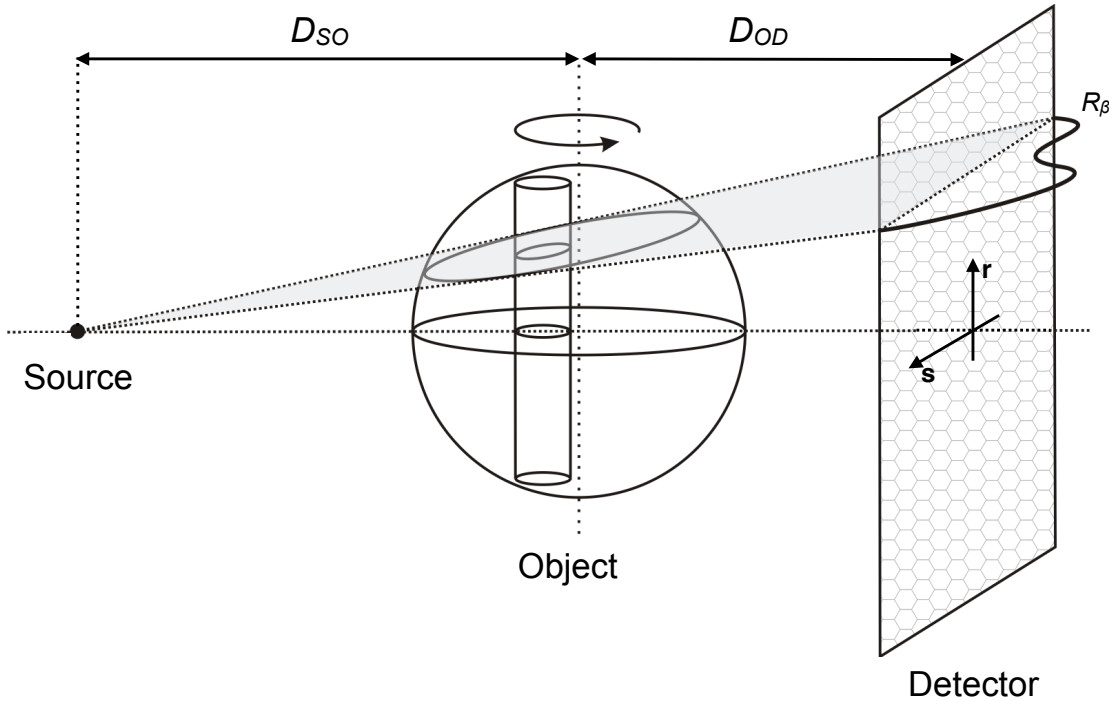
Figure 4.15 Geometrical layout of the cone-beam tomographic system. The detector measures the X-ray flux over a plane.

Now, we will present the most common method of reconstruction for the cone beam geometry. The method is often called FDK algorithm after the names of its creators: L. A. Feldkamp, L. C. Davis, and J. W. Kress [Feldkamp 1984]. The algorithm is an extension of the fan-beam reconstruction formula to the cone-beam case. It is based on filtering and back-projecting a single fan-beam plane within the cone. Each elevation in the cone is considered separately and the final 3D reconstruction is obtained by summing the contribution to the object from all the tilted fan beams. Thus, the basic idea of the FDK method is to apply weighted filter on the measured data along each row of the detector as if it were part of a 2D fan-beam acquisition and then to perform 3D back-projection. The method is fast and robust. However, the FDK method provides only an approximation of the reconstructed function. This is because the method is dedicated to the circular source trajectory (axial scan) and such a scan does not satisfy Tuy's conditions [Tuy, 1983]. More details on the Tuy's condition can be found in Appendix 9.4. Artefacts are especially pronounced at locations away from the orbit plane. They include reduction of reconstructed function values in the regions away from the orbit plane or cross-talks

between adjacent slices. In general, the exact results are achieved only at the orbit plane. Thus, the method provides better results if the angle of cone beam is small.

Because of the similarities with the fan-beam reconstruction method we start with the 2D equidistant fan-beam reconstruction formula for the point (r, ϕ) (Eq. 4.12.15), changing names for some of the variables:

$$f(r, \phi) = \frac{1}{2} \int_0^{2\pi} \frac{1}{U^2} \int_{-\infty}^{\infty} \frac{D_{SO}}{\sqrt{D_{SO}^2 + b^2}} P(b, \beta) h(b' - b) db d\beta, \tag{4.13.5}$$

where: $b' = \dfrac{D_{SO} r cos(\beta - \phi)}{D_{SO} + r sin(\beta - \phi)}$, $h(b) = \displaystyle\int_{-\infty}^{\infty} |\nu| e^{2\pi i \nu b} d\nu$, $U(r, \phi, \beta) = \dfrac{D_{SO} + r sin(\beta - \phi)}{D_{SO}}$, $\quad$ (4.13.6)

and D_{SO} is the distance from the centre of rotation to the source, as indicated in Figure 4.15.

The above equation can be simplified by replacing polar coordinate system (r, ϕ) by rotated (s, t) system. Using the following expressions:

$$s = x\ cos\beta + y\ sin\beta, \ \ t = -x\ sin\beta + y\ cos\beta \tag{4.13.7}$$

and

$$x = r\ cos\phi, \qquad y = r\ sin\phi \tag{4.13.8}$$

we can write:

$$r\ sin(\beta - \phi) = r(sin\beta cos\phi - cos\beta sin\phi) = y\ cos\beta - t - y\ cos\beta = -t \tag{4.13.9}$$

and

$$r\ cos(\beta - \phi) = r(cos\beta cos\phi + sin\beta sin\phi) = s - y\ sin\beta + y\ sin\beta = s\ . \tag{4.13.10}$$

Thus:

$$b' = \frac{D_{SO} s}{D_{SO} - t} \quad \text{and} \quad U(r, \phi, \beta) = \frac{D_{SO} - t}{D_{SO}}\ . \tag{4.13.11}$$

We can rewrite Eq. 4.13.5 using the above relationships:

$$f(s, t) = \frac{1}{2} \int_0^{2\pi} \frac{D_{SO}^2}{(D_{SO} - t)^2} \int_{-\infty}^{\infty} \frac{D_{SO}}{\sqrt{D_{SO}^2 + b^2}} P(b, \beta) h\left(\frac{D_{SO} s}{(D_{SO} - t)} - b\right) db d\beta\ . \tag{4.13.12}$$

There is one more step to obtain the formula for cone-beam reconstruction. In contrast to 2D fan beam reconstruction, in the cone beam case we have to tilt the fan beam out of the plane of reconstruction as it is shown in Figure 4.16. A new coordinate system (s, t') is defined to represent the location of the reconstructed point with respect to the tilted fan. When we move out of the central reconstruction plane, the size of the fan changes. Because of this fan size change, both D_{SO} and $d\beta$ change as well. The new source distance D'_{SO} is given by:

$$D'^2_{SO} = D^2_{SO} + \zeta^2,$$

(4.13.13)

where ζ is the height of the fan above the centre of the plane of rotation (measured along z axis as shown in Fig. 4.16.).

Since:

$$D_{SO}d\beta = D'_{SO}d\beta',$$

(4.13.14)

$$d\beta' = \frac{D_{SO}d\beta}{\sqrt{D^2_{SO} + \zeta^2}} .$$

(4.13.15)

Substituting D'_{SO} for D_{SO} and $d\beta'$ for $d\beta$ we obtain:
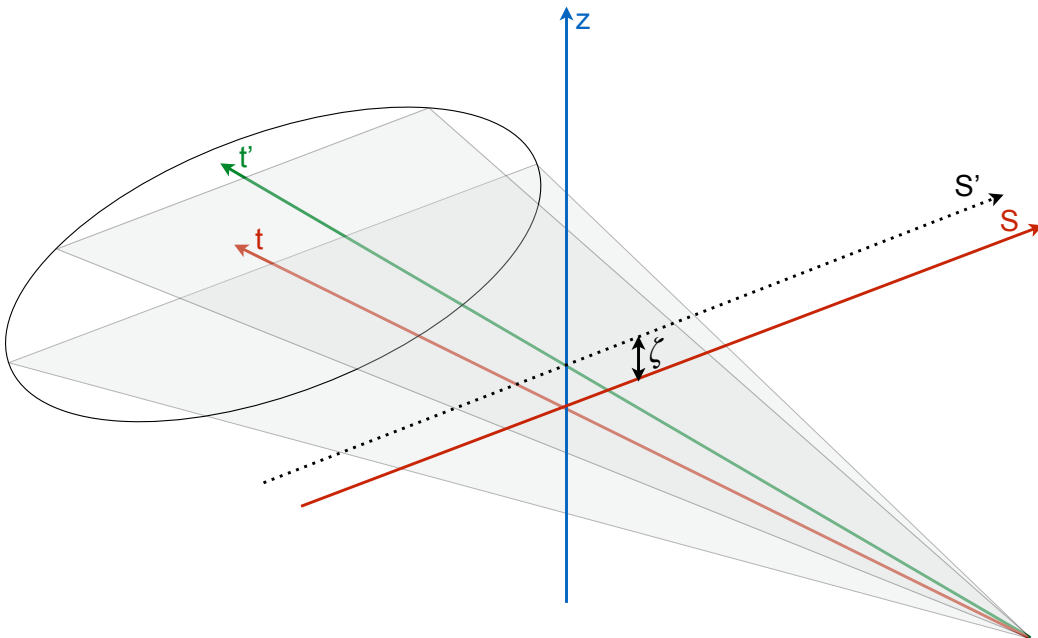
Figure 4.16 Two coordinate systems: (s, t) and (s', t'). The coordinate system (s', t') represents a tilted fan beam.

$$f(s', t') = \frac{1}{2} \int_0^{2\pi} \frac{D_{SO}'^2}{(D_{SO}' - t')^2} \int_{-\infty}^{\infty} \frac{D_{SO}'}{\sqrt{D_{SO}'^2 + b^2}} P(b, \beta', \zeta) h\left(\frac{D_{SO}' s'}{(D_{SO}' - t')} - b\right) db d\beta', \qquad (4.13.16)$$

where we indicated that P depends on the height ζ.

We can return to (s, t, z) coordinate system using Eq. 4.13.14, Eq. 4.13.15 and the following relationships:

$$s' = s, \qquad \frac{t'}{D_{SO}'} = \frac{t}{D_{SO}}, \qquad \frac{\zeta}{D_{SO}} = \frac{z}{D_{SO} - t}. \qquad (4.13.17)$$

Finally, the formula for cone-beam reconstruction is given by:

$$f(s, t) = \frac{1}{2} \int_0^{2\pi} \frac{D_{SO}^2}{(D_{SO} - t)^2} \int_{-\infty}^{\infty} \frac{D_{SO}}{\sqrt{D_{SO}^2 + b^2 + \zeta^2}} P(b, \beta', \zeta) h\left(\frac{D_{SO} s}{D_{SO} - t} - b\right) db d\beta. \qquad (4.13.18)$$

The pre-weighting factor $\dfrac{D_{SO}}{\sqrt{D_{SO}^2 + b^2 + \zeta^2}}$ is geometrically interpreted as the cosine of the angle between the ray and the central ray of the projection. The first term $\dfrac{D_{SO}^2}{(D_{SO} - t)^2}$ is identical to the $\dfrac{1}{U^2}$ factor in fan-beam back-projection (cf. Eq. 4.12.16). Pre-weighted projections are convoluted with the ramp filter h independently for each fan elevation ζ. Finally the pre-weighted and filtered projections are back-projected into three-dimensional reconstruction space. The flow of the FDK method is presented in Figure 4.17.

Pre-scaling the projections by the $\dfrac{D_{SO}}{\sqrt{D_{SO}^2 + b^2 + \zeta^2}}$ factor.

Row-by-row application of the ramp filter to the pre-scaled projection data.

Cone-beam back-projection of the pre-scaled and filtered data with a weighting function of the distance from the reconstruction point to the focal point.

Figure 4.17. The flow of the FDK method

4.14 Examples of application: X-ray microtomography

In this section a few selected applications of CT method will be presented. The following investigations were carried out using an X-ray microtomography system developed at the Institute of Nuclear Physics (Kraków, Poland). The system is composed of a microfocusing X-ray source, a sample positioning system and an X-ray sensitive CCD camera. The schematic layout of the experimental setup is shown in Figure 4.18. More details on the microtomographic system can be found in [Bielecki 2009].
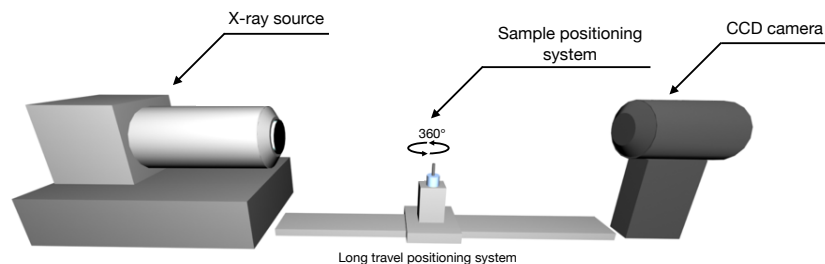
Figure 4.18. Schematic view of the X-ray microtomography setup

Investigations from several fields were carried out using the microtomographic system. In geo-science studies the following quantities have been determined: porosity, pore size distributions, specific area and tortuosity of rock samples [Bielecki 2013]. Combined microtomographic studies and Lattice Boltzmann calculations provided permeability tensors of the samples [Bielecki 2013]. Selected results are presented in Figure 4.19a-e. Material science investigations concerned imaging of foam materials based on carbon fibres, polylactic acid and tricalcium phosphate (Figure 4.20a-c). The X-ray microtomographic system was also used to image endocasts of human kidneys. More details on this topic can be found in [Drewniak 2011]. An example of the obtained tomographic images is presented in Figure 4.20.

The spatial resolution of the system based on the laboratory source is around 4 µm [Bielecki 2009]. The resolution is determined mostly by the spot size of the X-ray tube and the dimensions of a single element of the CCD detector. Higher resolution can be achieved using dedicated synchrotron beamline. Figure 4.22 shows a comparison of tomographic reconstruction of the same rock sample obtained using the laboratory system and the TopoTomo beamline of ANKA synchrotron (KIT, Karlsruhe, Germany) [Bielecki 2013]. The spatial resolution of images obtained using the synchrotron beamline was around 1 µm.

For the reconstruction of tomographic images obtained with the laboratory system the FDK cone beam algorithm was used, while in case of synchrotron-based images convolution back-projection for parallel beam geometry was applied.
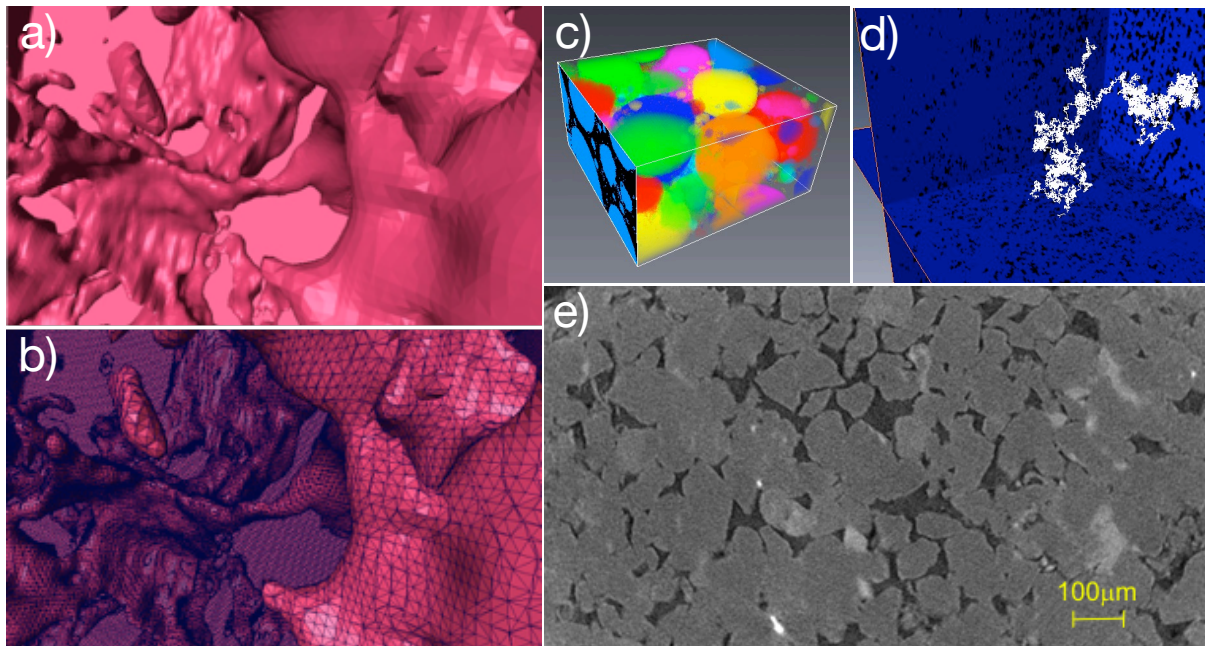
Figure 4.19 a) Internal structure of a porous rock sample, b) triangulation process to calculate the specific area of the sample, c) pore size distribution calculation, d) tortuosity calculation based on the random walk scheme, e) an example of reconstructed microtomographic slice of a rock sample (sandstone).
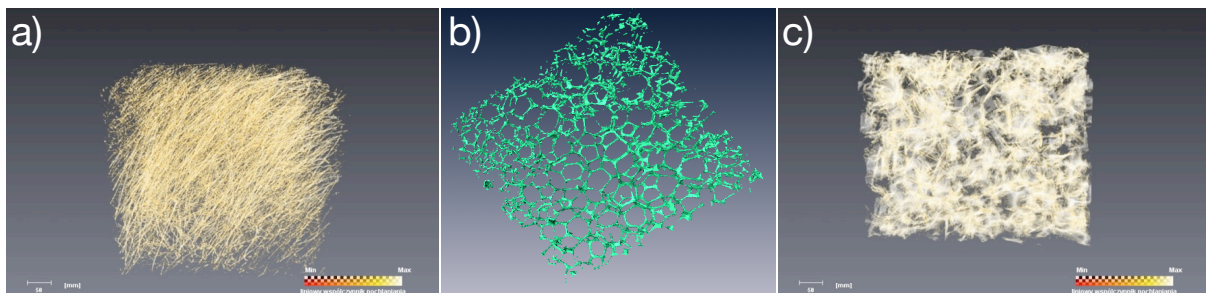
Figure 4.20 Microtomographic images of a) carbon fibre foam, b) polylactic acid-based foam material, c) tricalcium phosphate-based foam material.

Figure 4.21 3D tomographic reconstruction of human kidney endocast.
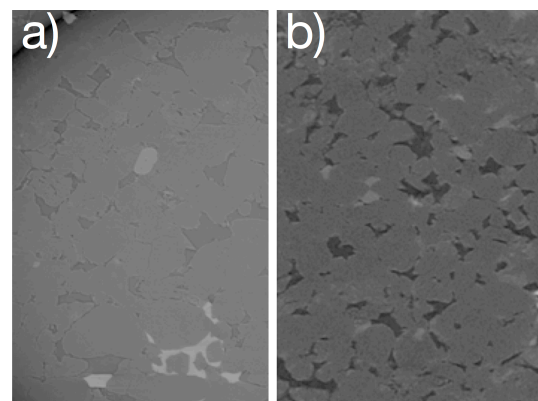
Figure 4.22 Reconstructed tomographic slice of a sandstone rock sample: a) synchrotron beamline, b) experimental setup based on microfocusing X-ray tube.

5. Algebraic Reconstruction Methods

In the preceding part of this book analytical methods, i.e. methods based on analytical transformations, were presented. This kind of reconstruction methods require a large number of projections. Moreover, ideally, the projections should be uniformly distributed over 180 or 360°. Often this condition is not fully fulfilled in classical (e.g. medical) CT and almost never in plasma tomography (see Section 6.2). An alternative approach to the tomographic reconstruction is based on algebraic manipulations. In this approach we assume that the searched function is represented by an array of discrete unknowns. Based on the measured projections, we can set up a system of linear algebraic equations for the unknowns. The reconstruction problem, in this case, consists in solving the system of equations. In this part of the book, we will at first introduce a set of linear equations where unknowns are elements of the object cross section. Then, we will present the Kaczmarz [Kaczmarz 1937] method for solving these equations. This approach applied to CT is often referred to as Algebraic Reconstruction Technique (ART). This will be followed by the several approximations that are used in this method to speed up its computer implementation.

5.1 Definition of the problem

Let $f(x, y)$ be the function to be reconstructed. We introduce a grid that is superimposed on the image function $f(x, y)$, as shown in Figure 5.1. We assume that in each cell function $f(x, y)$ is constant. Then, f_j denotes this constant value in the j-th cell, and N is the total number of cells. These steps are equivalent to introduction of the localised (pixel) basis set. Now, let us define the projections. In order to do that, we introduce rays of width τ as shown in Figure 5.1. A discrete line integral counterpart is now called a ray-sum. A projection will also have an index. Let p_i be the ray-sum measured with the i-th ray as shown in Figure 5.1. Then, the following relationship between f_j and p_i holds:

$$\sum_{j=1}^{N} w_{ij} f_j = p_i, \quad i = 1, 2, ..., M \tag{5.1}$$

where M is the total number of rays in all projections, and w_{ji} is the element of weighting (or contribution) matrix that represents the contribution of the j-th grid element to the i-th ray integral. The system of linear equation (Eq. 5.1) can be also written in the matrix form as:

$$\mathbf{Wf} = \mathbf{p}, \qquad (5.2)$$

where $\mathbf{f}$ is (N×1) column vector, $\mathbf{p}$ is (M×1) column vector and $\mathbf{W}$ is (M×N) matrix. The elements of $\mathbf{W}$ matrix can be constructed as the fractional area of the j-th image cell intercepted by the i-th ray, as shown for one of the cells in Figure 5.1. Note that most of the elements of $\mathbf{W}$ are zero, since only a small number of cells contribute to any given ray-sum. This implies that $\mathbf{W}$ is a sparse matrix.
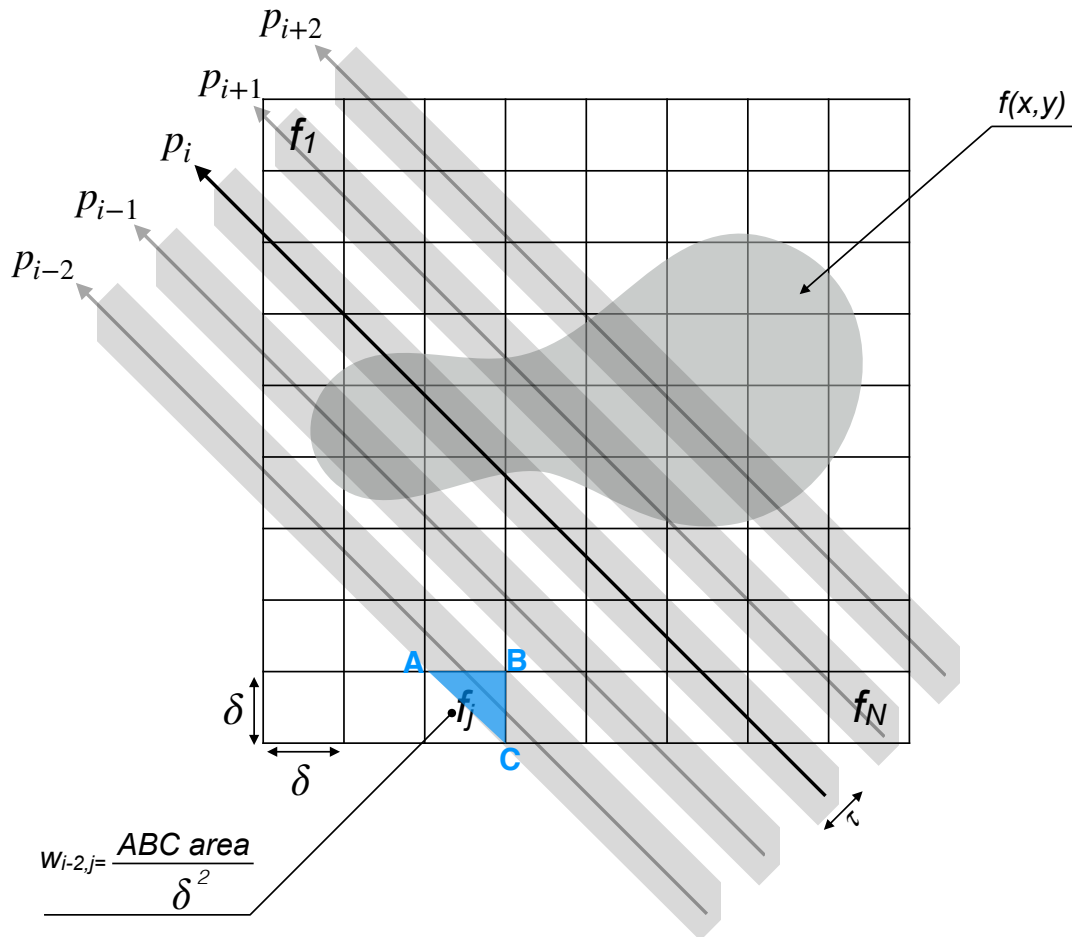
Figure 5.1 Definition of the problem in algebraic approach to tomographic reconstruction. An example of a weighting matrix element construction is also shown.

Now, let us focus on the solution of the system of equations. First of all, if both M and N were small we could use direct matrix inversion methods. In practice however, this is never true. For example, considering a moderate image resolution of 512×512 elements, N would be ~2.6×10^5 and M would also have the same magnitude. Furthermore, when $M < N$ and additionally projection data consists of measurement noise, direct matrix inversion is not possible and some least squares method must be used. However, when both M and N are large, such methods are also computationally impractical. In the next section a more efficient iterative Kaczmarz method is presented. Nevertheless, as will be shown later in the book, in highly ill-posed problems this method also fails and some kind of regularisation is required.

5.2 Algebraic Reconstruction Technique (Kaczmarz method)

In order to explain the principles of ART method, at first we have to note that the function $f(x,y)$ discretized on N grid cells has N degrees of freedom. Thus, the image to be reconstructed, represented by vector $\mathbf{f} = (f_1, f_2, \ldots, f_N)^T$, can be considered as a single point in a N-dimensional space. Each of the equations of the linear system (Eq. 5.1) represents a hyperplane in this N-dimensional space. If a unique solution exists, all these hyperplanes intersect in a single point that represents a desired solution. In order to simplify our considerations let us focus on a simple case of two variables only. Then, Equation 5.1 written down explicitly takes the following form:

$$\begin{cases} w_{11}f_1 + w_{12}f_2 = p_1 \\ w_{21}f_1 + w_{22}f_2 = p_2 \end{cases} \tag{5.3}$$

In this simple case of 2-dimensional space, hyperplanes are reduced to straight lines as shown in Figure 5.2. The ART method starts with an initial guess, e.g. vector $\mathbf{f}^{(0)}$ is selected in the random manner (the superscript denotes the iteration number). In the next step, this initial vector is projected onto the first line. Then, the resulting point is again projected on the second line and this procedure continues as shown in Figure 5.2. If a unique solution exists (i.e. if the two lines intersect), this iterative procedure will always converge to that point. The mathematical expression for $\mathbf{f}^{(k)}$, where k is the iteration number is given by:

$$\mathbf{f}^{(k)} = \mathbf{f}^{(k-1)} - \frac{\mathbf{f}^{(k-1)} \cdot \mathbf{w}_i - p_i}{\mathbf{w}_i \cdot \mathbf{w}_i} \mathbf{w}_i, \tag{5.4}$$

where $\mathbf{w}_i = (w_{i1}, w_{i2}, \ldots, w_{iN})$ and '·' denotes the dot product.

The convergence speed of the method depends on the angle between hyperplanes. If the two hyperplanes in Figure 5.2 are perpendicular to each other, then for an initial guess of any point in the (f_1, f_2)-plane, it is possible to arrive at the correct solution in only two iterations. On the other hand, if the angle between two hyperplanes is small, many iterations may be required, depending on the initial guess, before the correct solution is reached.
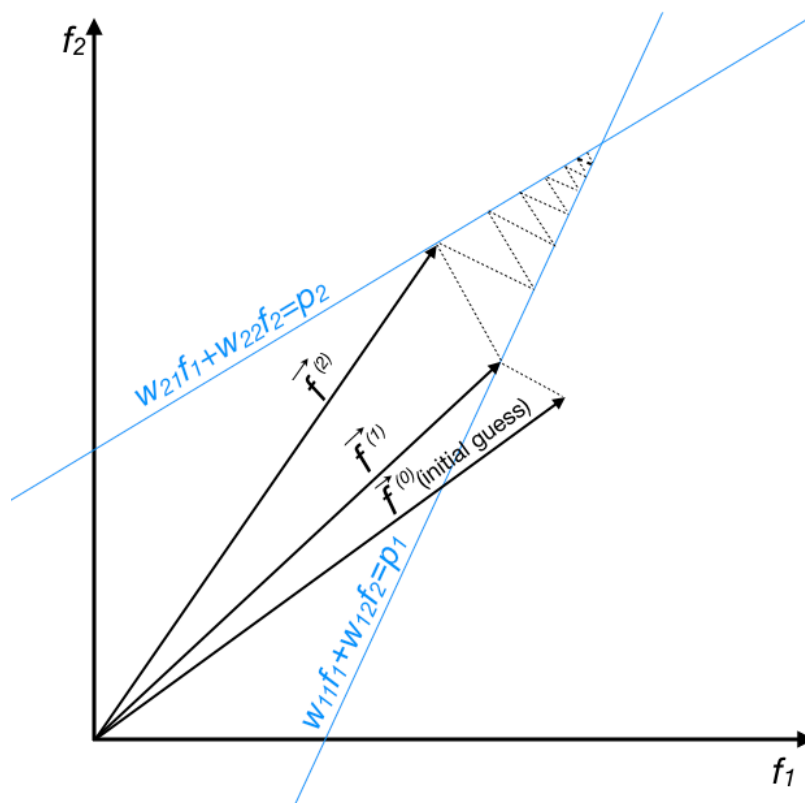
Figure 5.2 Illustration of the ART reconstruction problem in a simple case of two unknowns.

Sometimes, in the classical tomography we deal with the situation when $M>N$ (overdetermined system). Moreover, the projection set can be corrupted by noise. Obviously, no unique solution exists in this case. The ART solution then does not converge to a single point but rather oscillate in the neighborhood of the intersections of the hyperplanes [Kak 2001].

When $M<N$ (underdetermined system) a unique solution of the system of linear equations (Eq. 5.1) does not exist. In fact, an infinite number of solutions are possible. It can be shown however [Tanabe 1971] that for $M<N$ the solution obtained using ART converges to the minimum variance solution. The ART method is computationally efficient but it has also another important and attractive feature that will be discussed in detail

63

in the subsequent part of the book, when plasma tomography methods are considered. Namely, it allows, to some extent, to incorporate into the solution *a priori* information about the image that is to be reconstructed. For example, if it is known *a priori* that the image $f(x, y)$ is nonnegative, then in each of the solutions $\mathbf{f}^{(k)}$, successively obtained by using Equation 5.4, the negative components can be set to zero. Similarly, we can incorporate the information that $f(x, y)$ is zero (i.e. does not extend) outside a certain region or impose some smoothness constraint if these properties of the solution are known.

In order to discuss further some features of the ART method, let us rewrite Equation 5.4 in the following form:

$$f_j^{(k)} = f_j^{(k-1)} + \frac{p_i - q_i}{\sum_{l=1}^{N} w_{il}^2} w_{ij}, \tag{5.5}$$

where:

$$q_i = \mathbf{f}^{(k-1)} \cdot \mathbf{w}_i = \sum_{l=1}^{N} f_l^{(k-1)} \cdot w_{il}. \tag{5.6}$$

The above equation states that during an iteration the value in the *j*-th element of the image is corrected by:

$$\Delta f_j^{(k)} = f_j^{(k)} - f_j^{(k-1)} = \frac{p_i - q_i}{\sum_{l=1}^{N} w_{il}^2} w_{ij}. \tag{5.7}$$

In Equation 5.7, p_i is the measured ray-sum along the *i*-th ray, while q_i can be considered as the computed ray-sum for the same *i*-th ray based on the *(k-1)*-th solution, as given by Equation 5.6. The correction $\Delta f_j^{(k)}$ to the *j*-th pixel is obtained by first calculating the difference between the measured ray-sum p_i and the computed ray-sum q_i, normalizing this difference by $\sum_{l=1}^{N} w_{il}^2$. Then this value is assigned to all image cells in the *i*-th ray, each assignment being weighted by the corresponding w_{ij}^2. Sometimes, in order to improve the reconstruction quality and to reduce the artifacts caused by noise in the projections, the relaxation technique is used. Then, each pixel is updated by $\alpha \Delta f_j^{(k)}$ rather than by $\Delta f_j^{(k)}$, where $\alpha \in (0,1)$. Sometimes, the relaxation parameter α is taken as a function of the iteration number, i.e. it becomes smaller with increasing iteration number.

Figure 5.3 shows a simple example of image reconstruction using ART. In this case the image is composed of four (unknown) elements only. For the iterative reconstruction, six ray-sums $(p_1, \ldots, p_6)$ are used. In every iteration, $\mathbf{f}^{(k)}$ vector is calculated. The computations converges after six iterations.
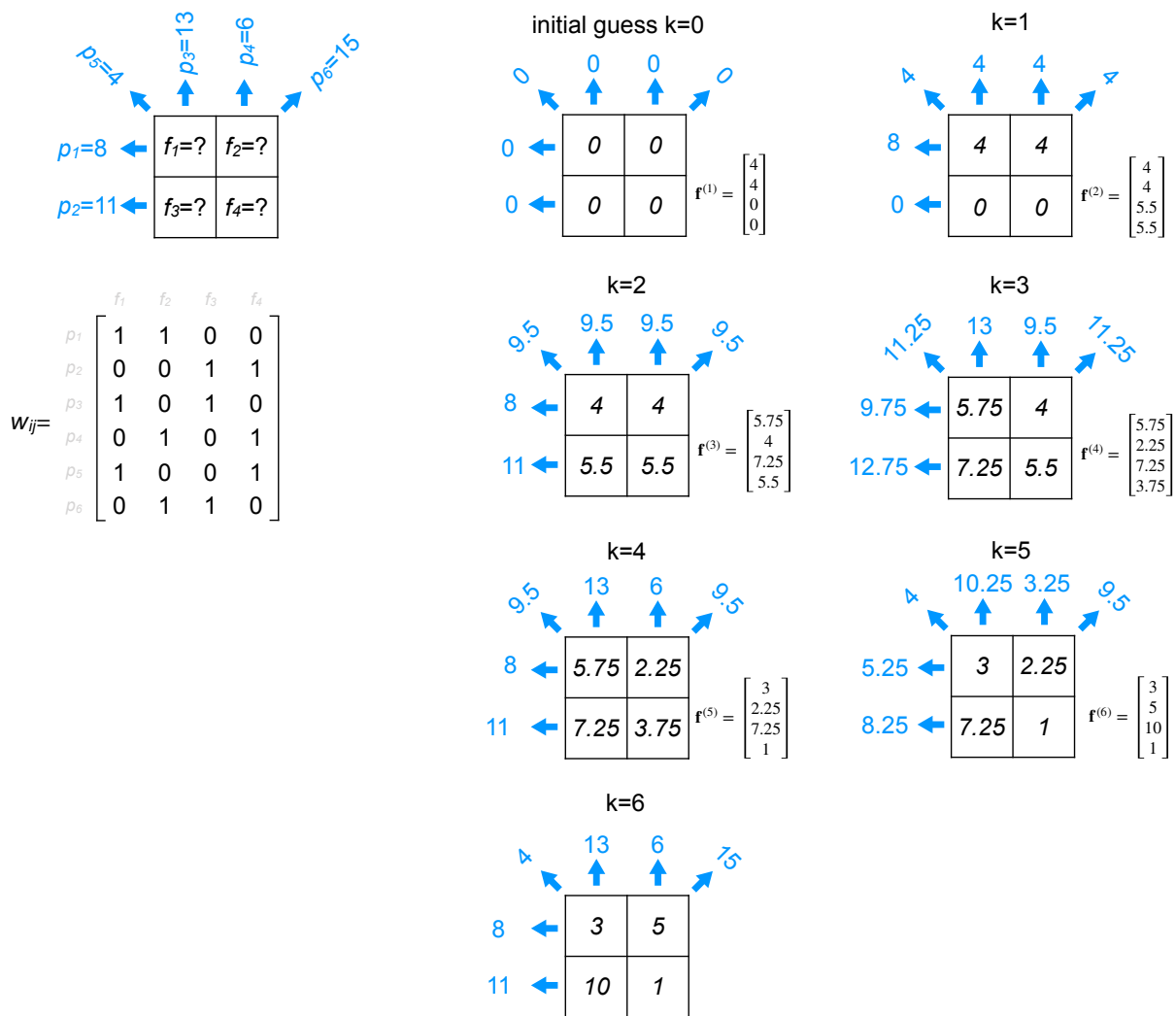
Figure 5.3 An example of application of ART for reconstruction of four pixel image.

Two another methods arise as variations of ART. In the Simultaneous Iterative Reconstruction Technique (SIRT) the changes in the *j*-th pixel are also computed using Equation 5.7. The difference is that before changing the value of *j*-th element, we go through all the equations and only at the end of each iteration the cell values are changed by the average value of all the computed changes for that element. This constitutes one iteration of the algorithm. In the second iteration, we go back to the first equation and the process is repeated. In another variant of ART method - Simultaneous Algebraic Reconstruction Technique (SART), several modifications were introduced to improve the quality of reconstructed images [Andersen 1984]. In order to reduce errors in the approximation of ray integrals of a smooth image by finite sums, the pixel basis was substituted by bilinear elements. Partial weights were assigned to the first and last image elements on the individual rays. In addition, a longitudinal Hamming window was applied to emphasize the corrections effective near the middle of a ray relative to those effective near its ends [Kak 2001].

6. Tomographic inversion in plasma physics

In this part of the book we will focus on the reconstruction method which are dedicated to plasma tomography. Even though we assume that the Reader has some knowledge on fusion science and plasma physics, we will start with a brief introduction to fusion physics and fusion devices. This part of the book can be treated as a refresher and can be omitted by the experienced Reader. Next, neutron, gamma-ray and X-ray detection systems in modern tokamak devices will be described with the special emphasis on technical aspects. In the subsequent chapters we will again focus on mathematical description, starting from the definition of the inversion problem in plasma physics through an introduction to ill-posed problems, ending with a detailed discussion on several methods specific to plasma tomography. Finally, practical examples of applications in the recent studies will be given.

6.1 A short introduction to fusion physics and fusion devices

In fusion reactions, low-mass nuclei fuse (i.e. combine), to form more massive nuclei. For example, in the reaction that naturally occurs in the Sun at a solar-core temperature of 14 million degrees, the nuclei of hydrogen (protons) fuse to form alpha particles trough the so-called proton-proton (p-p) cycle. After a fusion reaction, the total mass is less than before the reaction. The 'missing' mass is converted into energy, as quantified by the well-known Einstein equation:

$$E = \Delta m c^2, \tag{6.1.1}$$

where E is the energy released in the reaction, Δm is the nuclei mass difference before and after the reaction, and c is the speed of light in vacuum. Nuclei carry positive charges and if they have a low kinetic energy (at low temperature), they repel one another. In order to 'force' the nuclei to fuse, the particles involved must overcome this Coulomb barrier and get close enough for the attractive nuclear strong force to take over. This requires extremely high temperatures. In stars, when the p-p cycle is considered, the barrier can be penetrated with the help of tunnelling effect, allowing the process to proceed at lower temperatures than that which would be required at pressures obtainable in the laboratory. However, due to very low probability of quantum tunnelling, the extremely large number

of nuclei in stars generates fusion reactions over billions of years. In the laboratory experiments, the fuel must be heated to temperatures around 100 million degrees, to give the nuclei a high enough kinetic energy of thermal motion to overcome the force of repulsion of the positive charges and fuse. At this temperatures, electrons and nuclei are already separated and create an ionised gas called plasma. Since particles in plasma are charged, they conduct electricity and interact with magnetic fields. In somewhat simplified terms, the problem of producing fusion energy lies in development of a device that can heat the fuel to a sufficiently high temperature and then confine it for a time long enough so that more energy is released through fusion reactions than is used for heating. There are three commonly known approaches to fusion:

- Gravitational confinement. In this case, plasma is compressed to a high density and temperature by gravity. This confinement method requires a large amount of mass that can only be found in stars, thus it is impractical in laboratory applications.

- Inertial confinement. In this case, to initiate nuclear fusion reactions by heating and compressing a fuel target, usually high-energy beams of laser light are focused on a pellet that contains a mixture of deuterium and tritium. An example of realisation of this idea is the National Ignition Facility (NIF) - a large laser-based inertial confinement fusion (ICF) research device, located at the Lawrence Livermore National Laboratory in Livermore, California [Miller 2004].

- Magnetic confinement. Here, plasma is held away from the surface of experimental vessel by a combination of magnetic fields in a toroidal (doughnut-shaped) geometry and heated inductively, by radio-frequency waves or by injected fast neutral particles. The methods of plasma heating are described in more detail at the end of this section.

The most promising of these approaches is the magnetic confinement and the device which shows most promise for fusion is the tokamak [Sheffield 1994]. Thus, in this book, we focus mostly on applications of tomographic methods for tokamak plasma physics.

The primary fusion reactions possible to utilise in the future fusion reactors to harvest the energy are those involving light nuclei, such as the hydrogen isotopes deuterium D and tritium T:

$$D + T \rightarrow {}^4He + n + 17.6 \; MeV, \tag{6.1.2}$$

$$D + D \rightarrow {}^3He + n + 3.3 \; MeV, \tag{6.1.3}$$

$$D + D \rightarrow T + H + 4.0 \; MeV, \tag{6.1.4}$$

$$D + {}^3He \rightarrow {}^4He + H + 18.3 \; MeV. \tag{6.1.5}$$
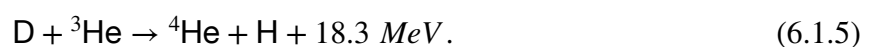
The two reactions involving as the reactants only deuterons (Eq. 6.1.3 and Eq. 6.1.4) occur with almost the same probability. The energy is released in the form of kinetic energy of the reaction products. The neutron carries 14.1 MeV and 2.45 MeV of energy for reaction 6.1.2 and 6.1.3, respectively. The most promising is the first reaction (Eq. 6.1.2). This is due to the fact that its cross-section is considerably higher at energies (temperature) achievable in the laboratory than for the other reactions. Figure 6.1.1 presents plots of the cross-sections for D-T, D-D and D-^{3}He reactions (in barns) as a function of nuclei energies (in keV). The character of the cross-section function for D-T reaction makes the future fusion power plants likely to operate with DT fuel. Deuterium can be quite easily obtained from sea water. The more problematic is tritium production. Tritium undergoes radioactive decay with a half-life of 12.3 years and therefore is not abundant naturally. It can however be produced from lithium in the following reaction:

$$^6\text{Li} + \text{n} \rightarrow {}^4\text{He} + \text{T} + 4.8 \; MeV. \tag{6.1.6}$$

Natural lithium, present in the earth crust, contains around 7.5% of ^{6}Li, thus T can be relatively easily produced inside a tokamak device equipped with a lithium blanket.

Figure 6.1 Cross-section for D-T, D-D and D-^{3}He fusion reactions. Based on National Physical Laboratory, Kaye & Laby data [NPL 2017].

The D–T reaction requires the input energy of at least ~10 keV and yields large output energy of 17.6 MeV. The 14.1 MeV neutrons produced in this reaction escape from the magnetic field due to their lack of electric charge and carry 80% of the fusion energy to the tokamak blanket. The neutrons kinetic energy is then converted into heat to drive electrical generators and to breed the tritium fuel, according to reaction 6.1.6. The other 20% (3.5 MeV) of the fusion energy is converted to kinetic energy of the helium ions. These energetic alpha particles, confined by the magnetic field, heat the plasma. In this way, a self-heating system can be obtained.

In the fusion reactor device, the net energy production should be positive. In fact, taking into account also the economical factors, the amplification factor Q (do not confuse with the reaction Q-value) defined as:

$$Q = \frac{P_{fus}}{P_{ext}},$$ (6.1.7)

should be greater then ~10-20 [Hamacher 2001]. In Equation 6.1.7, P_{fus} is the fusion power density and P_{ext} is the power density produced by external auxiliary heating systems. The condition when $Q \rightarrow \infty$ ($P_{ext} \rightarrow 0$) is called ignition. In this case, the thermal energy of the plasma is completely sustained by the nuclear fusion reactions. The condition of $Q = 1$ is referred to as breakeven. None of these conditions have been achieved so far in laboratory experiments.

The energy balance in a plasma can be described by a simple equation:

$$\frac{dW}{dt} = \bar{P}_{fus} + P_{ext} - P_{loss},$$ (6.1.8)

where W is the thermal energy density of the plasma, $\bar{P}_{fus}$ is the power density produced by the nuclear fusion reactions remaining inside the plasma which contributes to the plasma thermal energy and P_{loss} is the lost power density. The power density loss occurs due to two phenomena. First of all, the magnetic confinement is not perfect, thus particles and heat diffuse outside the plasma centre. The second reason of losses is bremsstrahlung radiation, produced when electrons in the plasma hit other charged particles, such as electrons or ions at a lower temperature, and suddenly decelerate. The power density lost by bremsstrahlung is proportional to $n^2 Z_i^2 \sqrt{T}$, where n is electron density, Z_i is ion density and T is plasma temperature. It is obvious that high-Z plasma impurities produce high bremsstrahlung losses.

Let us now focus on D-T reaction. Total fusion reaction power P_{fus} can be calculated as:

$$P_{fus} = E n_D n_T < \sigma v >,$$ (6.1.9)

where E is the energy produced in D-T reaction, n_D and n_T are deuterium and tritium ion densities, respectively, and $<\sigma v>$ is the so-called reactivity - a temperature dependent product between the cross-section σ of the reaction and the relative velocity v of the nuclei, averaged over the Maxwellian distribution. Figure 6.2 shows reactivity as a function of temperature for D-T, D-D and D-^{3}He reactions. The part of fusion reaction power density that remains in the plasma $\bar{P}_{fus}$ is given as:

$$\bar{P}_{fus} = \bar{E}n_D n_T < \sigma v > , \qquad (6.1.10)$$

where $\bar{E}$=3.5 MeV is the energy carried by the alpha particles in a DT reaction. Assuming that the fuel is composed of 50% of tritium and 50% of deuterium we have:
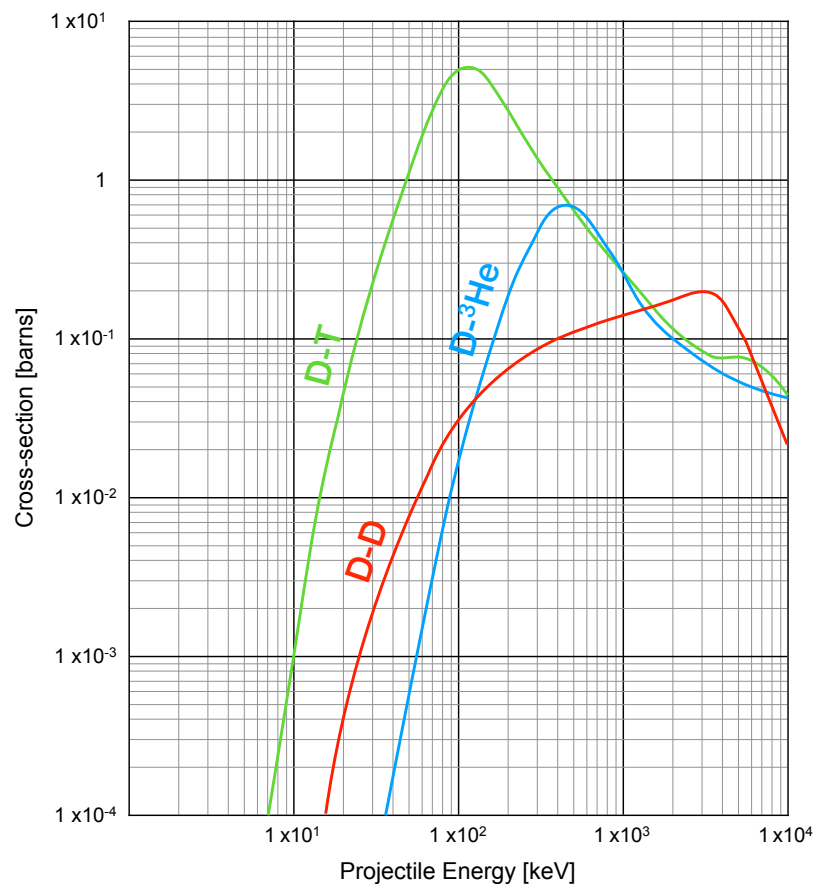
$$n_d = n_t = \frac{n_e}{2} . \qquad (6.1.11)$$
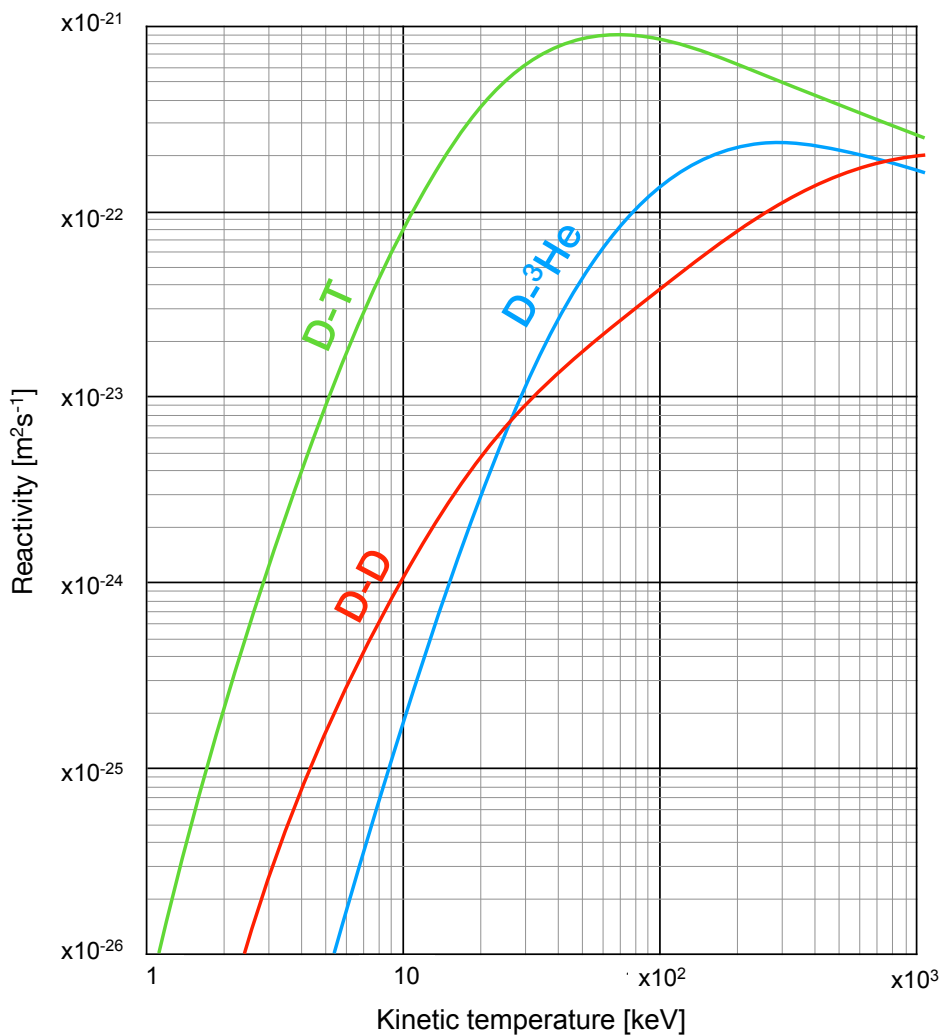
Figure 6.2 Reactivity for D-T, D-D and D-^{3}He fusion reactions. Based on National Physical Laboratory, Kaye & Laby data [NPL 2017].

Then, we can re-write Equation 6.1.10 as:

$$\bar{P}_{fus} = \bar{E}\frac{n_e^2}{4} < \sigma v > .$$ (6.1.12)

In order to gain energy by plasma, $\bar{P}_{fus} + P_{ext}$ must be grater than P_{loss}. In the special case, when power losses are exactly compensated by the external sources (i.e. $P_{ext} = P_{loss}$), plasma is in the stationary condition and its thermal energy remains constant. This situation is useful to define the energy confinement time - the characteristic time of thermal plasma energy dissipation:

$$\tau_E = \frac{W}{P_{loss}}.$$ (6.1.13)

The physical meaning of the above quantity is the time in which the plasma thermal energy is completely dissipated if the external heating sources are suddenly switched off.

Equation 6.1.8 leads to the Lawson's Criterion [Lawson 1957], that is very useful in studying of breakeven and ignition conditions. For DT plasma the Lawson's criterion for ignition states that:

$$n_e\tau_E \geq \frac{12}{\bar{E}}\frac{T}{<\sigma v>},$$ (6.1.14)

which, for temperature $T = 25\ keV$ (close to the minimum of $\frac{T}{<\sigma v>}$), gives:

$$n_e\tau_E \geq 1.7 \times 10^{20}\ m^{-3}\ s.$$ (6.1.15)

Today's fusion scientists use the triple product, more often than the above quantity, as their figure of merit. The triple product includes all three quantities: n_e, τ_E and T. Let us multiply both sides of Equation 6.1.14 by T:

$$n_e\tau_E T \geq \frac{12}{\bar{E}}\frac{T^2}{<\sigma v>}.$$ (6.1.16)

The quantity $\frac{T^2}{<\sigma v>}$ is a temperature dependent function with an absolute minimum at a slightly lower temperature than for $\frac{T}{<\sigma v>}$. For the DT reaction, the minimum of the triple product occurs at $T = 14\ keV$ giving the ignition condition:

$$n_e\tau_E T \geq 3 \times 10^{21}\ keV\ m^{-3}\ s.$$ (6.1.17)

So far, this condition has been never achieved in the present fusion reactors.

As it was stated before, among all existing concepts of fusion devices, the most promising so far is the tokamak machine. The other, competitive concept of fusion reactor based on magnetic confinement is the stellarator device. The interested reader is referred to a book by M. Wakatani [Wakatani 1998] for more details. The tokamak device design is shown in a simplified way in Figure 6.3. The device uses three superposed magnetic fields to confine fusion fuel. A ring-shaped field is produced by plane external coils. The second field comes from current flow in the plasma. The plasma current is induced by a transformer coil. This is the reason why tokamak devices work in a pulse mode rather than in a continuous one. An increasing current can be generated in the primary winding only for a limited time, thus current in the plasma can be driven also for the limited time. The field lines of the combined fields are then helical. A third, vertical field of outer coils is used for plasma positioning and shaping.
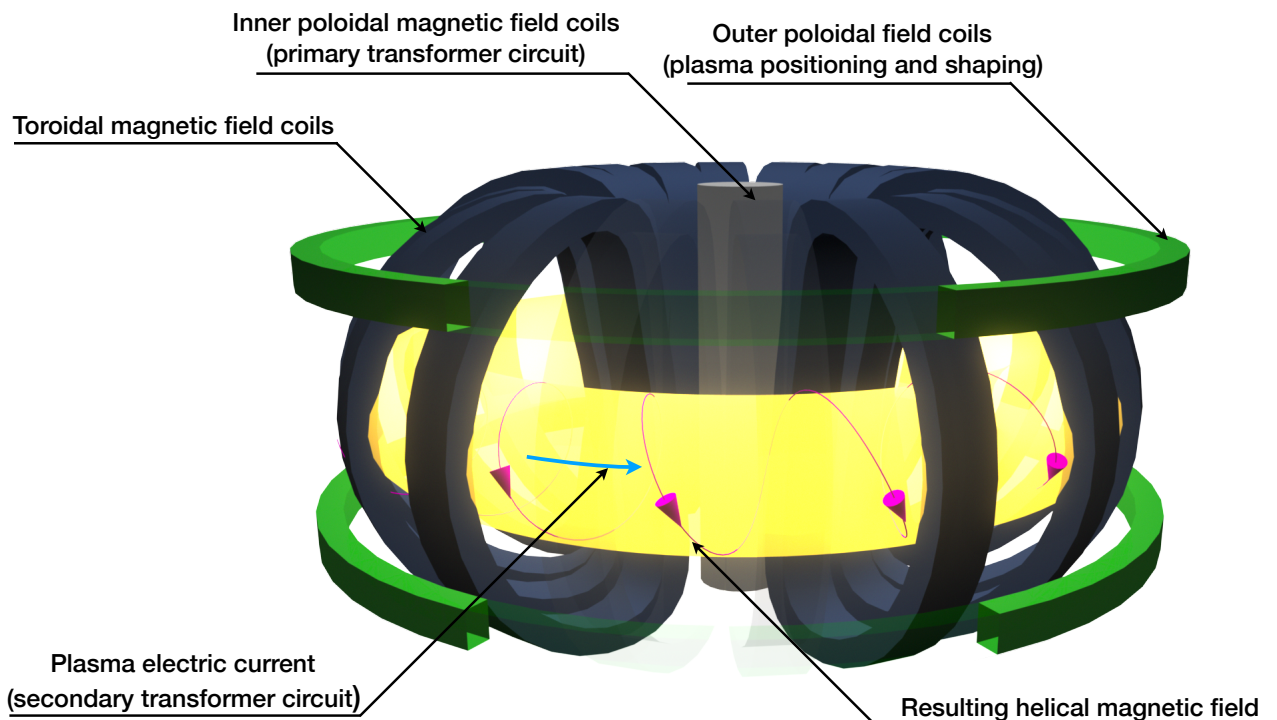
Figure 6.3 Simplified view of the tokamak device.

The induced current heats the plasma. This ohmic heating is limited by the fact that the electric resistance, which produces the heat, decreases with plasma temperature. The other non-inductive methods of plasma heating include: injection of neutral particle beam (Neutral Beam Injection - NBI) and plasma heating using electromagnetic waves of different frequencies.

In the NBI heating, positive ions (usually of hydrogen isotopes) are accelerated to high energies (>100 keV) via electric fields. As the ions cannot penetrate the magnetic field they must pass a neutraliser target where they capture electrons resulting in high energetic neutral atoms which subsequently enter the magnetic field of the tokamak (see Fig. 6.4). However, there is a balance between the rates at which the ions can be neutralised and re-ionisation by collisions. Thus, obtaining a completely neutral beam is not feasible. Unfortunately, the ionised fraction in the beam increases rapidly with increasing energy of the beam particles. The non-neutralised part of the beam is removed magnetically as shown in Figure 6.4. The neutral atoms that entered the plasma become ionised again due to collisions with plasma particles. These ions are much faster then average plasma particles. In a series of subsequent ion-ion, ion-electron and electron-electron collisions, the beam atoms transfer their kinetic energy to all plasma particles.
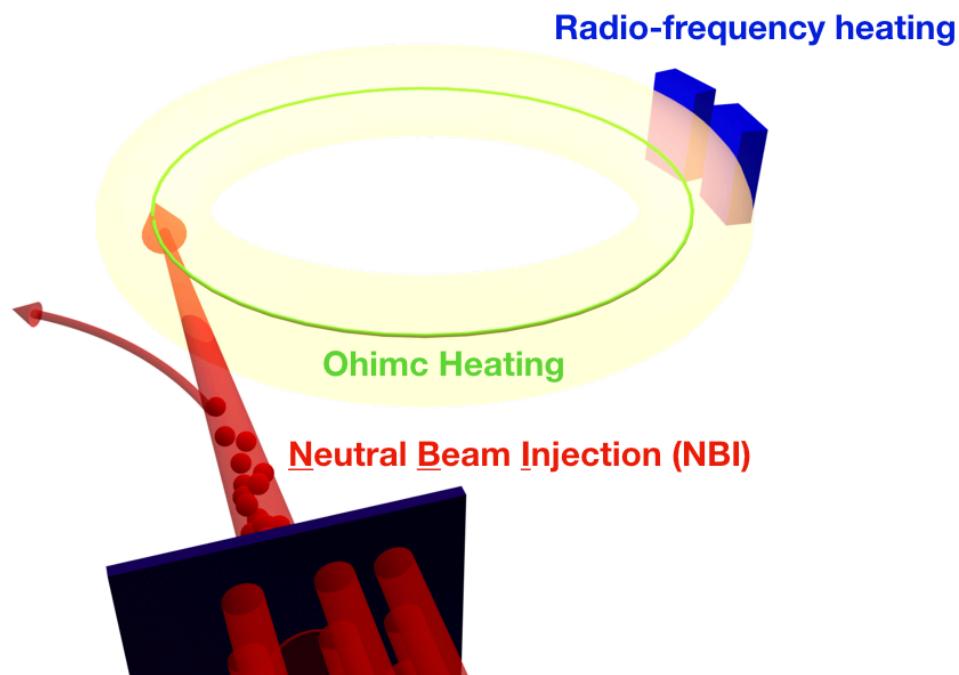
Figure 6.4 Schematic illustration of three methods of plasma heating: ohmic heating, injection of neutral particles and resonant radio-frequency wave heating.

The other method of plasma heating uses electromagnetic waves. In the plasma, ions and electrons gyrate around magnetic field lines. Electromagnetic waves of the specific frequency can resonate or damp their power to plasma particles. Gyro-frequency of the plasma particles depends on their charge and mass as well as on the magnetic field strength. The magnetic field decreases as $1/R$ in the plasma region, where R is the so-called major radius as shown in Figure 6.5. This allows to target certain particles by injecting waves of the respective frequency. The commonly applied Ion Cyclotron Resonant Heating (ICRH) relies on launching radio-frequency waves with frequencies
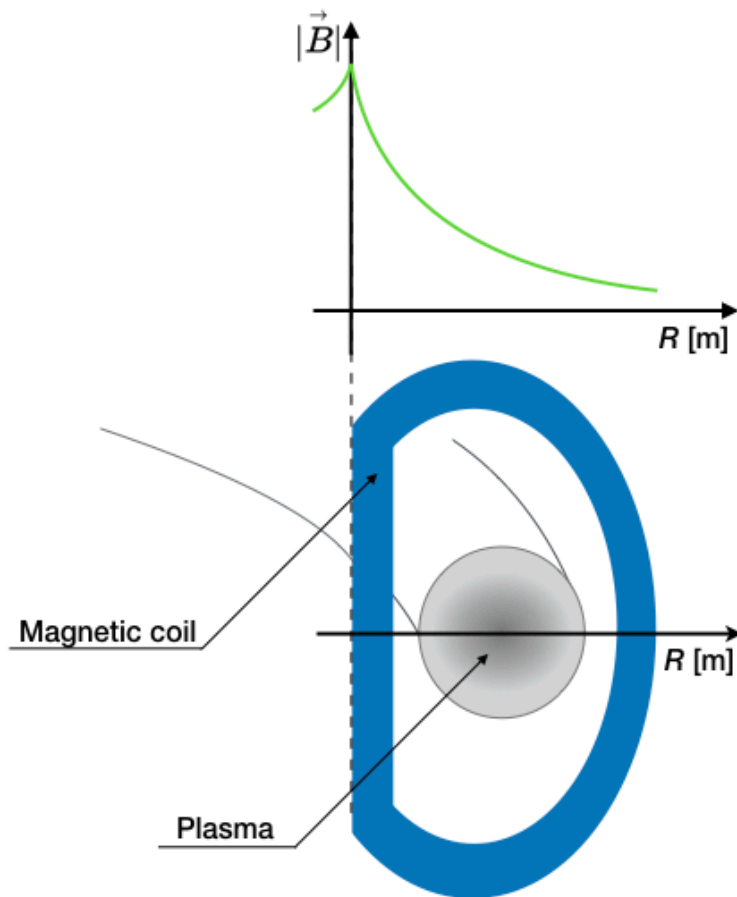
Figure 6.5 Magnitude of magnetic field in the tokamak device as a function of the major radius R.

equal to the cyclotron frequency of one of the ion species of the plasma or harmonics thereof (typically of ~20-60 MHz). The energy is transferred to the ions in resonant wave-particle interactions. Ion Cyclotron Resonant Heating method is of the key importance to the studies presented in Sec. 6.12. Another technique, Lower Hybrid Current Drive (LHCD) employs frequencies lying between ion cyclotron and electron cyclotron ones. LHCD has an inefficient heating effect. It can be used however to drive electric current [Jacquinot 1991].

6.2 Neutron, gamma and X-ray detection systems in modern tokamak devices

Modern tokamaks are equipped with numerous plasma diagnostic systems. Some basic diagnostics are based on time-resolved measurements, e.g. using fission chambers to determine total neutron yield from plasma. The other plasma diagnostics use dedicated neutron or gamma spectrometers of different types to extract information on physical parameters of plasma. In this section, we focus only on spatially resolved plasma diagnostic systems that allow retrieving information on neutron, gamma or X-ray emission.

These systems are of the special importance for DT plasma reactions, since the distribution of 14.1 MeV neutrons gives information on fusion reactivity and alpha particle profile birth. On the other hand, gamma rays of energy of 4.44 MeV, from interaction of alpha particles with Be plasma impurities in the reaction $^9Be(\alpha,n\gamma)^{12}C$, provide the profile of fast confined α-particles. Gamma rays of 17 MeV from $D(t,\gamma)^5He$ reaction, which is a weak branch of the DT reaction (Eq. 6.1.2), can give an independent assessment of fusion reactivity. Finally, the study of emission of hard X-rays of the energy > 20 keV provides an insight into the energy distribution function of runaway electrons [Shevelev 2013], while measurement of soft X-ray emission (0.1 - 20 keV) is a standard way of accessing valuable information on particle transport and magnetic configuration. Soft X-ray emission depends mainly on electron and impurity densities, as well as on electron temperature. This causes that, on one hand, soft X-ray analysis can provide valuable information of fusion plasma, but on the other hand such analysis is usually difficult to perform and therefore is often supported by numerical studies.

As it was described in the previous part of the book, in medical CT a finite, but relatively large number of projections is acquired by rotating the source and detector system around a patient. In tokamak devices however, such rotating system is not technically achievable and the tomographic inversion must be performed from a very limited number of projection directions. At JET tokamak, the neutron and gamma profile monitor (JET Gamma and Neutron Camera also called KN3) is used to obtain information on spatial distribution of neutron, gamma and hard X-ray emissivity. It consists of two cameras with 19 lines of sight in total. Each camera features three types of detectors. Liquid organic scintillators NE213, coupled to photomultiplier tubes, are used for neutron (2.45 MeV neutrons from DD reaction and 14.1 neutrons from DT reaction) and gamma rays detection. The detectors have neutron/gamma pulse shape discrimination capabilities. The second type of detectors is based on plastic scintillator Bicron-418 and is used to measure 14.1 MeV neutrons from DT reaction. The third detection system used for gamma measurements was equipped with CsI(Tl) photodiodes, but has been recently upgraded for the upcoming second deuterium-tritium campaign (DT2) and the detectors
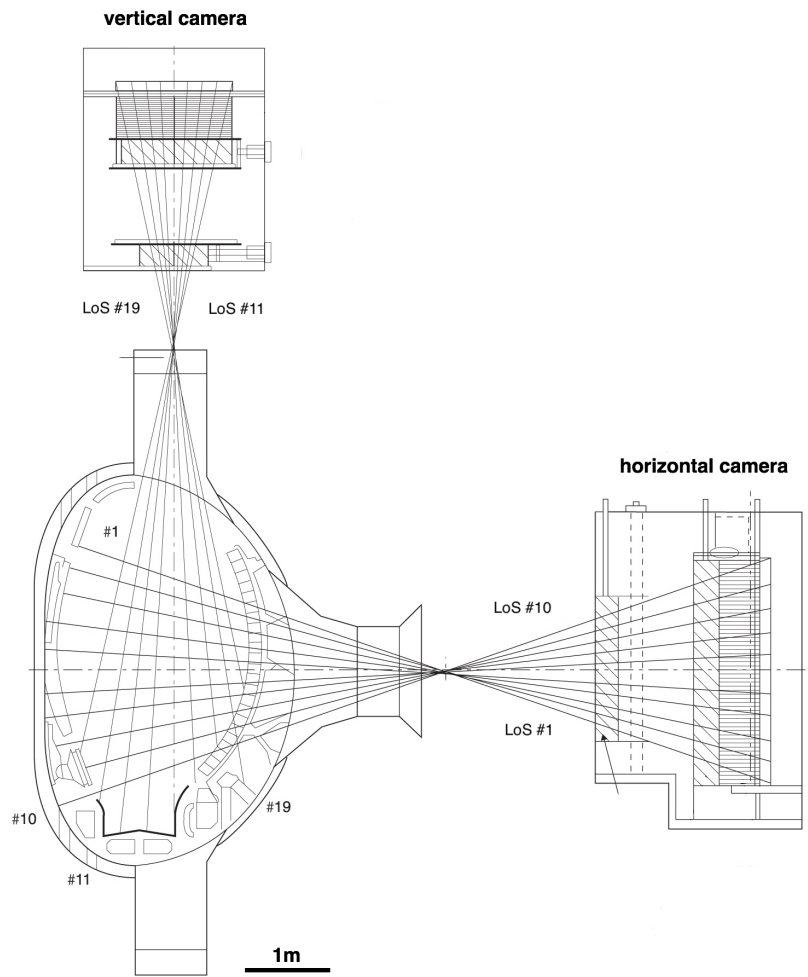
Figure 6.6 Geometrical layout of LoS of the neutron and gamma camera at JET tokamak [Kiptily 2006].

have been replaced by LaBr$_3$ scintillators combined with MultiPixel Photon Counters (MPPC) [Boltruczyk 2017]. This allowed to improve both the energy resolution (FWHM of a few % for 3–6 MeV gamma-rays) and count rate capability (up to 500 kHz). More information on this topic will be presented in Chapter 7. A poloidal cross section of the JET tokamak vessel, along with 19 lines of sight (LoS) of the camera, is shown in Figure 6.6. The plasma section covered by each LoS is about 20 cm diameter at the plasma centre.

WEST tokamak [Johnston 2017] has been recently equipped with a new soft X-ray detection system based on Gas Emission Multiplier (GEM) detectors. The system is designed to cover a poloidal section of the WEST tokamak. It is composed of two GEM detectors - one situated inside a port, with 83 LoS to observe plasma vertically, and the other located outside of a port, with 107 tomographic viewing lines to observe plasma horizontally. The primary aim of the diagnostic is metal impurities radiation

monitoring, especially tungsten emission, in 2–15 keV energy region. Additionally, the diagnostic system monitors MHD plasma activity in a 2D poloidal plasma cross-section. The system can achieve the temporal resolution of 1 ms with 1 cm resolved detection of plasma at the equatorial plane [Mazon 2015].

ASDEX Upgrade (AGU) tokamak [Neu 2009] is equipped with the soft X-ray tomographic system that has been operational since the year 2006. The diagnostic consists of 15 miniature heads with separate pinholes and chips assembled into 8 cameras. The system features 208 LoS in total. Each head works with a linear array of 35 diodes of size 4.6 × 0.96 mm^2 with 30 µm separation [Odstrčil 2016]. The spectral interval covered by the system ranges from 2.3 keV to about 13 keV. The spatial resolution of the system is about 7 cm.

Also many other tokamak devices, like JT60-U [Konoshima 2001], EAST [Xu 2012], KSTAR [Lee 2014], TCV [Anton 1996] or COMPASS [Mlynar 2012], have plasma diagnostic systems capable of plasma tomographic reconstruction.

6.3 Definition of the inversion problem in plasma physics

The task of tomographic reconstruction for thermonuclear plasma as a source of fusion neutrons, gamma rays or X-rays is very challenging due to ill-posed nature of the problem and sparse spatial resolution of the measured plasma projections. The sparse spatial resolution is a result of limited number of LoS available for the diagnostics. Thus, appropriate algorithms, suitable for the reconstruction from the limited data set, have to be used. Several approaches to plasma tomographic reconstruction have been developed, tested and applied on various machines. In this section we give a foundations of the problem, taking as an example neutron and gamma camera system at JET (see the information presented in Sec. 5.1). In the next section, the appropriate mathematical apparatus for solving and analysing of ill-posed problems will be presented. In the subsequent sections, we will go back to practical approach and applications.

The tomographic reconstruction is performed from the measured projections:

$$\int_{LoS} f(x, y) dl, \tag{6.3.1}$$

i.e., from the line integrals of the emissivity function $f(x, y)$, along the 19 straight LoS of the system presented in Fig 6.7. Here we assume that the detection system is placed in a poloidal cross-section of the plasma and its toroidal extension is small compared to the plasma dimensions (analogy to the fan-beam tomography). Moreover, we assume that the emissivity is axially symmetric in the toroidal direction. These assumptions are well fulfilled for the JET camera. The physical meaning of $f(x, y)$ is the neutron or photon (X-ray or gamma-ray) emissivity of the plasma, i.e. number of neutrons or photons emitted per plasma unit volume, per unit time. In practice however, it is a signal associated with neutron or photon that is directly measured by a detector and not the line integrated emissivity. Thus, to relate the measured signals to line integrated emissivity it is necessary to include a factor that takes into account several aspects. First of all, geometrical considerations, such as detector collimator geometry, detector solid angles and detectors LoS layout have to be taken into account. Then, properties of the detectors such as detection efficiency, energy thresholds and detector response functions have to be included. Finally, the information on scattering inside the detector collimator and the tokamak vacuum vessel should be taken into account as well. Usually, the precise translation of the count rate to the line integrals requires both experimental study of the detector response and Monte Carlo (MC) calculations of the radiation transport. Hereafter, we assume that we have the knowledge about the above-mentioned properties.

Let us assume now that we can discretise the emissivity function $f(x,y)$ on a grid of $N_H \times N_V$ elements, as shown in Figure 6.7. Each element is then associated to a value of the emissivity that is assumed to be constant within the pixel. There is a trade-off between the number of discrete elements given by N_H and N_V, defining the resolution of the reconstructed function $f(x,y)$, and the number of degrees of freedom of ill-conditioned problem.
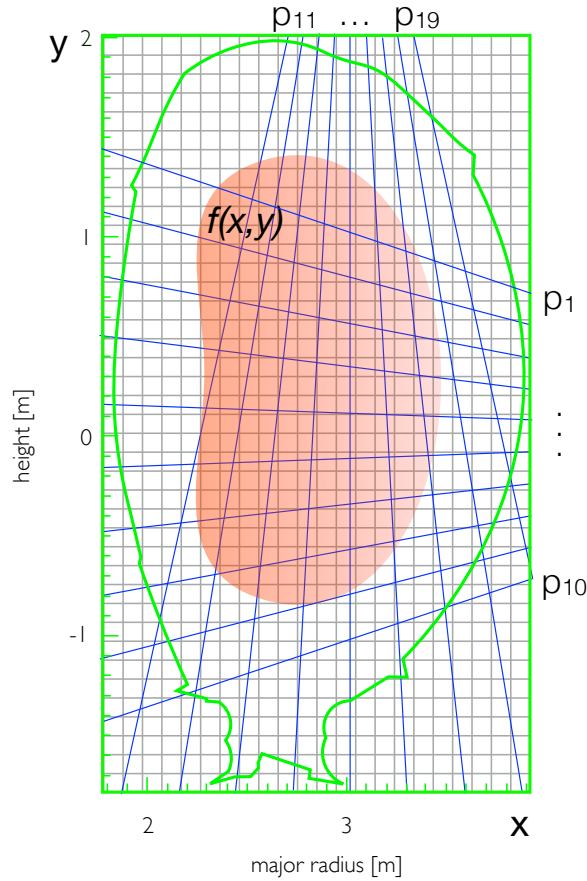
Figure 6.7 Discretisation of emissivity function f(x,y) on the reconstruction grid. The 19 LoS of the detection system are marked in blue,. The line integrals are determined based on measurements from the detectors set.

After discretisation, the inverse problem of tomographic reconstruction is defined by the set of linear equations:

$$p_k = \sum_{i=1}^{N_p} w_{ki} f_i, \quad k = 1...N_d. \tag{6.3.2}$$

In Eq. 6.3.2, f_i is the i-th element of the plasma emissivity represented by $N_p \times 1$ column vector $\mathbf{f} = (f_1,..,f_{N_p})^T$, $N_P = N_H N_V$ is the total number of elements for the discrete

79

representation of the neutron emissivity, $N_d = 19$ is the number of LoS, and p_k is the k-th element of $N_d \times 1$ column vector $\mathbf{p}$ that represents the available data along the LoS. The element w_{ki} of the geometrical matrix $\mathbf{W}$ (known also as weight or contribution matrix) represents the contribution of i-th element of emissivity to the k-th projection. The matrix $\mathbf{W}$ (of size $N_d \times N_p$) is constructed based on the detailed geometrical description of the diagnostic system defined by LoS geometry. Often, empirical correction factors mentioned before (for detectors efficiency, scattering contribution etc.) are included into the matrix elements. In the simple model, the values of w_{ki} elements of $\mathbf{W}$ matrix can be calculated as the polygonal intersection area between discretisation grid elements and the LoS width [Bielecki 2015]. In more complex cases, a full 3D model of LoS geometry can be considered to calculate elements of the geometrical matrix.

Due to the limited number of LoS, the tomographic reconstruction of the plasma neutron emissivity is an ill-posed problem. This is reflected in the matrix $\mathbf{W}$ which is ill-conditioned since its condition number, defined as the maximum ratio of the relative error in $f(x, y)$ divided by the relative error in $\mathbf{p}$, is large. Thus, standard reconstruction methods can lead to a solution that satisfies Eq. 6.3.2 but with no physical relevance.

Also, it is a well-known fact that the Algebraic Reconstruction Technique itself (presented in Sec. 5.2) does not provide, in general, physically meaningful results for undetermined, ill-posed problem of tomographic reconstruction of fusion plasmas [Ingesson 1998]. This is because the measurements themselves do not describe a unique solution and the solution is sensitive to noise. Therefore, regularisation is required by taking into account additional (*a priori*) information to obtain a single well-behaved solution. Using this extra information and constraints can, to some extent, compensate for the lack of experimental data and to select a realistic solution among all possible ones. Indeed, the regularisation is the key to obtain reliable and physically meaningful solution in plasma tomography. In the subsequent sections of the book, several complementary methods dedicated to plasma tomography will be presented.

6.4 Introduction to ill-posed inverse problems

A great number of problems from various branches of classical mathematics can be classified as ill-posed inverse problems, and since they are unstable and usually nonlinear, very often are considered as the most complicated ones. Similarly, ill-posed inverse problems are systematically studied in physics [Lavrent'ev 1986], geophysics [Zhdanov 2002], medicine [Fischer 2008], economics [Horowitz 2014], and many other areas of knowledge where mathematical methods are used. They play a key role in tomographic reconstruction of fusion plasma, where the inversion is inherently ill-posed.

Let us consider a matrix equation in the form of Eq. 6.3.2:

$$\mathbf{Wf} = \mathbf{p}. \tag{6.4.1}$$

The above equation is strictly related to the Fredholm integral equation of the first kind, which takes the following general form for functions defined on the interval [*a,b*]:

$$\int_a^b W(s,t)f(t)dt = p(s), \qquad a \le s \le b, \tag{6.4.2}$$

where the right-hand side p and the kernel W are given, and where f is the unknown solution.

The problem defined by Eq. 6.4.1 is well-posed (in sense of Hadamard [Hadamard 1902]) if:

• There exists some solution $\mathbf{f}$ *(existence),*

• There is only one solution *(uniqueness)*,

• The solution depends continuously on available input data $\mathbf{p}$ *(stability)*.

Otherwise the problem is ill-posed. To illustrate the issues connected with the ill-posed inverse problems, let us focus on the following simple and illustrative example.

Example:

The following system of linear equations is given:

$$\begin{cases} x_1 + 10\, x_2 = 11 + \epsilon \\ 10\, x_1 + 100.1\, x_2 = 110.1 \end{cases} \qquad (6.4.3)$$

Let us relate ϵ to some kind of noise that is inherently present in the input data. Then, if $\epsilon = 0$, $x_1 = x_2 = 1$, however if ϵ is small but $\epsilon \neq 0$, say $\epsilon = 0.1$, then $x_1 = 101.1$, $x_2 = -9$.

The solution is very sensitive to perturbation. Let us use the Singular Value Decomposition (see. Appendix 9.5) $C = U\Sigma V^T$ of the coefficient matrix $C = \begin{bmatrix} 1 & 10 \\ 10 & 100.1 \end{bmatrix}$ to investigate properties of the system:

$$U = V = \begin{bmatrix} -0.0994 & -0.9950 \\ -0.9950 & 0.0994 \end{bmatrix}, \qquad \Sigma = \begin{bmatrix} 101.0990 & 0 \\ 0 & 0.0010 \end{bmatrix}. \qquad (6.4.4)$$

Now we can clarify the definition of the condition number given in the previous section as the ratio of largest over smallest singular value (diagonal elements of Σ matrix):

$$Cond(C) = \frac{\sigma_1}{\sigma_n} \approx 1 \times 10^5. \qquad (6.4.5)$$

The ratio measures the degree of singularity of C. The larger this value is, the closer C is to being singular. The large condition number implies that the columns of C are nearly linearly dependent.

Note that we have to clearly distinguish ill-conditioning from round-off error. Conditioning is a property of the matrix itself and not the property of an algorithm or floating point precision of the computer used to solve the system.

The above example illustrates the properties of ill-posed problems. However, in tomographic reconstruction of fusion plasmas the situation is even more complicated because:

- Usually we deal with underdetermined problem (more unknowns than LoS),

- The geometrical matrix W is usually sparse (limited coverage of the space by LoS),

- The projection vector p (input data) contains a significant amount of noise. This is due to errors resulting from statistical fluctuations in the finite number of neutrons or photons

detected, described by a Poisson distribution, as well as the noise from other signal-independent sources (e.g. electronics noise from tokamak high power systems such as ICRH & NBI heating or LIDAR lasers).

The ill-conditioning of the tomographic reconstruction problem in fusion research implies that standard methods of numerical linear algebra (e.g. LU, Cholesky, or QR factorisation) for solving Eq. 6.3.2 cannot be used in a straightforward manner. Instead, more sophisticated methods must be applied in order to ensure the computation of a meaningful and physically sensible solution. This is the essential goal of regularisation methods. These methods incorporate further information (*a priori* knowledge) about the desired solution in order to stabilise the problem and select a useful and stable solution. This is the primary aim of regularisation.

In 1943, A. N. Tikhonov pointed out the practical importance of ill-posed inverse problems and gave the possibility of finding stable solutions for them [Tikhonov 1943]. Tikhonov regularisation is still the foundation of many methods applied in plasma tomographic reconstruction. Based on these foundations, other methods have been developed and applied. The idea behind Tikhonov regularisation is to define the regularised solution f_λ as the minimiser of the following weighted combination of the residual norm and the side constraint:

$$f_\lambda = argmin\left[\parallel \mathbf{Wf} - \mathbf{p} \parallel^2 + \lambda \parallel \mathbf{Lf} \parallel^2 \right], \tag{6.4.6}$$

where $\parallel \cdot \parallel$ denotes the Euclidean norm. In many cases, matrix $\mathbf{L}$ is chosen as the identity matrix ($\mathbf{W} = \mathbf{I}$), giving preference to solutions with smaller norms, or as a difference operator to enforce smoothness of the solution.

To explain further the idea behind the Tikhonov regularisation, let us consider the following simple and illustrative example.

Let us assume that the discrete function **f** to be reconstructed is composed of 3 elements only. Furthermore, only two measurements (projections) are available:

$$\mathbf{p} = \begin{bmatrix} 10 \\ 10 \end{bmatrix}. \tag{6.4.7}$$

This situation is schematically illustrated below.
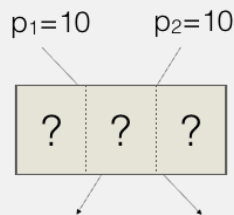
The ill-conditioned ($Cond(\mathbf{W}) \approx 200$) contribution matrix **W** is given as:

$$\mathbf{W} = \begin{bmatrix} 1 & 0.41 & 1.4 \\ 1 & 0.43 & 1.4 \end{bmatrix}, \tag{6.4.8}$$

The system of linear equations $\mathbf{Wf} = \mathbf{p}$ is underdetermined, with an infinite number of solutions. The solution that minimises the norm $\| \mathbf{f} \|^2$ is:

$$\mathbf{f} = \begin{bmatrix} 3.4 \\ 0 \\ 4.7 \end{bmatrix}. \tag{6.4.9}$$

Let us call this solution the *'exact'* solution. The *'exact'* solution can be illustrated as below.
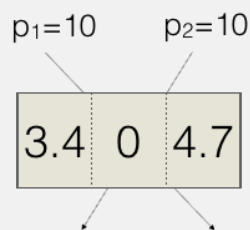
Now, let us add a small amount of noise to the measured projections **p,** such that the *perturbed* projection vector is given as:

$$\mathbf{p}' = \begin{bmatrix} 10.1 \\ 9.9 \end{bmatrix}. \tag{6.4.10}$$

The solution that minimises the norm $\| \mathbf{f}' \|^2$, obtained using the perturbed projections $\mathbf{p}'$ is:

$$\mathbf{f}' = \begin{bmatrix} 4.8 \\ -10 \\ 6.7 \end{bmatrix}. \tag{6.4.11}$$

It is obvious that the solution is far from what we expected (i.e. far from the *'exact'* solution) and it features a negative, non-physical element.
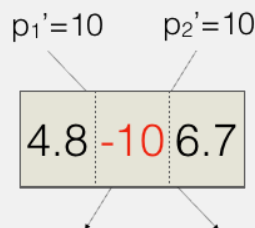
In the second case, the norm is definitively too big ($\| \mathbf{f}' \| = 12.6$) compared to the norm of the *'exact'* solution ($\| \mathbf{f} \| = 5.8$). Thus, the idea behind the regularisation is to make $\| \mathbf{Wf}' - \mathbf{p}' \|^2$ as small as possible (but actually not to minimising it), without $\| \mathbf{f}' \|$ becoming too big. Indeed, it can be achieved by minimising of the functional in Eq. 6.4.6. The table below summarises several solutions for different values of the λ parameter.

Table 6.1. Regularised solutions for different value of the λ parameter.

λ	$\mathbf{f}'$	$\| \mathbf{f}' \|^2$
0.01	$\begin{bmatrix} 4.2 \\ -6.1 \\ 5.9 \end{bmatrix}$	9.5
0.039	$\begin{bmatrix} 3.36 \\ 0.08 \\ 4.7 \end{bmatrix}$	**5.8**
0.05	$\begin{bmatrix} 3.3 \\ 0.5 \\ 4.62 \end{bmatrix}$	5.7
0.1	$\begin{bmatrix} 3.2 \\ 1.1 \\ 4.5 \end{bmatrix}$	5.6
1	$\begin{bmatrix} 2.7 \\ 1.15 \\ 3.85 \end{bmatrix}$	4.8

It is clear that by a proper choice of the λ parameter (e.g. $\lambda=0.039$), we can obtain the regularised solution that is very close to the '*exact*' solution. However, we have to know how to choose λ and choosing a proper value for λ can be challenging.

The regularisation parameter λ controls the weight given to minimisation of the side constraint relative to minimisation of the residual norm. A large λ (a large amount of regularisation) favours a small solution seminorm at the cost of a large residual norm, while a small λ (a small amount of regularisation) favours a small residual norm and a large solution seminorm. Thus, the regularisation parameter λ is an important quantity which controls the properties of the regularised solution. The proper choice of λ value is crucial for obtaining reliable and physically relevant results of the reconstruction. The regularisation parameter λ should be chosen with a special care. The next section presents a few methods of selection of optimal regularisation parameter λ.

6.5 Methods for selection of optimal regularisation parameter

One of the simple methods for selection of optimal regularisation parameter is the so-called L-curve method. It employs a plot, for all valid regularisation parameters, of the magnitude of the regularised solution $\| \mathbf{Lf} \|^2$ versus the magnitude of the corresponding residual $\| \mathbf{Wf} - \mathbf{p} \|^2$. The L-curve when plotted in log-log scale has usually a characteristic L-shaped appearance with a distinct corner separating the vertical and horizontal parts of the curve. The optimal choice of the regularisation parameter corresponds to the L-curve's corner [Hansen 1992]. Figure 6.8 shows the ideal form of the L-curve. Unfortunately, in some cases, the highly ill-posed character of the problem can cause the L-curve to be concave, and consequently, its L-vertex cannot be reliably defined.
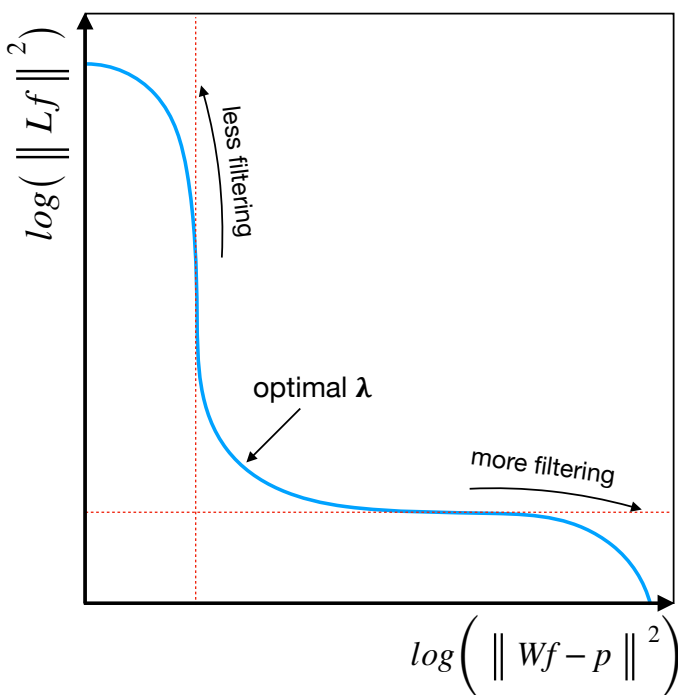
Figure 6.8 The ideal form of the L-curve. The corner corresponds to optimal choice of regularisation parameter

Another method is the Generalised Cross-Validation (GCV) technique [Golub 1979]. This approach is an extension of the ordinary Cross-Validation technique. The method is based on an idea that if one arbitrary element p_i of the projection (input data) vector $\mathbf{p}$ is left out, then the corresponding regularised solution (calculated using n-1 remaining measurements) should predict this element well and λ should be independent of any orthogonal transformation of $\mathbf{p}$. This leads to choosing the regularisation parameter which minimises the following GCV function:

$$G = \frac{\left\| \mathbf{W}\mathbf{f}_{\mathbf{reg}} - \mathbf{p} \right\|^2}{[Tr(\mathbf{I} - \mathbf{W}\mathbf{W}^{\mathbf{I}})]} \, . \tag{6.5.1}$$

In Eq. 5.5.1 $\mathbf{W}^{\mathbf{I}}$ is a matrix which produces the regularised solution $\mathbf{f}_{\mathbf{reg}}$ when multiplied by $\mathbf{p}$, i.e., $\mathbf{f}_{\mathbf{reg}} = \mathbf{W}^{\mathbf{I}}\mathbf{p}$. The trace in denominator can be easily computed using SVD.

The Morozov's discrepancy principle [Morozov 1984] can be used as well to select regularisation parameter λ, when some estimation ϵ of errors in the input projection vector $\mathbf{p}$ is known. Then, every solution that reproduces the projection within the errors is acceptable. However, the principle suggests to choose optimal $\lambda \geq 0$ such that:

$$\left\| \mathbf{W}\mathbf{f}_\lambda - \mathbf{p} \right\| = \left\| \epsilon \right\| , \tag{6.5.2}$$

i.e. such that the residual norm is exactly equal to the error estimate. In practice, the method requires finding the zero of nonlinear function and can be efficiently realised by SVD. Two remarks on the Morozov's discrepancy principle are necessary. First of all, in this approach λ is a function not only of the projection input data $\mathbf{p}$, but also a function of error magnitude ϵ. Moreover, the discrepancy principle selects λ as large as possible within given error bars, thus it tends to over-regularise the solution. In practice, for tomographic reconstruction of fusion plasmas, it means that if $\mathbf{L}$ matrix is related to a derivative operator, the solution can be over-smoothed.

Several less common methods have been also applied for selection of regularisation parameter in tomography, including extensions of L-curve method [Xu 2016], Predicted Residual Error Sum of Squares (PRESS) or Akaike information criterion (AIC) [Odstrčil 2016]. In practice however, the highly ill-posed character of the tomographic reconstruction problem causes that often the described methods fail. Then, more heuristic methods that include physical information from other plasma diagnostics must be applied. An example of such approach will be presented in the subsequent section of the book.

6.6 Reconstruction by Tikhonov regularisation
Based on J. Bielecki et al., Review of Scientific Instruments 86, 093505 (2015).

In this section an example of solving of Eq. 6.3.2 and hence performing tomographic reconstruction using Tikhonov regularisation will be presented. Let us focus on reconstruction of plasma neutron emissivity in case of JET tokamak using the detection system illustrated in Figure 6.6 (page 76).

The geometrical matrix $\mathbf{W}$ was calculated by considering the LoS of each detector projected onto the discretisation grid representing the plasma neutron emissivity cross-section. The values of w_{ki} elements of $\mathbf{W}$ matrix were calculated as the polygonal intersection areas between discretisation grid elements and the LoS width. The information on the geometrical layout of the KN3 LoS was provided by the SURFace reconstruction code. For the presented analysis, 2.45 MeV neutron emissivity profiles were used, acquired using the set of NE213 liquid organic scintillator detectors (each detector of 2.5 cm diameter and 1.0 cm thick). The signal from 2.45 MeV neutrons was separated from the gamma ray signals by pulse signal discrimination using the standard Charge Comparison (CC) method [Giacomelli 2014], while the 14.1 MeV neutron contribution from triton burnup process was negligible.

The correction factors taken into account during the construction of $\mathbf{W}$ matrix include: (i) neutron detection efficiency of NE213 detectors; (ii) neutron attenuation and scattering in the collimator; and (iii) neutron backscattering contribution. The absolute neutron detection efficiency of NE213 detectors for 2.45 MeV neutrons was determined as ~2.4×10^{-2} per neutron/cm^2 [Adams 1993]. Correction factors for the attenuation of the neutrons (as they pass through the tokamak vessel window and the material surrounding the neutron detector) as well as for the scattering of the neutrons in the collimators were calculated using the Monte Carlo N-Particle Transport Code (MCNP) modelling [Adams 1993]. For the horizontal camera, the correction is ~9% and for the vertical camera ~17.5%. The differences are due to the different thicknesses of the neutron attenuation materials between the plasma and the NE213 detectors. The correction factors for each collimator channel due to neutron backscattering were calculated using FURNACE code. For neutron energy of 2 MeV, the backscattered neutron contribution in the central camera channels (i.e., channels #5 and #14) is ~3% of the total incident neutron flux on the detector, while it is >75% for the outer channels (channels #1, #10, #11, and #19) [Adams 1993].

The ill-posed problem of the reconstruction can be solved using extra information and constraints to compensate, to some extent, for the lack of experimental data and to select a realistic solution among all possible ones. An example of such information

is the smoothness of the neutron emissivity solution. This means that the reasonable and physically realistic solution is obtained from the discretised neutron emissivity function, assuming it to be a smooth function, i.e., each element has no drastically different values compared to its neighbouring elements. The smoothness of the solution can be imposed either *a posteriori* or *a priori*. For instance, in [Craciunescu 2008], the neutron emissivity solution was obtained by post-processing, smoothing the reconstructed image of the neutron emissivity function. A smoothing operator was implemented as one-dimensional median filtering using a sliding window that moves on the magnetic contour lines. Thus, the smoothing operator was not integrated in the objective function.

In the presented example, instead, *a priori* knowledge upon the emissivity function is intrinsically included into the regularisation procedure, in order to avoid the post-processing of the solution. According to Tikhonov method, the solution of Eq. 6.3.2 is obtained by minimising the following functional:

$$min\left[\ \|\ \mathbf{Wf} - \mathbf{p}\ \|^2 + \lambda^2\ \|\ (\mathbf{L_1} + c\mathbf{L_2})\mathbf{f}\ \|^2\right],\qquad(6.6.1)$$

where, in this two-parameter case, λ controls the weight given to the minimisation of the side constraint relative to the minimisation of the residual norm, while parameter c controls the proportion between the terms related to $\mathbf{L_1}$ and $\mathbf{L_2}$ operators in the minimisation of the side constraints. Operator $\mathbf{L_1} = \nabla^2$ is a discrete approximation of the Laplacian that imposes a smoothness constraint of the reconstructed solution. The $\mathbf{L_1}$ operator can be written as a matrix of $N_H N_V \times N_H N_V$ elements (see Appendix 9.6):

$$\mathbf{L_1} = \begin{bmatrix} \mathbf{T} & -\mathbf{I} & 0 & \dots & 0 \\ -\mathbf{I} & \mathbf{T} & -\mathbf{I} & \dots & 0 \\ 0 & -\mathbf{I} & \mathbf{T} & \dots & 0 \\ 0 & 0 & -\mathbf{I} & \dots & 0 \\ \dots & \dots & \dots & \dots & \dots \\ 0 & 0 & 0 & \dots & \mathbf{T} \end{bmatrix},\qquad(6.6.2)$$

where $\mathbf{I}$ is an $N_V \times N_V$ identity matrix and $\mathbf{T}$ is the following $N_V \times N_V$ matrix:

$$\mathbf{T} = \begin{bmatrix} -4 & -1 & 0 & \dots & 0 \\ -1 & -4 & -1 & \dots & 0 \\ 0 & -1 & -4 & \dots & 0 \\ 0 & 0 & -1 & \dots & 0 \\ \dots & \dots & \dots & \dots & \dots \\ 0 & 0 & 0 & \dots & -4 \end{bmatrix},\qquad(6.6.3)$$

and N_H and N_V are the numbers of grid elements in the horizontal and vertical directions, respectively, as defined in Sec. 6.3.

In Eq. 6.6.1, $\mathbf{L_2}$ is a derivative operator along the magnetic flux contours which implies smoothness of the solution along the contours and the correct reconstruction of the shape of the neutron emissivity. The particular form of the $\mathbf{L_2}$ matrix has to be computed individually for every time interval of interest in the plasma discharge. Information on the magnetic configuration is obtained for a particular instance of time of JET discharge using the FLUSH software that helps to reconstruct the flux solution of the EFIT plasma equilibrium solver [O'Brien 1992]. In order to minimise the functional in Eq. 6.6.1 and to find the solution that regularises the reconstruction inverse problem, the Generalised Singular Value Decomposition (GSVD) was applied to matrices $\mathbf{W}$ and $\mathbf{L} = (\mathbf{L_1} + c\mathbf{L_2})$:

$$\mathbf{W} = \mathbf{U\Sigma X}^{-1}, \qquad \mathbf{L} = \mathbf{VMX}^{-1}, \tag{6.6.4}$$

where $\mathbf{U}$ is $N_d \times N_p$ orthogonal matrix, $\mathbf{V}$ is $N_p \times N_p$ orthogonal matrix, $\mathbf{X}$ is $N_p \times N_p$ nonsingular matrix, and $\mathbf{\Sigma}$ and $\mathbf{M}$ are $N_p \times N_p$ diagonal matrices:

$$\mathbf{\Sigma} = diag(\sigma_1, \ldots, \sigma_{N_p}), \qquad \mathbf{M} = diag(\mu_1, \ldots, \mu_{N_p}). \tag{6.6.5}$$

As previously, N_d and N_p refer to the number of available detectors and number of the discrete elements (pixels) of the reconstructed function $\mathbf{f}$, respectively.

The diagonal entries of $\mathbf{\Sigma}$ and $\mathbf{M}$ are non-negative, ordered as follows:

$$0 \leq \sigma_1 \leq \ldots \leq \sigma_{N_p} \leq 1, \qquad 1 \geq \mu_1 \geq \ldots \geq \mu_{N_p} \geq 0, \tag{6.6.6}$$

and normalised:

$$\sigma_i^2 + \mu_i^2 = 1, \quad i = 1...N_p. \tag{6.6.7}$$

They define the generalised singular values of the matrix pair $(\mathbf{W}, \mathbf{L})$ as ratios $\dfrac{\sigma_i}{\mu_i}$ (for $i = 1...N_p$) that reflect the level of ill-conditioning of the reconstruction problem. In Eq. 6.6.4, $\mathbf{U}$ and $\mathbf{V}$ are the matrices of singular vectors of the matrix $\mathbf{WL}^{-1}$. Using GSVD, the regularised solution is calculated as:

$$\mathbf{f}_\lambda = [\mathbf{W}^T\mathbf{W} + \lambda\mathbf{L}^T\mathbf{L}]^{-1}\mathbf{W}^T\mathbf{p} = \sum_{i=1}^{N_p} \frac{<\mathbf{u}_i, \mathbf{p}> \sigma_i}{\sigma_i^2 + \lambda\mu_i^2}\mathbf{x}_i, \tag{6.6.8}$$

where $\mathbf{x}_i$ is i-th column vector of $\mathbf{X}$, $\mathbf{u}_i$ is i-th column vector of $\mathbf{U}$, and $<.>$ denotes the inner product.

Since the standard methods described in Sec. 6.5 fail in this case, the optimal values of λ and c parameters are chosen through an iterative procedure. Additional *a priori* information is used to select the optimal regularisation parameters. The normalised electron density profile Γ_e was chosen as *a priori* information provided by JET LIDAR and High Resolution Thomson Scattering (HRTS) diagnostics [Gowers 2002, Maslov 2013]. For this purpose, several physical assumptions have to be made. First of all, it must be noted that the neutron emission from JET ohmic plasmas is very low and the major contribution to 2.45 MeV neutron emission comes from Neutral Beam Injection (NBI) heated plasma. This is because the cross-section for beam-thermal interaction is about two orders of magnitude higher than the cross-section for thermonuclear reactions. The neutron camera data thus consist mostly of signals from neutrons produced in beam-thermal deuterons fusion reactions. Furthermore, the quasi-neutrality condition of the plasma is assumed (i.e. the plasma electron density n_e is approximately equal to ion density n_i). The neutron rate from a given point in the plasma is related to the fuel density n_i at that point [Eriksson 2014] and also to electron temperature T_e, due to the dependency of the slowing down time distribution function of the beam-thermal component. Then, the assumption of quasi-neutrality plasma condition allows us to base the selection of regularisation parameters on the minimisation of the root mean square (RMS) difference between the normalised electron density profile Γ_e and the normalised reconstructed neutron emissivity profile Γ_n. The search of the optimal regularisation parameters is performed iteratively. In order to find the optimal couple of the parameters (λ^2, c), a scan in c is performed. Then, for a given c, the Golden Section Search (GSS) method [Teukolsky 2007] is applied to find the optimal λ^2.

The presented method was applied to reconstruct the neutron emissivity of deuterium plasma discharge (#85100) with varying NBI power scenario shown in Figure 6.9a. For this discharge, the maximum electron temperature T_e = 1.5 keV and the effective ionic charge Z_e during time interval 47.5–51.0 s was 1.13 ± 0.15. As input, the total number of neutron counts measured by the NE213 detectors was used. Figure 6.9a shows the total NBI power during the discharge recorded with the time resolution of 15.2 ms together with the total neutron yield measured by JET KN1 diagnostic with the maximal time resolution of 6 ms. KN1 is the main diagnostic system used at JET tokamak to measure the total neutron yield produced during the plasma discharges. It consists of three sets of [235]U and [238]U fission chambers placed around the machine [Swinhoe 1984]. Figure 6.9c shows the results of the reconstruction of the neutron emissivity for nine, 0.1 s long time intervals, corresponding to characteristic moments of the NBI power evolution. Figure 6.9b presents plots of the total neutron yield. measured by the fission chambers (down-sampled to time resolution of 0.1 s) and the maximum of the reconstructed neutron emissivity, calculated with the same time resolution. A good correlation of the reconstructed neutron emissivity with the total neutron yield measured independently by the fission chambers is observed (see Fig. 6.9b).
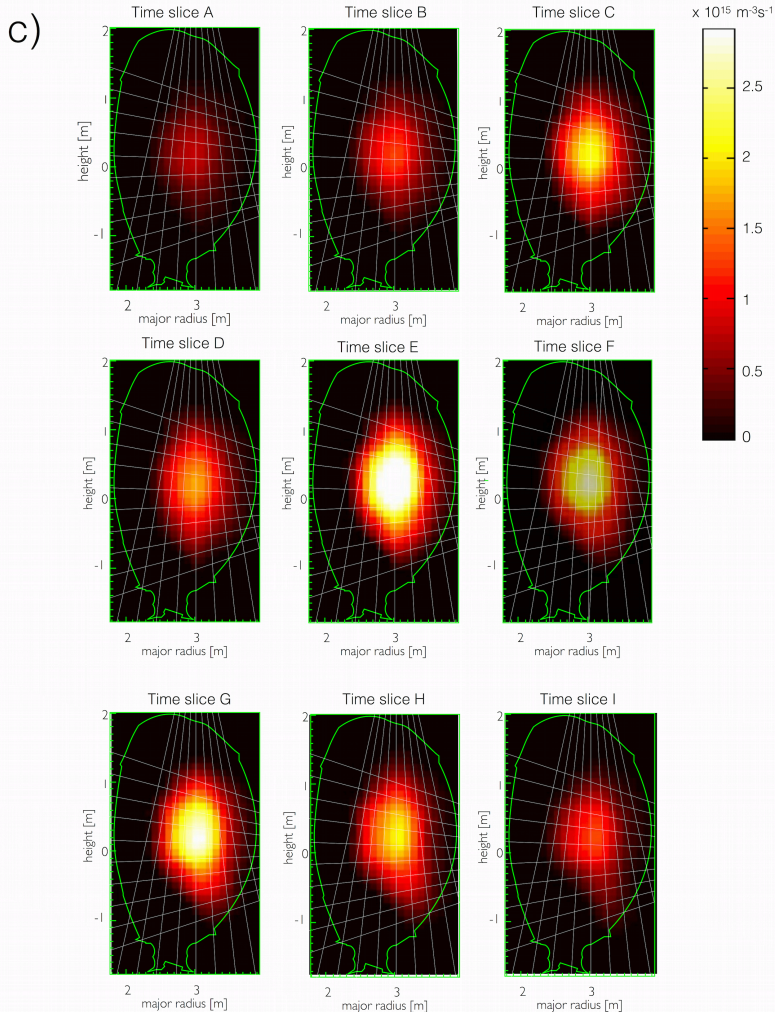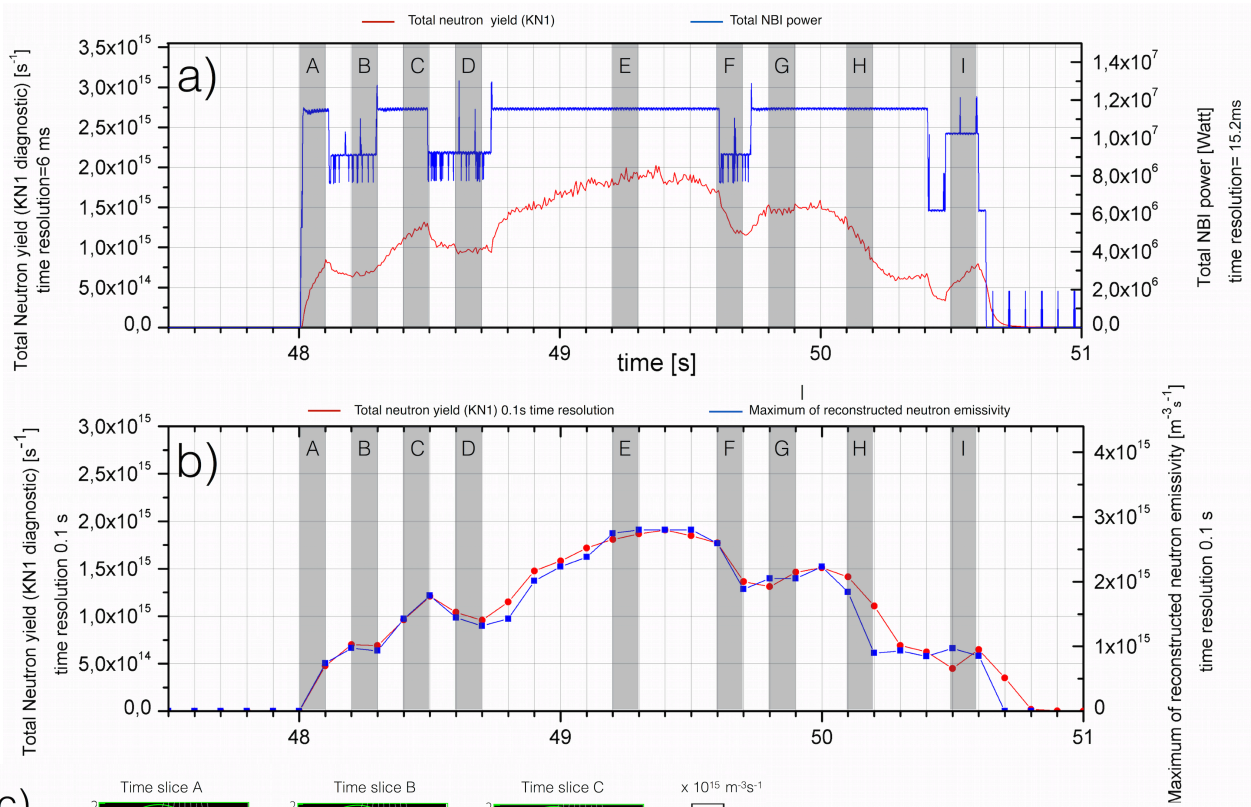
Figure 6.9 a) Total NBI power during the discharge (blue) and total neutron yield measured by the fission chambers (red) b) total neutron yield (red) measured by the fission chambers (down-sampled to time resolution of 0.1 s) and the maximum of the reconstructed neutron emissivity with the same time resolution (blue) c) results of the reconstruction of the neutron emissivity for nine, 0.1 s long, time intervals corresponding to characteristic moments of the NBI power evolution [Bielecki 2015].

A maximum neutron emissivity of 2.9×10^{15} m^{-3}s^{-1}, evaluated using the developed method and data provided by KN3 diagnostic, was observed during the time interval 49.2-49.3 s (E in Fig. 6.9b). Sudden drops of NBI power during time intervals 48.6-48.7 s (D) and 49.6-49.7 s (F) are clearly reflected in the plots of the reconstructed emissivity function and can be also noted in the plot of the maximum reconstructed emissivity (Fig. 6.9b). Lower emissivity of $\approx 0.75 \times 10^{15}$ m^{-3}s^{-1}, corresponding to the phase of switching on and switching off the NBI system can be observed during time intervals 48–48.1 s (A) and 50.5-50.6 s (I), respectively.

In general, the results of the performed reconstruction are consistent with the measurements of KN1 diagnostic. However, some discrepancies (e.g., Fig. 6.9b, time intervals: 48.7-48.8 s, 50.1-50.2 s, and 50.5-50.6 s) can be observed due to the coarse method of the regularisation parameters selection. Very occasionally, the regularisation parameters, selected automatically by the presented procedure, differ significantly from the actual optimal parameters. Then, the choice of (λ^2, c) can influence the results of the reconstruction. If selected (λ^2, c) are too small compared to optimal parameters, the reconstructed emissivity function can be under-smoothed (too highly peaked), which results in a too high maximum of the reconstructed emissivity. If (λ^2, c) are too large, the solution is over-smoothed with a too low maximum of the reconstructed emissivity. In general, the images of reconstructed neutron emissivity are not affected by severe artefacts. The plasma shape and its centre position can be clearly distinguished. However, minor artefacts can be rarely observed in the region of vessel covered by outermost LoS, monitoring plasma edges. In these regions, the neutron emissivity is mostly related to thermal plasma. However, this neutron contribution to the camera measurement is low and comparable to statistical noise.

The presented method based on Tikhonov regularisation uses the electron density profile shape as *a priori* information for the neutron emissivity profile shape. It was for the first time that the data from physical measurements of the tokamak diagnostics have been used to select the optimal parameters of regularisation. In this approach, the electron density profile was used, since it can be reliably measured at JET tokamak by LIDAR and HRTS diagnostics. However, the information on electron density profile could be substituted by the ion density and ion temperature distributions, providing that appropriate diagnostics will be available at a tokamak facility. In contrast with some methods reported previously, the one presented here does not include any post-processing of the obtained solution (e.g., no median filtering applied to the solution) and the physical constraints on the solution are imposed during the regularisation process. In several papers, complementary approaches to plasma emissivity reconstruction based on Tikhonov regularisation have been also reported [Iwama 1989, Terasaki 1999, Lee 2010, Wingen 2015].

6.7 Reconstruction by Minimum Fisher Information Method

Based on A. Jardin, D. Mazon and J. Bielecki, Phys. Scr. 91 044007 (2016).

In this section an alternative method for reconstruction of plasma emissivity is presented. The method is based on minimising of Fisher information (MFI) and will be presented in the context of soft X-ray (SXR) plasma emissivity reconstruction for Tore Supra tokamak. SXR in the range of 0.1–20 keV provides valuable information on tokamak plasma for studying e.g. magnetohydrodynamic activity, magnetic equilibrium or impurity transport [Vezinet 2014]. In particular, tungsten which is widely used as the main plasma facing material in major tokamaks such as ITER, JET or WEST, is a source of concern due to significant radiation losses in the plasma core and thus must be kept under acceptable concentrations. In this context, 2D SXR tomography is a useful tool to observe poloidal asymmetries of impurities and to provide a good estimate of their local concentration. In order to distinguish from neutron emissivity defined in the previous sections, the reconstructed SXR emissivity will be hereafter denoted as $g(x, y)$.

The SXR diagnostic used at Tore Supra tokamak is equipped with two fan-beam cameras. The horizontal camera consists of 45 LoS associated with one pinhole, while the vertical camera features 31 + 6 LoS associated with two pinholes. The geometrical layout of the diagnostic's LoS is shown in Fig 6.10. This configuration enables to obtain the spatial resolution of ~3 cm in the centre of the poloidal cross-section of the tokamak vessel. The diagnostic measures line-integrated profiles of the plasma SXR emission in the energy range of 3 - 25 keV. For this purpose the diagnostic is equipped with $N_d = 82$ silicon diodes accurately calibrated in their X-ray domain, including the electronics and geometrical correction [Mazon 2008]. The searched SXR emissivity is discretised on a square grid of 1.6 m × 1.6 m as a matrix of $N_p \times N_p$ square elements. Each element is associated to a value g_i of the SXR emissivity that is assumed to be constant within the pixel.

The inverse problem of SXR tomographic reconstruction between the emissivity $g(x, y)$ and» the line-integrated measurements p_k is defined, in analogy to Eq. 6.3.1, by the set of equations:

$$p_k = \sum_{i=1}^{N_p^2} w_{ki} g_i, \quad k = 1...N_d, \tag{6.7.1}$$

where w_{ki} are the coefficients of the geometrical matrix for the Tore Supra SXR diagnostic.
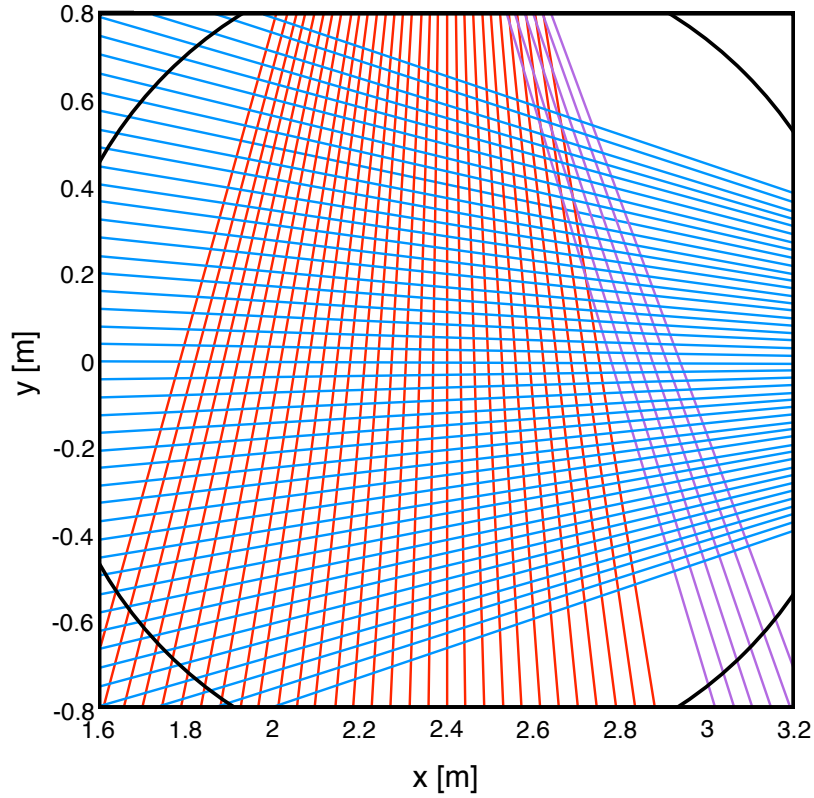
*Figure 6.10 Geometrical layout of lines of sight of Tore Supra SXR diagnostic [Jardin 2016].
The system features 31+6 vertical lines (in red and purple), associated with a camera
equipped with two pinholes and 45 horizontal lines (in blue), associated with
a single-pinhole camera.*

As it was shown in the previous sections, simple minimisation of the residuals
or the standard methods of tomographic reconstruction cannot be used due to
the ill-conditioned nature of the problem as well as presence of noise in the measured
data. The problem is also underdetermined, with only $N_d = 82$ projections compared
to the amount of information to retrieve, typically $N_p^2 = 400 \div 2500$.

To reconstruct SXR emissivity, similarly as in Sec 6.6, we rely on adding *a priori*
information on the expected emissivity profile and minimising the functional:

$$g_\lambda = argmin\left[\; \| \mathbf{Wg} - \mathbf{p} \|^2 + \lambda \; \| \mathbf{Lg} \|^2 \right], \tag{6.7.2}$$

where we used again the matrix representation. For the ordinary Tikhonov regularisation,
$\mathbf{L} = \mathbf{I}$ (zeroth order regularisation that minimises the solution norm), $\mathbf{L} = \nabla$ (first-order linear
regularisation that minimises the solution gradients), $\mathbf{L} = \nabla^2$ (second-order linear
regularisation that selects the solution with the least curvature) or $\mathbf{L}$ represents other types

of derivative operator as shown in the previous section. In MFI method however, $\mathbf{L}$ is associated with the Fisher information defined as the following integral:

$$I_f = \int \frac{g'(\mathbf{x})^2}{g(\mathbf{x})} d\mathbf{x}, \tag{6.7.3}$$

where $\mathbf{x} = (x, y)$. The above equation implies that the regions of low $g(x, y)$ have maximum information and hence minimum variance, thus become smooth, whereas smoothening is less pronounced in regions where $g(x, y)$ is high. Often, instead of solving the fully nonlinear problem (Eq. 6.7.2 with the objective function given by Eq. 6.7.3), a weighted linear regularisation method is used [Anton 1996]. Starting from first-order regularisation and introducing a positive diagonal weight matrix $\mathbf{F}$, the regularisation term for MFI method is defined as:

$$\mathbf{H}^{(n)} = \nabla^T \mathbf{F}^{(n)} \nabla, \tag{6.7.4}$$

where the superscript *(n)* denotes the iteration number. In order to minimise the Fisher information of the emissivity $g(x, y)$, we apply an iterative approach. We start with $\mathbf{F}^{(0)} = \mathbf{I}$ which is equivalent to the first-order linear regularisation. Then, we solve the normal equation (Eq. 6.6.8) to obtain $\mathbf{g}^{(n)}$:

$$\mathbf{g}_\lambda^{(n)} = [\mathbf{W}^T\mathbf{W} + \lambda\mathbf{H}^{(n)}]^{-1}\mathbf{W}^T\mathbf{p}. \tag{6.7.5}$$

Then, we use solution $\mathbf{g}_\lambda^{(n)}$ to construct elements of $\mathbf{F}^{(n)}$ matrix:

$$\begin{cases} \mathbf{F}_{ij}^{(n)} = \frac{1}{g_i^{(n)}}\delta_{ij} & g_i^{(n)} > g_{min} \\ \mathbf{F}_{ij}^{(n)} = \frac{1}{g_{min}}\delta_{ij} & g_i^{(n)} \leq g_{min} \end{cases}, \tag{6.7.6}$$

where δ_{ij} is the Kronecker's delta and $g_{min} > 0$ is the lower bound used for calculation of the weights. Any negative element $g_i^{(n)} < 0$ which could appear between two iteration steps is automatically set to zero to avoid unphysical solution. This iterative procedure continues until $\mathbf{g}^{(n)} \approx \mathbf{g}^{(n-1)}$. Then, $\mathbf{g}^{(n)}$ is taken as the solution.

For the selection of the regularisation parameter λ, the standard methods described in Sec. 6.5 can be used. However, due to the iterative nature of MFI method, the computational demands are higher and thus some simplified method of λ selection are often used [Jardin 2016]. One possibility is to use a fast empirical method based on the matrix traces:

$$\lambda^{(n)} = \frac{Tr(\mathbf{W}^T\mathbf{W})}{Tr(\mathbf{H}^{(n)})}. \tag{6.7.7}$$

Another possibility is to select the regularisation parameter such that smoothness of solution matches the noise level in measurements:

$$\frac{1}{N_d} \sum_k \frac{(p_k - p_k^{(rec)})^2}{\sigma_k} \approx 1, \tag{6.7.8}$$

where σ_k denotes the variance of the expected noise level on the k-th channel and $p_k^{(rec)} = \sum_i W_{ki} g_i$ is the signal at the i-th channel calculated based on the reconstructed emissivity.
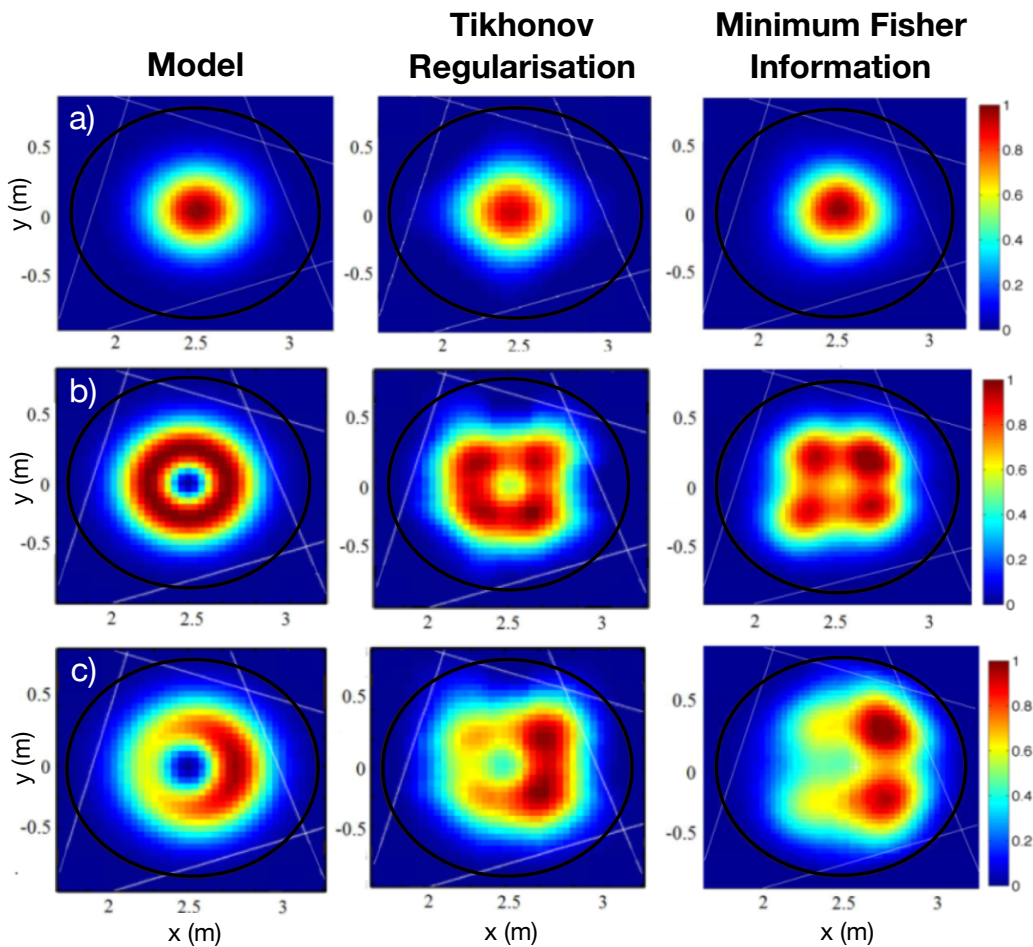
Figure 6.11 Comparison of reconstruction results of three plasma models performed with the second-order Tikhonov regularisation and Minimum Fisher Information method [Jardin 2016].

Figure 6.11 shows a comparison of reconstruction results for three simple plasma models obtained using two different reconstruction methods: second-order Tikhonov regularisation and Minimum Fisher Information method. Three phantom models were created and used to mimic the most commonly observed SXR emissivity distributions

in tokamak plasma. The phantom models include: Gaussian, hollow, and banana shapes. The simple Gaussian model is given by the following formula:

$$\mathcal{G}(x, y) = exp(-\frac{(x - \Delta x)^2}{2\sigma^2} - \frac{(y - \Delta y)^2}{2\sigma^2}), \quad (6.7.9)$$

where $(\Delta x, \Delta y)$ are the plasma centre coordinates and σ represents the standard deviation of the Gaussian. The hollow model is obtained by subtracting two Gaussian phantoms with the same emissivity centre but different variances $\sigma_1^2 > \sigma_2^2$:

$$\mathcal{H}(x, y) = \mathcal{G}_1(x, y) - \mathcal{G}_2(x, y). \quad (6.7.10)$$

Then, the banana model is derived from the hollow model by introducing a High-Field Side (HFS) poloidal asymmetry as follows:

$$\mathcal{B}(x, y) = \mathcal{H}(x, y)exp(-\frac{(x - \Delta x_{as})^2}{2\sigma_{as}^2} - \frac{(y - \Delta y_{as})^2}{2\sigma_{as}^2}), \quad (6.7.11)$$

where the point $(\Delta x_{as}, \Delta y_{as})$ denotes the centre of the asymmetry chosen on the corona of the corresponding hollow profile, and σ_{as} represents the asymmetry spatial extent. The phantom shapes were selected to model, in relatively realistic way, the commonly observed distributions of SXR emissivity. While the Gaussian shape represents emission of a thermal plasma, the banana phantom reflects more complicated cases of the SXR emissivity, such as impurity poloidal asymmetries. The hollow shape simulates SXR emissivity observed after a sawtooth crash. The results are also quantified by two figures of merits RMS_{em} and RMS_{pr} which represent root mean square error of the reconstructed emissivity and root mean square error of the projections, respectively, i.e.:

$$RMS_{em} = \sqrt{\frac{1}{N_p^2} \sum_i \left(g_i^{(mod)} - g_i^{(rec)} \right)^2}, \quad (6.7.12)$$

where $g_i^{(mod)}$ denotes the emissivity in the i-th element of the model, $g_i^{(rec)}$ is the emissivity in the i-th element of the reconstruction result,

$$RMS_{pr} = \sqrt{\frac{1}{N_d} \sum_i \left(p_i^{(mod)} - p_i^{(rec)} \right)^2}, \quad (6.7.13)$$

where $p_i^{(mod)}$ is the signal at the i-th detector calculated from the phantom model and $p_i^{(rec)}$ is the signal at the i-th detector based on the reconstructed emissivity. Emissivity profiles are normalised, i.e. RMS_{em} equal to one represents 100% of global reconstruction error while zero represents a perfect reconstruction.

In order to test the reconstruction quality as a function of plasma emissivity extent, several reconstructions of regular centred Gaussian model $\mathscr{G}$ with a scan of the standard deviation σ from 0.1 to 0.3 m were performed. Values of σ greater than 0.3 m are not considered as relevant with respect to the available plasma volume inside the vacuum vessel of Tore Supra tokamak. In this study, the grid size was arbitrary fixed to $N_p^2 = 40 \times 40$. Figure 6.12a and Figure 6.12b show the resulting RMS_{em} and RMS_{pr}, respectively. The usual range of experimental SXR emissivity extent observed at Tore Supra tokamak is also indicated in the figures. It can be noted that both MFI and Tikhonov regularisation methods give similar and satisfying results with $RMS_{pr} \approx 1\%$, with a slightly better quality for the MFI method in the range of plasma dimensions observed at Tore Supra tokamak. This trend seems to reverse for higher σ values, which can be explained by the different regularisation operators of the two methods. Indeed, the second order Tikhonov regularisation method simply minimises the curvature of the solution, while in the MFI method the ponderation matrix $\mathbf{F}$ flattens the gradient at the plasma edge. This can degrade the MFI reconstructions for high SXR emissivity extents with respect to the considered plasma volume, where the SXR emissivity level is still substantial at the very edge of plasma.
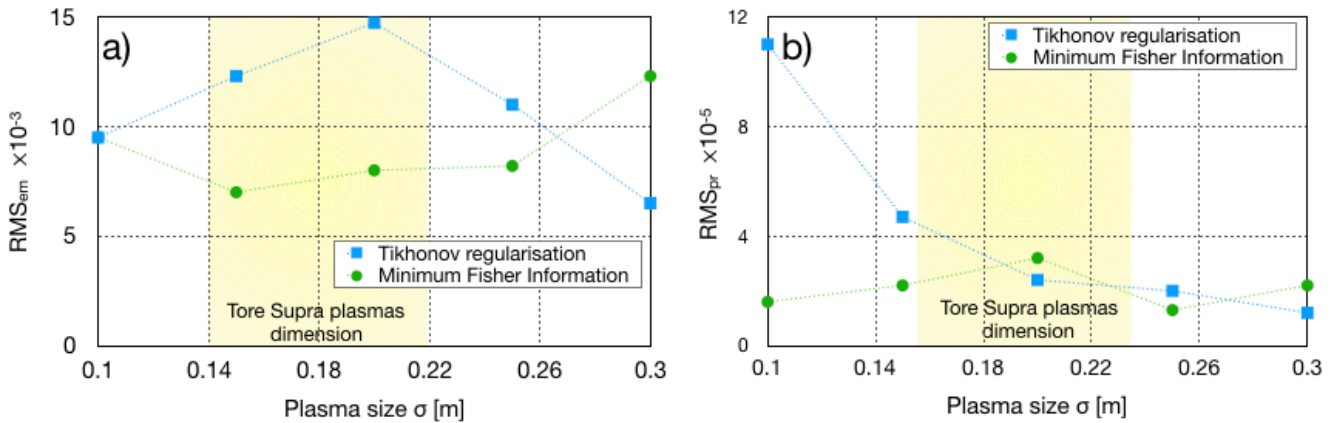
Figure 6.12 a) RMS$_{em}$ vs plasma dimension σ b) RMS$_{pr}$ vs plasma dimension σ for Tikhonov regularisation and Minimum Fisher Information methods.

In Figure 6.13 the two regularisation methods are compared in terms of RMS_{em} and RMS_{pr} versus the reconstruction grid size. The comparison involved a set of 108 phantoms per grid point, including the 3 plasma models for different plasma sizes (from σ = 0.15 m to 0.25 m) and for different positions (($\Delta x, \Delta y$) from -0.2 m to +0.2 m around the tokamak vessel centre), in order to cover all the possibilities inside the available plasma volume. As a general trend, it can be clearly seen that a finer grid leads to better reconstructions, but with an extra cost of the computational demands per inversion. Grids finer than $N_p^2 = 50 \times 50$ do not give better reconstructions than $RMS_{em} = 2 - 5\%$ while the computational time is an increasing exponential function of N_p^2 [Jardin 2016].

It was found that the second-order Tikhonov regularisation method is globally slightly more accurate in terms of RMS_{em} and MFI method tends to overfit measurements, due to the previously described rough methods of λ optimisation. For the Tikhonov regularisation-based method, implemented using GSVD approach, most of the computational time is spent in GSVD of the **W** and **L** matrices. In principle, if **L** does not depend on time (e.g. does not depend on magnetic configuration), the decomposition can be performed once for all required time intervals, before the inversion. However, in more complex cases as presented in Sec. 6.6, where matrix **L** is time dependent (e.g. depends on magnetic configuration), the GSVD has to be performed individually for every time interval of interest in the plasma discharge. This obviously increases the computational demands.
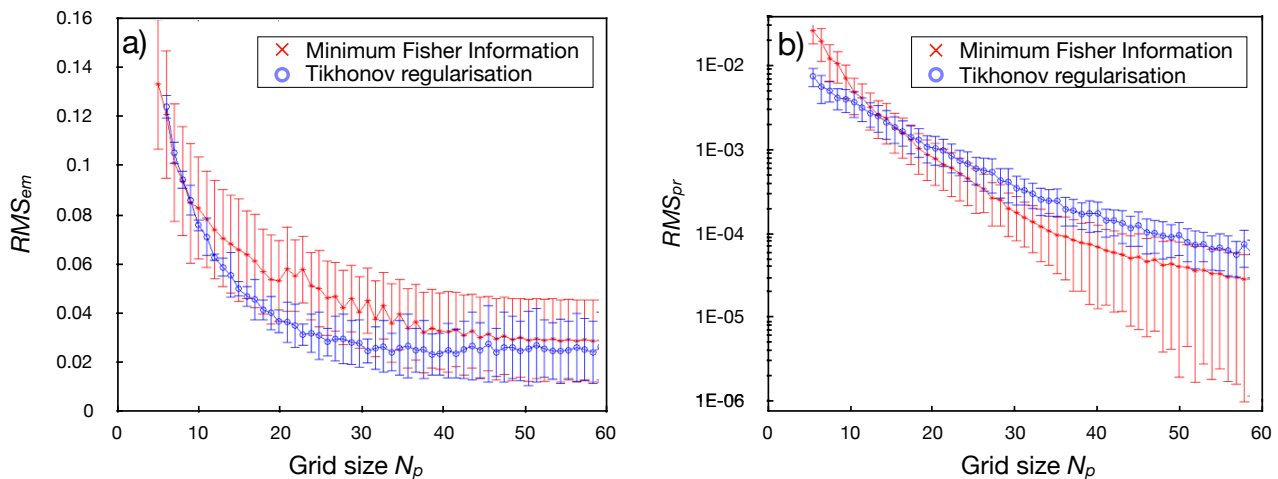
Figure 6.13 RMS_{em} and RMS_{pr} as a function of N_p^2 for the second order Tikhonov regularisation and MFI method [Jardin 2016].

It can be noticed from Figure 6.11b and Figure 6.11c that, due to relatively low number of projections, tomographic inversions do not give perfect reconstructions of complex shapes and poles of emissivity appear for non regular emissivity models. It is slightly more pronounced for MFI method. Thus, in order to give a physical example of the SXR emissivity reconstruction and to study the capability of the results interpretation, a Tore Supra discharge (#46564) was investigated. During the discharge, tungsten laser blow-off was performed. Figure 6.14a shows the time traces for all 82 SXR detectors. Since the increase in SXR emissivity during the laser blow-off is attributed to tungsten radiation, the background is subtracted from the SXR signal (see Fig. 6.14a). Then, based on the background-subtracted projections shown in Figure 6.14b, the SXR emissivity was reconstructed using MFI method. The resulting SXR emissivity features a High Field Side asymmetry, as shown in Figure 6.14c. In the next step, a synthetic model that mimics the experiment was created. The model is presented in Figure 6.14d, and the related

projections calculated based on the model are shown also in Figure 6.14b. The MFI was used to reconstruct the synthetic emissivity of the model. The result of the model reconstruction is shown in Figure 6.14e. The experimental reconstruction in 6.14c is thus compared with the reconstructed emissivity obtained from the phantom model (Figure 6.14e). The two tomograms show a similar pattern of poles of emissivity in terms of both position and intensity, validating the presence of an experimental High Field Side asymmetry in W radiation.
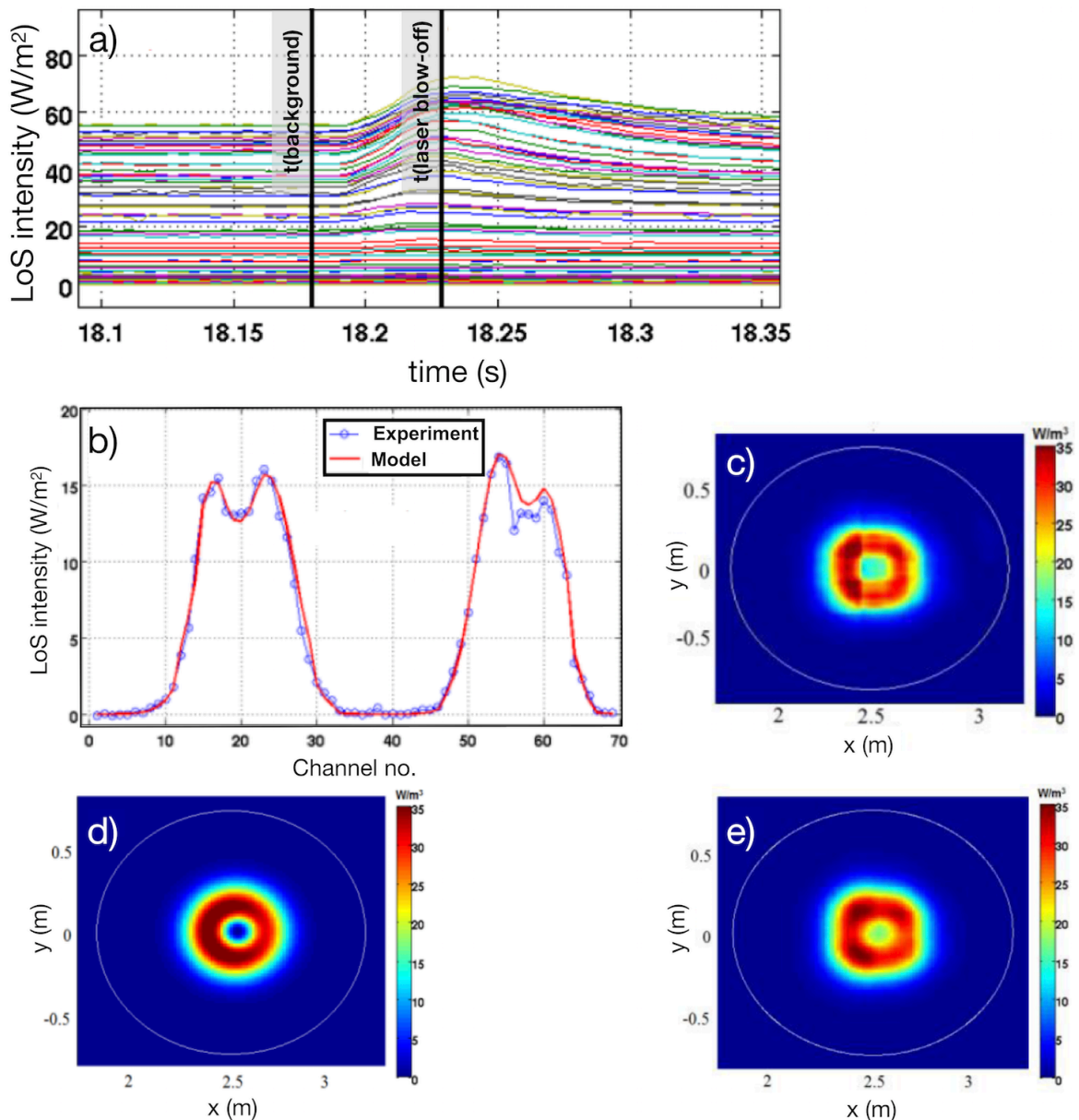

Figure 6.14 Reconstruction of a Tore Supra tokamak discharge with W laser blow-off (#46564). a) Time traces for all SXR detectors, b) input projections after background subtraction, c) experimental SXR emissivity reconstructed using MFI method, d) related synthetic model, e) reconstruction results of the model obtained with MFI method [Jardin 2016].

6.8 Using different basis functions

The methods presented in Section 6.6 and Section 6.7 belong to so-called series expansion methods. In this class of the reconstruction methods, the inversion problem is discretised by expanding the emission profile on a set of basis functions. Although the use of rectangular-pixel basis functions is a common approach, it is obviously not the only choice. In fact, rectangular-pixels belong to the so-called local basis functions. The name 'local' indicates that the basis function has value of 1 inside the corresponding pixel and 0 outside the pixel (i.e. basis functions have small or local spatial support). Pixels have usually rectangular shape, however hexagonal or other patterns are possible as well. The advantage of using the local basis functions is that they are not directly related to the expected shapes of the reconstructed emissivity function. On the other hand, usually many local basis functions are needed to properly reconstruct the emissivity function, thus, the problem is ill-conditioned and undetermined, as it was shown in the previous sections. An incorporation of *a priori* knowledge is needed in this case.
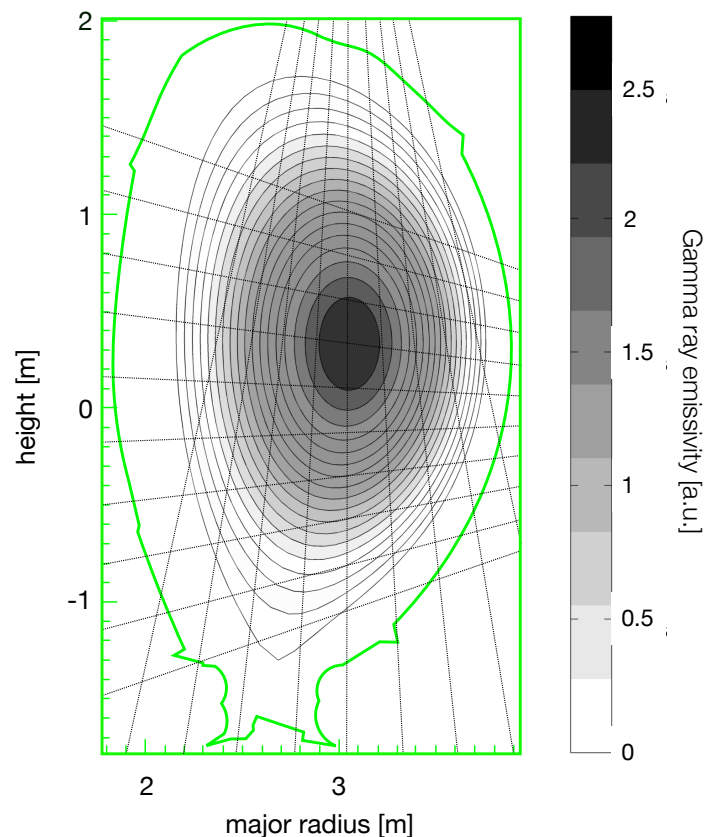

Figure 6.15 An example of gamma ray emissivity reconstruction using the magnetic flux surfaces as basis functions. JET discharge #90756.

On the contrary, global basis functions incorporate *a priori* information on the emissivity function somehow naturally. They are non-zero over a large part of the emissivity region (i.e. they have non-local spatial support) and describe some linear property of the emissivity function. Fourier series is an example of global basis function.

Figure 6.15 shows the results of gamma-ray emissivity reconstruction for JET discharge #90756. The developed and applied method relies, similarly to the method presented in Sec. 6.6, on Tikhonov regularisation. In this approach however the magnetic flux surfaces were used as basis functions. The smoothness of the reconstructed gamma-ray emissivity function was imposed by defining the regularisation operator **L** as:

$$
\mathbf{L} = \begin{bmatrix}
\frac{1}{\Delta\Psi_1} & 0 & \ldots & 0 & 0 \\
-\frac{1}{\Delta\Psi_2} & \frac{1}{\Delta\Psi_2} & \ldots & 0 & 0 \\
0 & -\frac{1}{\Delta\Psi_3} & \ldots & 0 & 0 \\
\ldots & \ldots & \ldots & \ldots & \ldots \\
0 & 0 & \ldots & -\frac{1}{\Delta\Psi_N} & \frac{1}{\Delta\Psi_N}
\end{bmatrix},
\tag{6.8.1}
$$

where $\Delta\Psi_1 \ldots \Delta\Psi_N$ denote separation between magnetic surfaces (1.. N). As the input data signals from the CsI detectors, installed in the JET camera (KN3 system), were taken. The reconstruction algorithm was implemented in MATLAB programming language.

6.9 Genetic Algorithms for plasma tomographic reconstruction

Based on J. Bielecki, Fus. Eng. Des. 127, 160 (2018).

In this Section, a new method of neutron emission reconstruction, based on genetic algorithms (GA), is presented. Genetic algorithms have been already applied in the field of electrical impedance [Olmi 2000, Hsiao 2001], optical [Kihm 1996] and X-ray [Yang 2014] tomography. However, this is the first attempt of application of GA for tomographic inversion in MCF devices. Genetic algorithms are adaptive heuristic search methods inspired by evolutionary ideas of natural selection and genetics. They use probabilistic selection rules, rather than deterministic ones. It is well known that parallelisation of the standard reconstruction method, e.g. based on the sparse GSVD, is not a trivial task. Contrary, GA are inherently parallel and can be easily distributed among many Central Processing Units (CPUs) or Graphic Processing Units (GPUs). Moreover, GA perform the search from a population of points, in a parallel manner. Therefore, they have the ability to avoid being trapped in a local optimal solution like traditional methods, which search from a single point. Genetic algorithms are also well suited for optimisation in noisy environments. All these points suggest that GA are worth testing for being a candidate as a tomographic inversion method in fusion devices. There exists a large number of textbooks and papers that tackle the problem of GA. The field of GA is very dynamic and continuously developing. Thus, the comprehensive overview of GA is definitely outside the scope of this monograph.
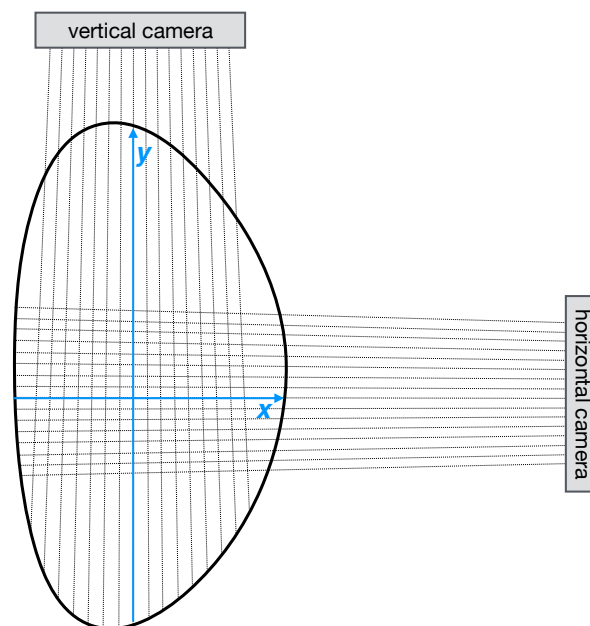

Figure 6.16 Geometrical layout of the LoS of the generic neutron tomographic system. The neutron imaging system consists of two cameras with 32 LoS in total.

In this section we test the feasibility of application of GA to the neutron emissivity tomographic inversion and investigate its robustness. To do that, a generic experimental setup presented in Figure 6.16 was used.

The system consists of two cameras, each camera features 16 neutron detectors. However, it is worth noting that the method can be easily adapted and applied to any tokamak's neutron diagnostic geometry.

In the presented approach, the ill-posed inversion problem is solved using a local basis functions in the form of rectangular pixels. Thus, the emissivity is discretised on a grid as a matrix $\mathbf{F}$ of $N \times N$ square elements. Each element is associated with a value of the emissivity that is assumed to be constant within the pixel. The grid size is a parameter that can be tuned and it should be chosen as a trade-of between the number of degrees of freedom of the ill-conditioned problem, the resolution of the reconstructed neutron emissivity, and the computing time. In the presented work, $N = 19$ was found as a good compromise between the resolution and computing time. Let us remind that the discrete inverse problem of tomographic reconstruction is defined by the following set of linear equations: (see Sec. 6.3, Eq. 6.3.1)

$$p_k = \sum_{i=1}^{N_p} w_{ki} f_i, \quad k = 1...N_d \qquad (6.9.1)$$

In the above equation f_i is the i-th element of the plasma neutron emissivity represented by $N^2 \times 1$ column vector $\mathbf{f}$, i.e. $\mathbf{f}$ is a row-major ordered vector form of emissivity matrix $\mathbf{F}$, N^2 is the total number of elements for the discrete representation of the neutron emissivity, N_d is the number of LoS (detectors) and p_k is the k-th element of $N_d \times 1$ column vector $\mathbf{p}$ that represents the available data along the LoS. The element w_{ki} of the geometrical matrix $\mathbf{W}$ represents the contribution of i-th element of emissivity to the k-th projection.

The proposed method is based on an iterative approach. The workflow of the reconstruction method is presented in Figure 6.17. The reconstruction starts with the initialisation phase. In this step, M random solutions $\mathbf{f}^j$, ($j = 1...M$) (so-called 'chromosomes' in GA terminology) are created. To speed-up the convergence process, an alternative version of initialisation step can be also used. In this case, the initial population of the solutions is taken as M solutions of ART (Kaczmarz) method (see Sec. 5.2) with the iteration number selected randomly, instead of the completely random initial solutions. It is a known fact that the ART itself does not provide, in general, physically meaningful results for the undetermined, ill-posed problem of tomographic reconstruction of fusion plasmas [Ingesson 1998]. As an illustration, Figure 6.18 presents results of the reconstruction by ART of three test phantoms (Gaussian, hollow, banana) defined in Sec. 6.7 after 100 iterations when the convergence of the solution was reached (i.e. further iterations do not improve the quality of the reconstruction). Although the overall
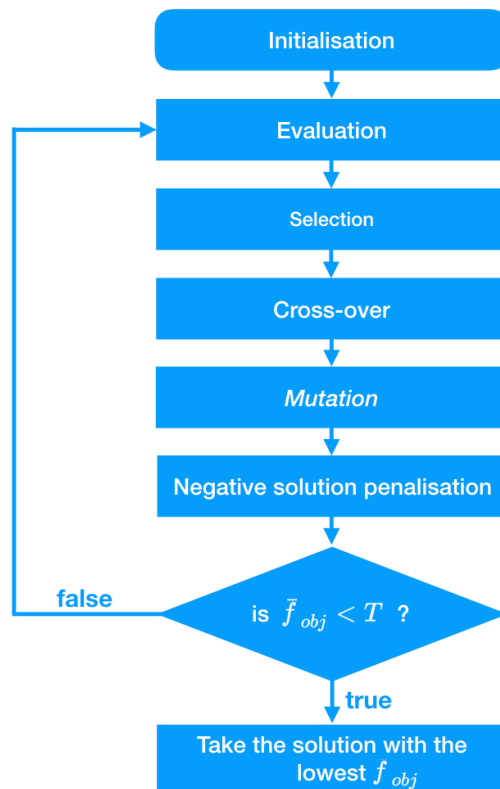
Figure 6.17 Workflow diagram of the reconstruction method based on Genetic Algorithms.
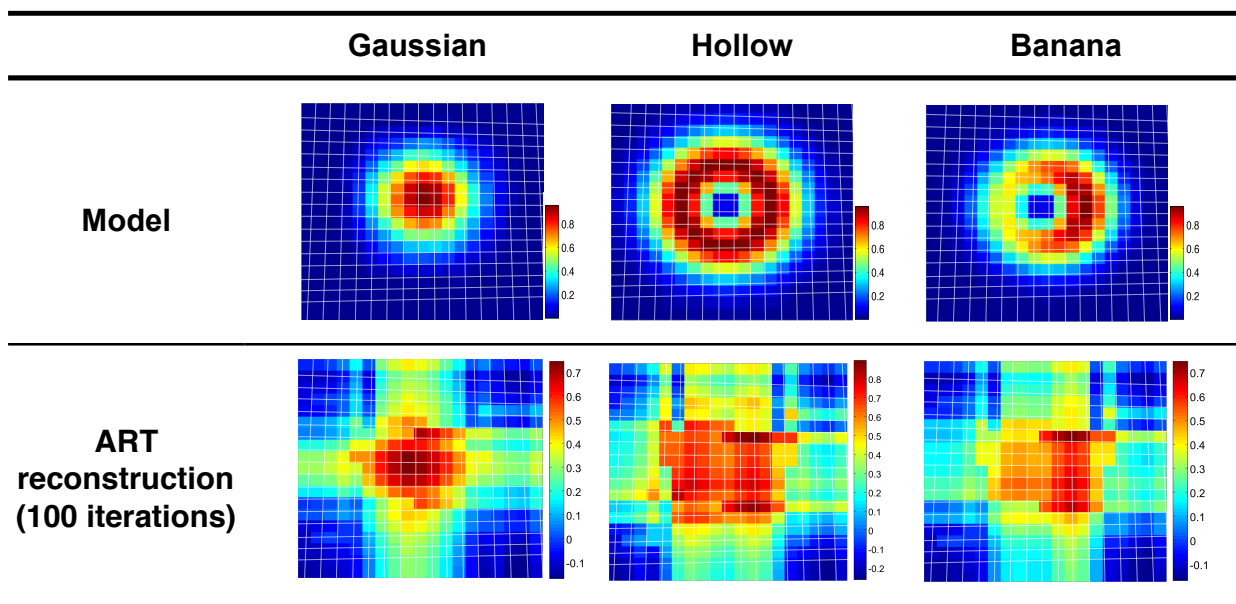

Figure 6.18 Results of the reconstruction of three neutron emissivity models using ART. The reconstructions were obtained after 100 iterations. Although ART is not able to reproduce good results for the highly ill-posed problem, the solutions obtained with different iteration numbers can be used as initial guesses for GA-based reconstruction method.

reconstruction quality is very poor and the results feature many artefacts, this kind of trial emissivity functions can be used as initial guesses for GA-based method.

In the next step, the solutions are evaluated based on the Tikhonov-like objective function:

$$\mathbf{f}^j_{obj} = \left\| \mathbf{W}\mathbf{f}^j - \mathbf{p} \right\|^2 + \lambda \left\| \mathbf{L}\mathbf{f}^j \right\|^2, \tag{6.9.2}$$

where $\mathbf{L}$ is a matrix representation of the derivative operator that imposes a smoothness constraint on the reconstructed solutions and λ is a constant that controls the weight given to the minimisation of this side constraint relative to the minimisation of the residual norm. Selection of the λ parameter could be optimised during the reconstruction using the methods described in Sec 6.5, however it would additionally increase the computational cost of the method. Thus, during the development phase, λ was set to 1. This choice was based on the experience from several initial tests. After the evaluation, in the selection step, a fraction S_r of the solutions with the lowest values of the objective function are selected as the candidates for the next generation. The quantity S_r represents the survival rate and it was set to 0.7. From these MS_r selected solutions, in the next step, the remaining $M - MS_r$ solutions are created in the cross-over phase. In every step of this phase, for two given solutions, three random numbers are selected that represent the start point C_s, the width C_w and the height C_h of a random block to be swapped between the solutions. This procedure is illustrated in Figure 6.19. Then, one of the two newly created solutions is randomly chosen as a candidate for a new generation. This cross-over procedure is repeated until $M - MS_r$ new solutions are created to keep the population number M constant at all the iterations.
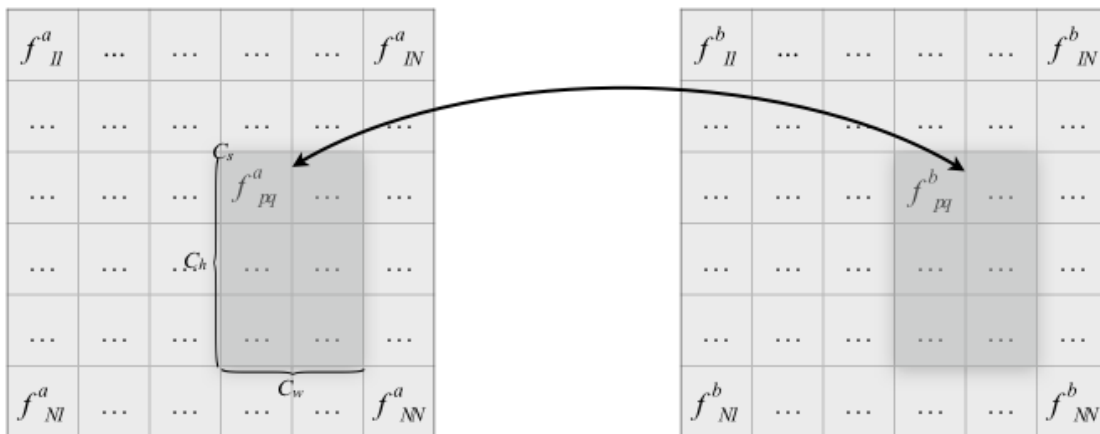

Figure 6.19 Illustration of the cross-over operation - swapping of two random blocks.

The next phase introduces some mutations in the pre-selected and crossed-over population. This is done in the following way. For randomly selected solutions of a given

generation, the elements of the selected solutions are modified by adding a random noise. The noise has a Gaussian distribution with the standard deviation equal to P_m fraction of the particular element value. The P_m parameter represents mutation probability and should be kept low (typically below 0.001 [McCall 2005]). Since the mutation operations can rarely introduce some minor negative elements in the solutions, in the last step, the negative solutions, if exist, are penalised by taking the absolute value. This step can be treated as an additional mutation and does not influence the convergence of the GA. The whole set of steps is repeated until the average objective function value $\bar{f}_{obj}$ is higher than a given threshold value T.

The developed method was tested using a synthetic data set defined in Sec. 6.7. Analytic neutron emissivity models of Gaussian, hollow and banana shapes were used to produce synthetic projections that were taken as inputs for the reconstruction algorithm. After performing the reconstruction, consistency between the model and the reconstruction result was evaluated for both local emissivity and the projections. Such tests are valuable for assessing the performance, accuracy and limits of the method. The reconstruction accuracy was evaluated using two figures of merit RMS_{em} and RMS_{pr}, as defined in Sec. 6.7, which represent root mean square error of the reconstructed emissivity and root mean square error of the projections, respectively.

Test reconstructions were performed for two different phantom sizes: small (S) $(\sigma = 0.15a, (\Delta x, \Delta y) = (0,0), \sigma_2 = \sigma, \sigma_1 = \sqrt{2}\sigma, \sigma_{as} = \sqrt{3}\sigma, (\Delta x_{as}, \Delta y_{as}) = (\sqrt{2},0))$ and large (L) $(\sigma = 0.21a, (\Delta x, \Delta y) = (0,0), \sigma_2 = \sigma, \sigma_1 = \sqrt{2}\sigma, \sigma_{as} = \sqrt{3}\sigma, (\Delta x_{as}, \Delta y_{as}) = (\sqrt{2},0))$, where a is the minor radius of the system. Figure 6.20 and Figure 6.21 show the results of reconstructions of the three phantom models for S and L phantoms size, respectively. The reconstructions were performed using the developed method based on GA and, for comparison, using Tikhonov regularisation (TR). In both methods, to allow for a fair comparison, no preferential smoothing constraint has been imposed. The solution of TR problem was obtained using GSVD as described in Sec. 6.6. In general, the reconstruction of the Gaussian emissivity model gives very satisfactory results, however reconstructions of more complex shapes like hollow model and banana model are not perfect due to the limited number of projections. The accuracy of GA is comparable with TR for both small and large phantoms. The only exception is the reconstruction of large Gaussian model, where RMS_{em} is slightly lower in case of TR method. The advantage of GA-based method can be noticed when the background emissivity around the reconstructed phantom is considered. The reconstructed shape is slightly smeared out in case of TR reconstruction. Also, the reconstructed maximum value of the model is better reproduced by GA-based method. The results are quantified by calculated RMS_{em} and RMS_{pr} that are presented in Tab. 6.1 for small phantoms size and in Tab. 6.2 for large phantoms size.
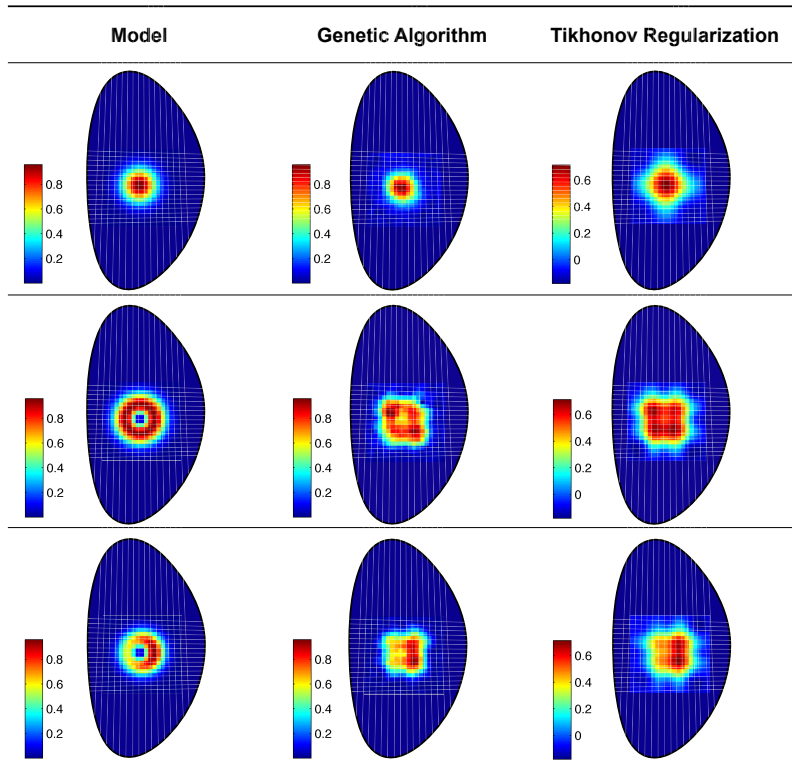
Figure 6.20 Three phantom models (small size) reconstructed using the developed method based on GA as compared with TR method.
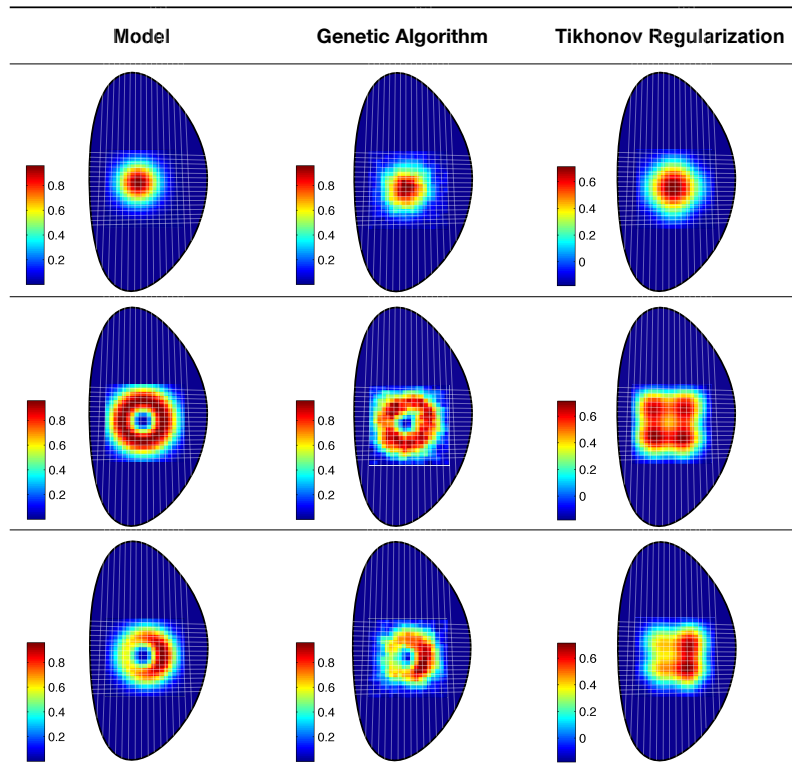
Figure 6.21 Three phantom models (large size) reconstructed using the developed method based on GA as compared with TR method.

Table 6.2 Calculated RMS_{em} and RMS_{pr} for the reconstruction of the three phantom models (small size) using GA and TR methods.

Model	GA		TR	
	RMS_{em}	RMS_{pr}	RMS_{em}	RMS_{pr}
Gaussian (S)	0.046±0.004	0.412±0.021	0.065	0.083
Hollow (S)	0.121±0.015	0.169±0.052	0.128	0.3128
Banana (S)	0.097±0.005	0.425±0.007	0.100	0.258

Table 6.3 Calculated RMS_{em} and RMS_{pr} for the reconstruction of the three phantom models (large size) using GA and TR methods.

Model	GA		TR	
	RMS_{em}	RMS_{pr}	RMS_{em}	RMS_{pr}
Gaussian (L)	0.034±0.005	0.072±0.036	0.028	0.062
Hollow (L)	0.084±0.010	0.065±0.032	0.162	0.247
Banana (L)	0.077±0.006	0.067±0.033	0.118	0.195

Figure 6.22 Small banana phantom model. An example of input projections (in blue) and back-calculated projections after the reconstruction using GA-based method (in red) and TR-based method (in black).

Since the GA-based method is not deterministic, the presented results are the average from 10 independent runs along with the stan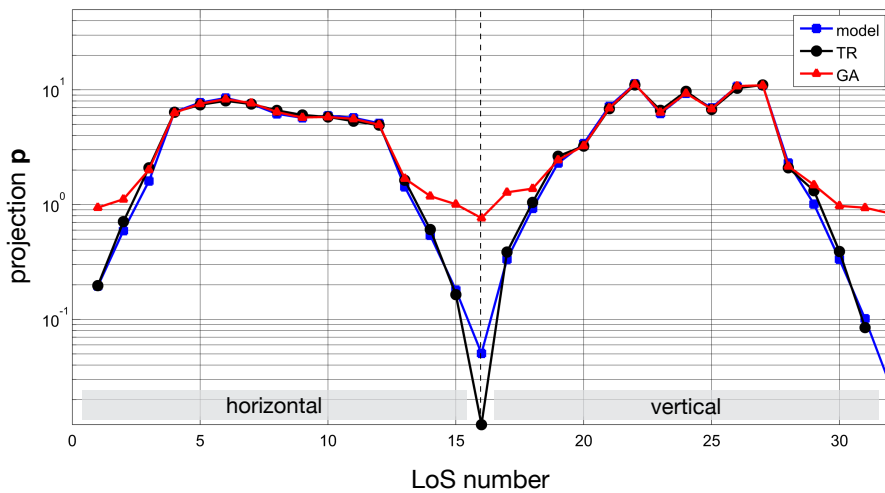dard deviations. On the other hand, due to stochastic nature of GA, the shapes reconstructed using the GA-based method are slightly jagged. The reconstructed emissivity functions are also not free from artefacts.

This can be noticed in the reconstruction results of small hollow and banana models where poles of emissivity appear as artefacts. Figure 6.22 presents the comparison of input projections for the small banana model and back-calculated projections for GA and TR methods. Slightly higher discrepancies of the original and back-calculated projections are observed for GA-based method. This is quantified by RMS_{pr} values presented in Tab. 6.2. The RMS_{pr} value for the banana model is around ~1.5 times higher for GA method than for the result obtained with TR method. Nevertheless, the obtained RMS_{pr} errors are very low for both methods (< 5%).
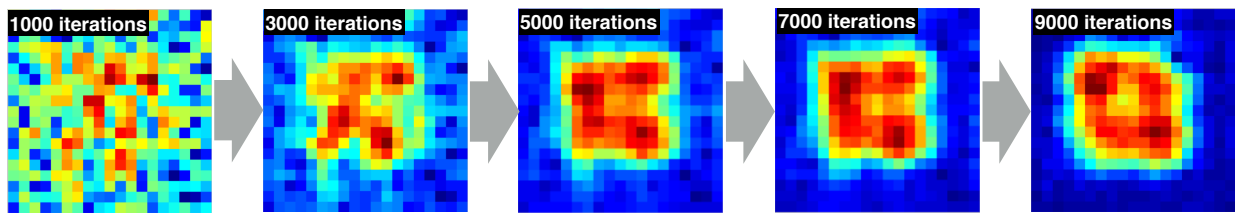
Figure 6.23 Evolution of the GA-based solution for the reconstruction of the small hollow phantom model.

Figure 6.24 The average value of the objective function as a function of the iteration number for the reconstruction of the small hollow model.

Figure 6.23 presents the evolution of the GA solution for the reconstruction of the small hollow phantom model. The plots were created every 2000 iterations, up to ~10000 iterations where the convergence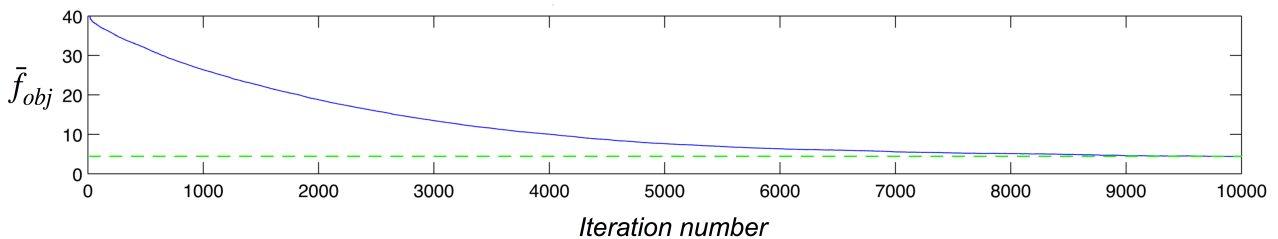 condition was reached. Figure 6.24 shows the average value of the objective function $\bar{f}_{obj}$ as a function of the iteration number for the same reconstruction of the hollow model.

During a tokamak operation, diagnostics and associated Data Acquisition Systems (DAQ) usually work in noisy environment of high-power NBI and ICRH systems. Thus, in the next step, the resilience of the developed method against the noise was studied. For this purpose, the banana phantom model was used. The line-integrated projection data set **p** was constructed for the phantom and next the random noise was intentionally added to the projection data. It was assumed that each detector acquired a signal with an addition of relative noise. In principle, the neutron detector signals exhibit noise resulting from statistical fluctuations of the finite number of neutrons detected, as described by a Poisson distribution. In practice however, the noise can be modelled using a Gaussian distribution, since for small neutron counting rates the noise is generally dominated by other signal-independent sources (e.g. electronics-noise) and for larger counting rates the central limit theorem ensures that the Poisson distribution approaches the Gaussian distribution. The simulated noise had therefore the Gaussian distribution with standard deviation equal to fraction l of the signal p_k in a particular channel. The noise level was varied from 0.01 to 0.1. For each noise level, the reconstruction quality in terms of RMS_{em} was tested by performing 10 reconstructions of the phantom using synthetic projections affected by the noise. Figure 6.25 presents the plot of RMS_{em} as a function of the noise level l. As a reference, the results from TR method were also included in the figure.
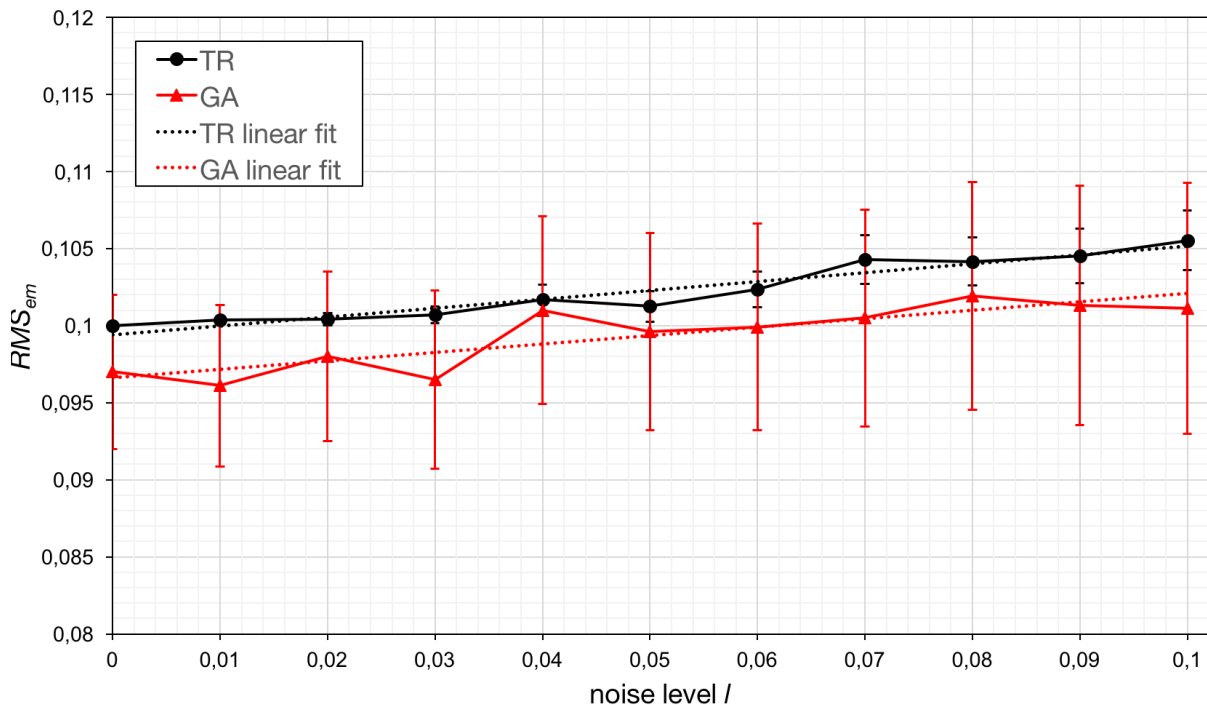

Figure 6.25 RMS$_{em}$ as a function of the noise level l for the GA-based method (in red) and TR method (in black). Results for the small banana phantom model.

For $l > 0.07$ significant distortions of the emissivity shape were observed. Additionally, since the GA-based method is of a stochastic nature, the significant deviations from the mean RMS_{em} values were observed.

The computation time needed for reconstructions highly depends on the implementation (parallel, sequential computing) as well as on the numerical libraries and machine type (e.g. CPU, GPU, Field Programmable Gate Arrays (FPGA)). Moreover, the time depends also on selection of parameters such as population size, initial guess, reconstruction grid size etc. Finally, the method is of a stochastic nature itself, thus slightly different computation time can be required for different runs of the same code, even if the same input data and parameters were used. However, in order to give a rough estimate on the computational demands, the reconstruction time for the GA-based method (sequential computation implemented into a MATLAB code) is plotted in Figure 6.26 as a function of the grid size N. The test was carried out for the three phantoms (large size) with the optimal parameters used in the previous part of the study. All reconstructions were conducted using 10000 iterations. The presented results are the average from 10 independent runs (error bars are of the size of the symbols). In the investigated range of the grid size parameter N, the presented implementation of the algorithm is of polynomial time complexity $\mathcal{O}(n^2)$ regardless the considered model (Gauss, Hollow, Banana).
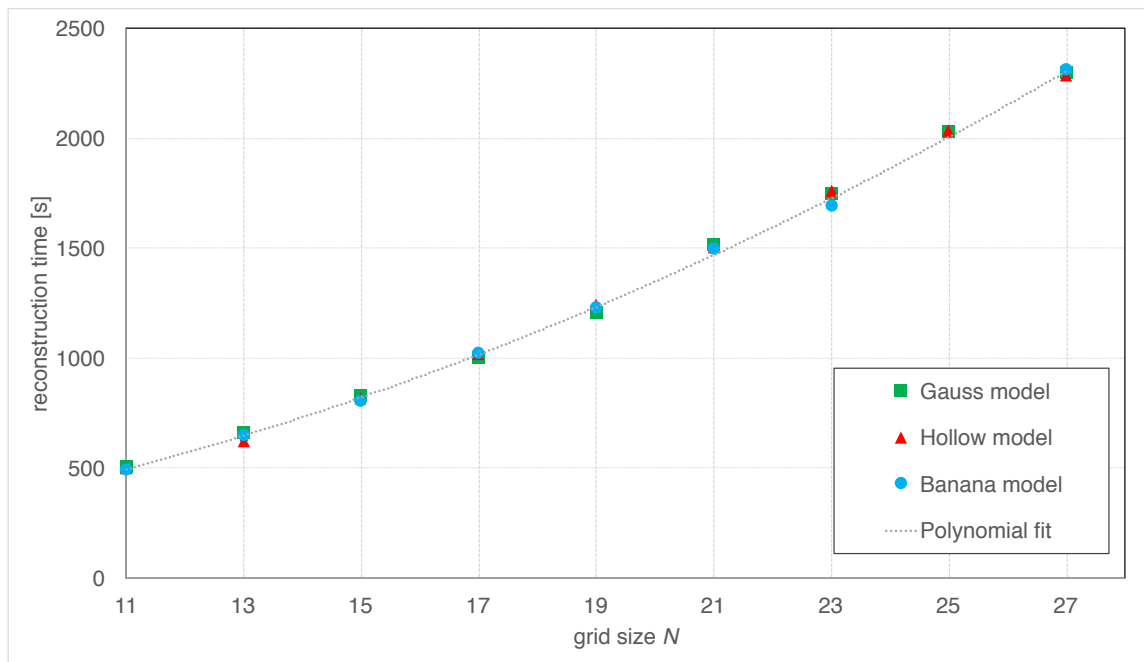

Figure 6.26 Reconstruction time for the GA-based method as a function of the grid size

The presented novel method of neutron emissivity reconstruction for tokamak plasma has been developed and tested with the set of synthetic models and it has been proven that

the method provides accurate reconstruction results, comparable with results obtained with TR method. It was therefore shown that GA can be successfully applied for neutron emissivity reconstruction from limited experimental data set of a tokamak diagnostic. The root mean square difference between the reconstructed solution and the model RMS_{em} varied between 5 – 12 % for the GA-based method and 3 - 16% for TR method. It must be stressed however that the tests were carried out in somewhat ideal situation, since the comparison was performed using perfect models without presence of noise and using an ideal description of the geometrical layout of LoS. The errors assessment in the real situation is much more difficult, however those results give at least the lower limit of the expected reconstruction errors. The method also performs well when the additive noise present in the input projections is below ~7 %. Typically, around 10000 iterations are needed to achieve solution convergence. The method is computationally demanding and, at this stage, is slower than TR method with GSVD [Bielecki 2015]. However, a new highly-parallel implementation of the method utilising GPU-accelerated computation is foreseen. In the presented method, many parameters can be tuned (e.g. population size M, survival rate S_r, cross-over parameters C_s, C_w, C_h), however the experience shows that the settings can influence the convergence speed but very rarely influence the overall accuracy of the method.

6.10 Monte Carlo approach for plasma tomographic reconstruction

Based on J. Bielecki, submitted to Journal of Fusion Energy (2018).

In this section a new approach to plasma neutron emissivity reconstruction based on Metropolis–Hastings [Metropolis 1953, Hasting 1970] MC algorithm is presented. The presented method can serve as an alternative for commonly applied techniques described in Sec 6.6 and Sec 6.7. The algorithm is based on a biased random walk. A dedicated computer code generates pseudo-random samples within the domain that contains the solution. The proper selection criterion (i.e. objective function) ensures the convergence to the desired solution.

Large non-trivial systems, such as systems involved in the ill-posed problems of plasma tomographic reconstruction, suffer from the 'curse of dimensionality'. This means that the number of possible configurations is very large with numerous local minima, and therefore a straightforward sampling of these configurations is rather impractical, as it was shown before. For neutron tomographic reconstruction from limited data sets measured in tokamak devices, the applied Metropolis–Hastings algorithm can overcome this problem, avoiding trapping in local minima. In fact, the algorithm offers a possible method for jumping out of a local minimum by accepting, with some finite probability, changes in
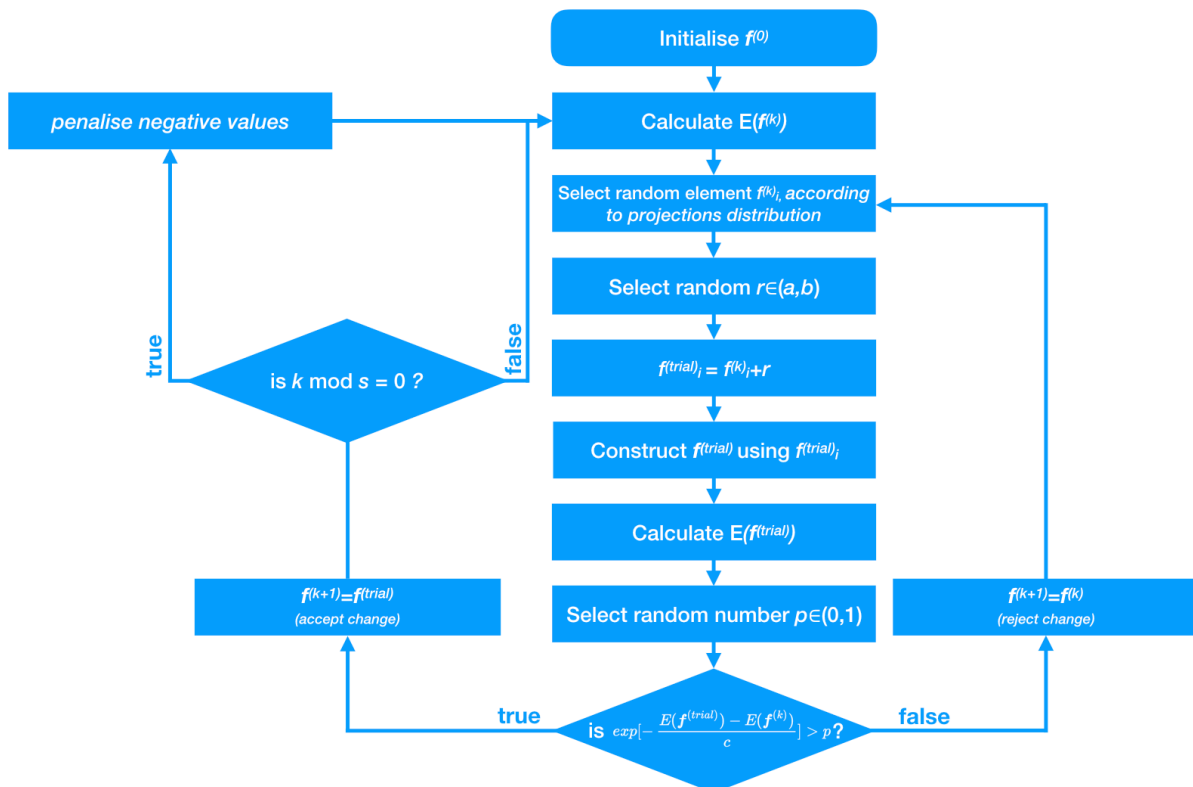

Figure 6.27 Workflow diagram of the MC-based reconstruction method.

the direction opposite to indicated by the objective function. Moreover, in this approach, additional *a priori* information (e.g. about the smoothness of the solution) can be also easily incorporated. This *a priori* information is taken into account by the (Tikhonov-like) objective function.

The method has been developed and evaluated using the generic tomographic system described in the previous section (Fig. 6.16). Again, we focus on solving Eq. 6.9.1. In most cases of plasma tomography, solving of the equation by the direct matrix inversion is impossible due to ill-posed nature of the problem and some kind of regularisation is usually applied, as demonstrated in previous sections. In the current approach we take advantage of stochastic MC approach, instead of solving the problem by Tikhonov regularisation with Singular Value Decomposition (SVD), as it was shown in Sec. 6.6. The proposed method is based on an iterative approach. The workflow of the reconstruction method is presented in Figure 6.27. The reconstruction starts with the initialisation phase. In this step, an initial guess of the solution $\mathbf{f}^{(0)}$ is created. In the developed code, a $N^2 \times 1$ null vector is taken as the initial guess, where, as previously, N^2 is the total number of elements for the discrete representation of the neutron emissivity. In the subsequent step, an element f_i of the solution is selected randomly in order to be modified. The probability distribution for selecting the random element is defined according to projections $\mathbf{p}$. This process is pictorially represented
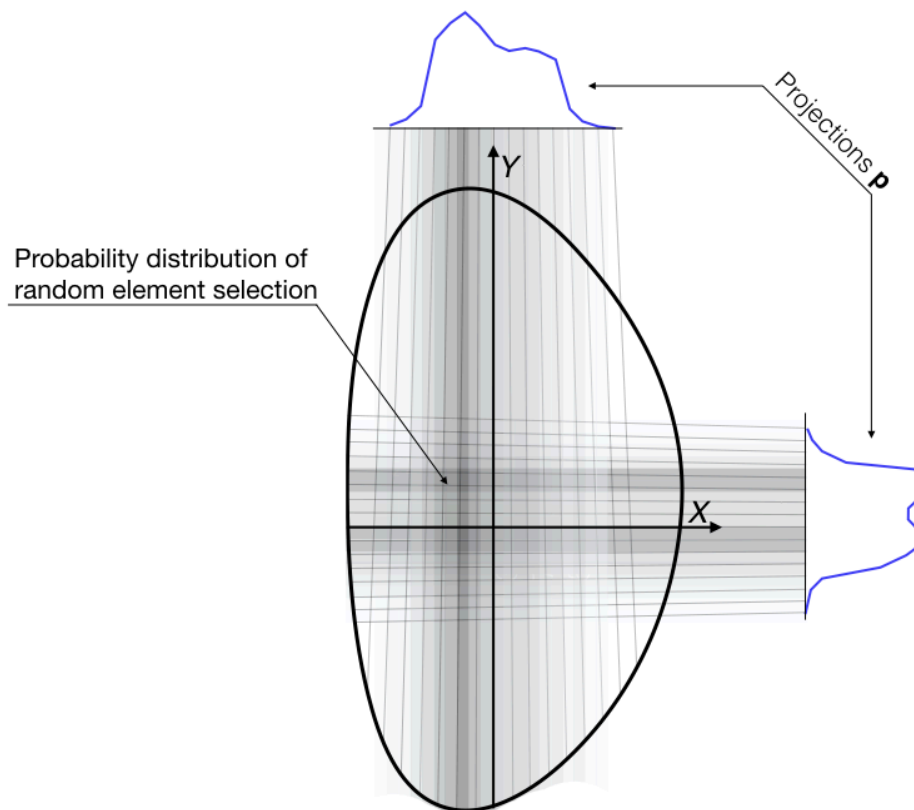

*Figure 6.28 Illustration of the selection of a random element according to projections **p**.*

in Figure 6.28. Such an approach ensures that the modifications are more frequently introduced in the regions where greater values of the reconstructed function are expected and less frequent modifications are performed in the region where lower values are expected. In this sense, the method inherits some aspects of the BP method (cf. Sec 4.8). The value of the selected element is then modified by adding a random number r, drawn from a uniform distribution in the interval (a, b). The lower a and upper b limits of the interval are determined experimentally and in this work were set as -0.001 and 0.001, respectively. In general, the smaller are the steps of modifications the better reconstruction accuracy can be achieved, however, more iterations are needed to obtain the convergence. In each iteration, the unmodified solution $\mathbf{f}^{(k)}$ and the modified solution $\mathbf{f}^{(trial)}$ are evaluated by the Tikhonov-like objective function given as:

$$E(\mathbf{f}^{(k)}) = \left\| \mathbf{W}\mathbf{f}^{(k)} - \mathbf{p} \right\|^2 + \lambda \left\| \mathbf{L}\mathbf{f}^{(k)} \right\|^2. \qquad (6.10.1)$$

In Eq. 6.10.1, $\mathbf{L}$ is a matrix representation of the second-order derivative operator that imposes a smoothness constraint on the reconstructed solutions, λ is the regularisation parameter and the superscript (k) denotes the iteration number.
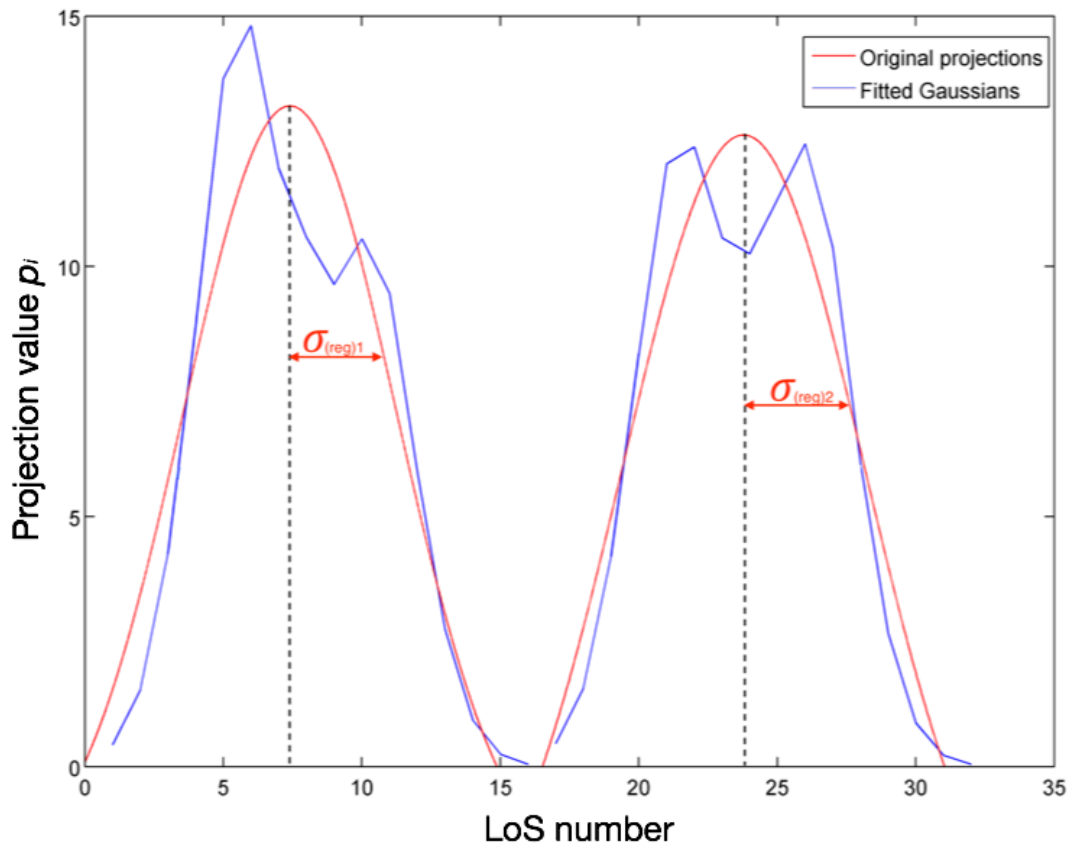

Figure 6.29 Illustration of the regularisation parameter selection procedure based on the widths of Gaussian functions fitted to the projections.

In the presented approach, a simple heuristic method of finding approximated optimum of λ is applied. At first, two Gaussian functions are fitted to the projection data set (one for the vertical view, another for the horizontal view) as shown in Figure 6.29. The regularisation parameter λ is then taken as a function of the variations $\sigma^2_{(reg)1}$ and $\sigma^2_{(reg)2}$ of the two Gaussian distributions:

$$\lambda = \frac{\sigma^2_{(reg)1} + \sigma^2_{(reg)2}}{l_{MC}}, \tag{6.10.2}$$

where l_{MC} is a constant that has been determined experimentally, based on scans for several test phantoms (in this study l_{MC} =1.4). Dynamic selection of λ, based on the widths of the projection functions, ensures increased smoothness for a wider emissivity function and prevents from over-smoothing when the emissivity function is more peaked.

Let $E(\mathbf{f}^{(k)})$ denote the value of the objective function before introducing the modification and $E(\mathbf{f}^{(trial)})$ be the value of the objective function when the modification of selected element f_i is considered (i.e. $f_i^{(trial)} = f_i^{(k)} + r$). Then, the modification is accepted only if:

$$exp\left(-\frac{E(\mathbf{f}^{(trial)}) - E(\mathbf{f}^{(k)})}{c_{MC}}\right) > p_{MC}, \tag{6.10.3}$$

where p_{MC} is a uniformly distributed random number in the interval (0,1) and c_{MC} is a small constant parameter (c_{MC} = 0.001 taken in this study). If condition 6.10.3 is fulfilled, the modified solution $\mathbf{f}^{(trial)}$ is taken for the next iteration (i.e. $\mathbf{f}^{(k+1)} = \mathbf{f}^{(trial)}$), otherwise unmodified solution is used in the next iteration (i.e. $\mathbf{f}^{(k+1)} = \mathbf{f}^{(k)}$). In order to prevent unphysical solutions containing negative elements, every s iterations (s = 100, in this study) the negative values of $\mathbf{f}^{(k)}$, if exist, are penalised by taking the absolute value of the solution. The iteration procedure continues until the objective function $E(\mathbf{f}^{(k)})$ is higher than a given threshold value T.

Figure 6.30a shows the objective function value as a function of the iteration number. After $\sim 8 \times 10^4$ iterations the convergence criterion ($E(\mathbf{f}^{(k)}) < T$) was met. In general, the objective function decreases with the iteration number, however, locally, the objective function can increase as it is shown in Fig 6.30b. Figure 6.30c shows the change in the objective function value $\Delta E = E(f^{(trial)}) - E(f^{(k)})$ as a function of the iteration number. Figure 6.30d presents the rejected trials (i.e. those trials for which condition 6.10.3 has not been fulfilled) as a function of the iteration number. It can be clearly seen, that number of the rejected events increases when the iterative process converges to the desired solution. This is quite obvious, since when the current solution becomes more similar to the final solution, there is much less possibilities to implement random changes that would decrease the objective function.
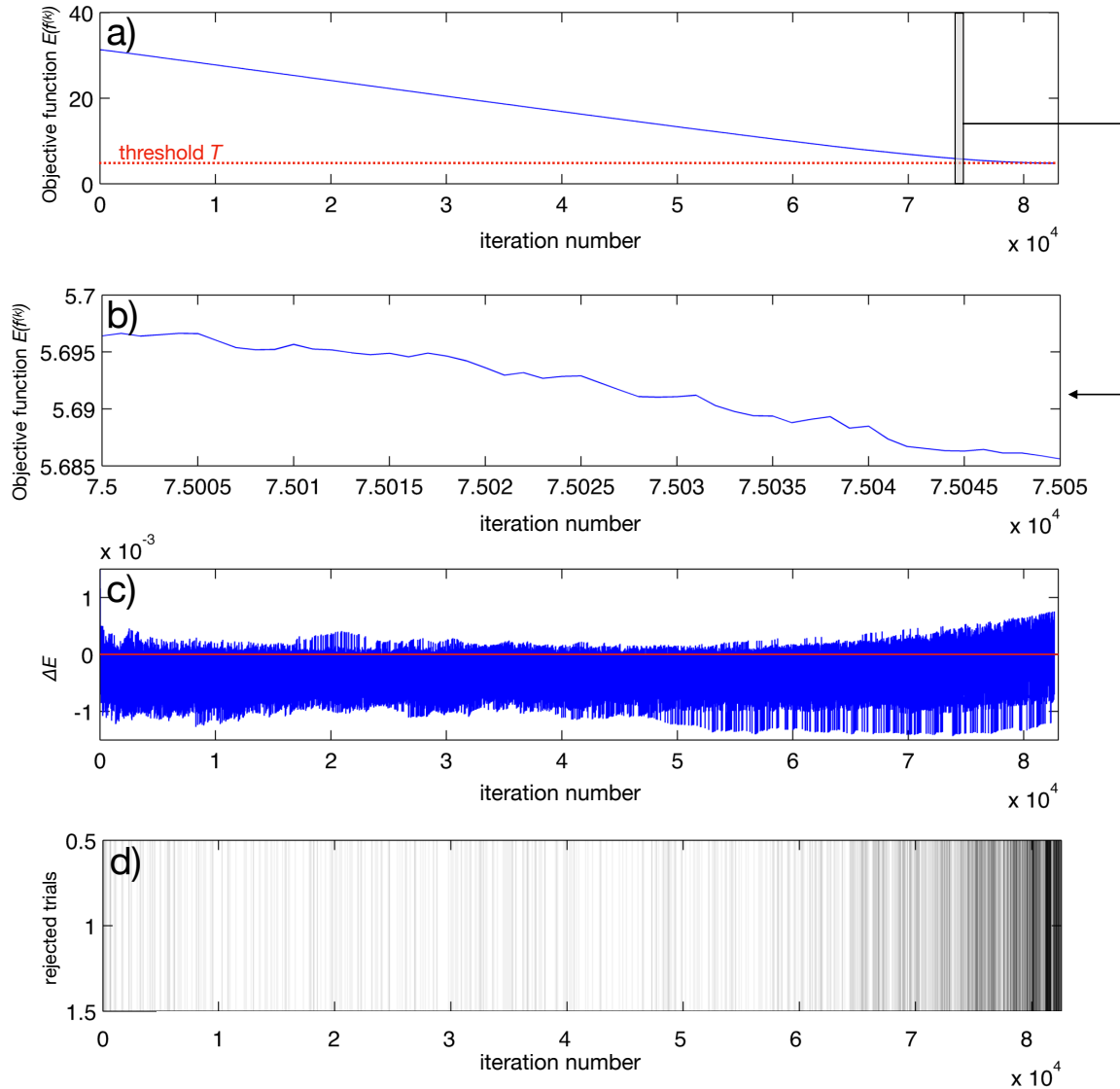
Figure 6.30. Convergence of the solution in Monte Carlo-based reconstruction method: a) the objective function value as a function of the iteration number, b) zoom of plot a) to show that the objective function value can locally increase, c) the change in the objective function value ΔE as a function of the iteration number, d) rejected trials (black vertical lines) as a function of the iteration number.

The presented method was tested with the set of plasma neutron emissivity phantom models defined in the previous section. Figures 6.31 and 6.32 show the reconstruction results of the modelled neutron emissivity, along with the relative errors, for small and large phantoms size, respectively. Figures 6.33a-f summarise the reconstruction quality, in terms of RMS_{em}, as a function of the reconstruction grid size, for all the considered models. Since the presented method is of a stochastic nature, the presented results are the average values from 10 independent reconstructions and the error bars represent the standard

120

Figure 6.31 Three phantom models (small size) reconstructed using the developed MC method and the relative error in reconstruction.

Figure 6.32 Three phantom models (large size) reconstructed using the developed MC method and the relative error in reconstruction.

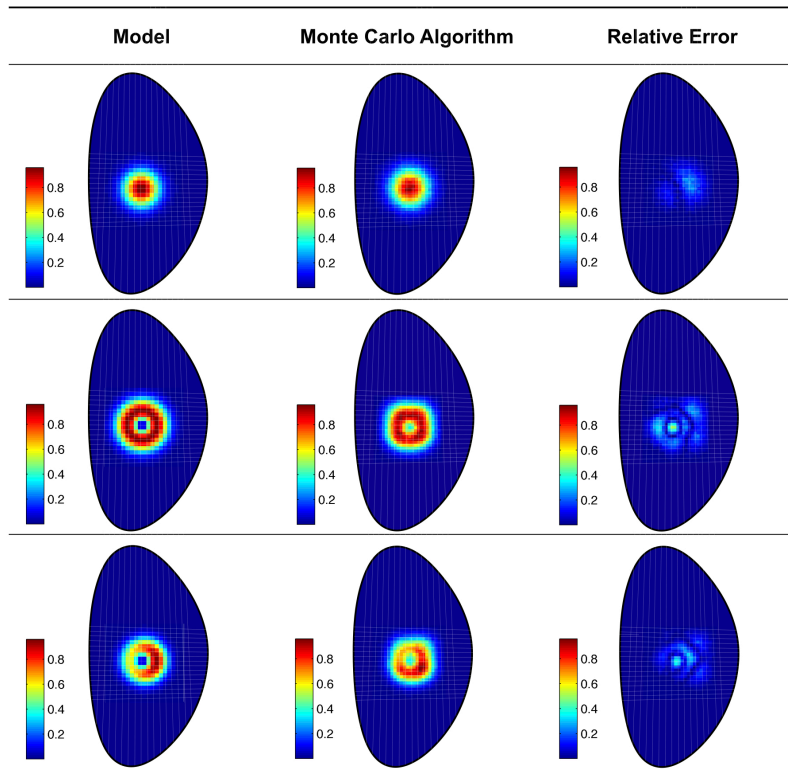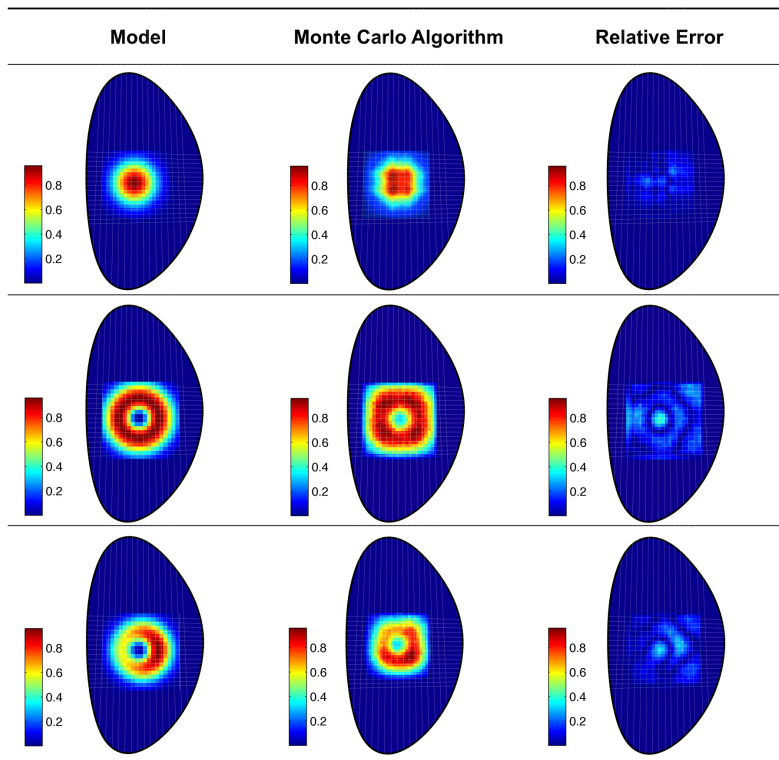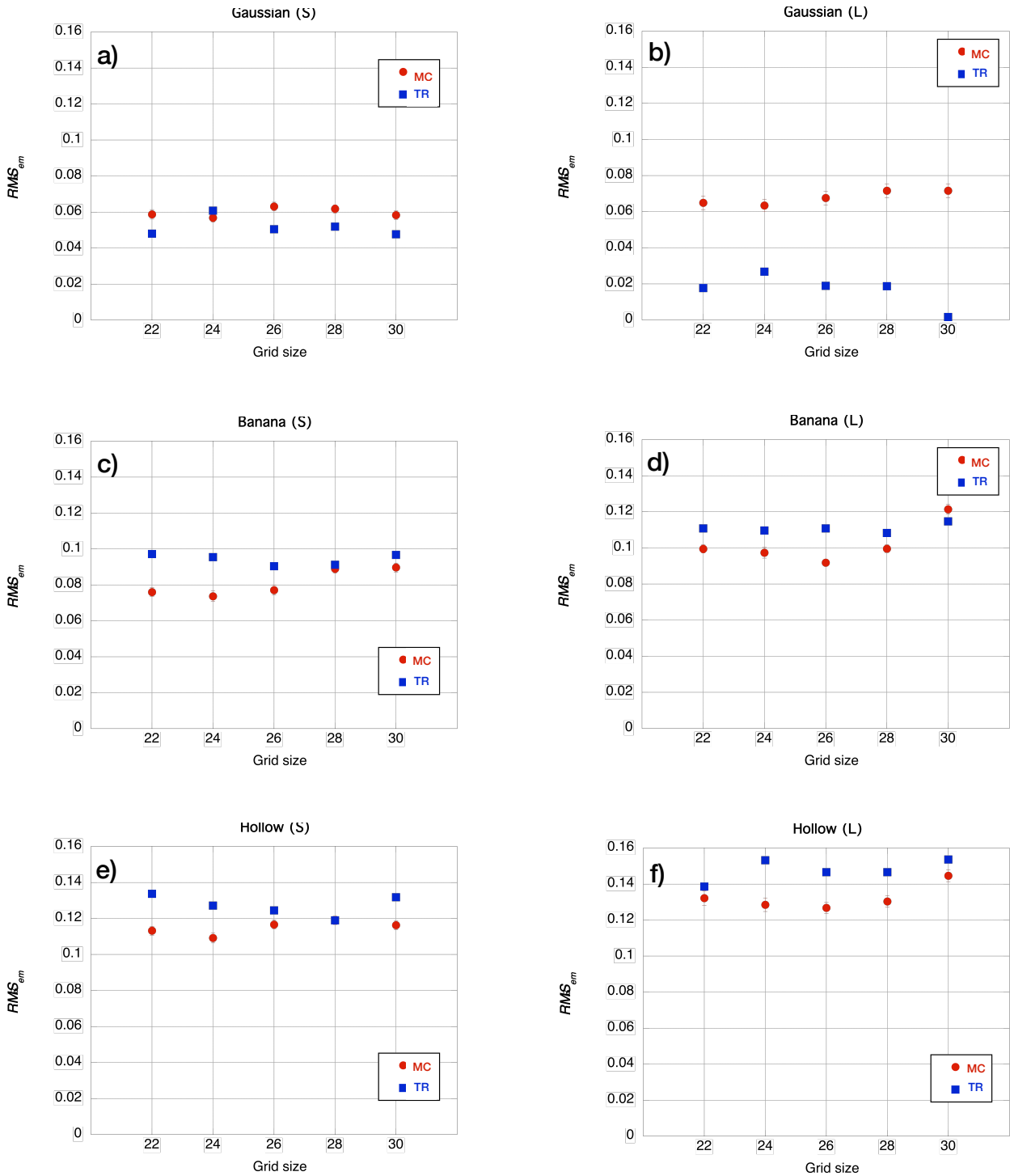Figure 6.33 The RMS_{em} as a function of the grid size for the developed MC method (in red) and TR (in blue). a) small Gaussian model, b) large Gaussian model, c) small banana model, d) large banana model, e) small hollow model, f) large hollow model.

deviation. For comparison, also the RMS_{em} values for the results obtained with TR method have been included in the figure. It can be noted that, in most cases, grid size of 24 or 26 is optimal and further increase of the grid resolution does not lead to better quality (i.e. lower RMS_{em}) of the obtained results. In general, the developed MC method provides better results of reconstruction than TR for more complex models (banana and hollow). However, RMS_{em} is higher for MC method (~0.06) than for TR method (~0.02) when large Gaussian model is considered. Both methods give almost equal RMS_{em} values for small Gaussian model. In general, TR method seems to better reconstruct larger phantoms while in case of the MC method slightly lower RMS_{em} is obtained for the small phantoms set. For both large and small hollow and banana models, regions with the highest relative reconstruction error are located in the central part of the model. In these regions, the modelled emissivity drops to zero, however due to the smoothness constraint implemented in the objective function the reconstructed emissivity has small non-zero value. This leads to the situation that the relative error locally reaches ~0.35, in the central part of the reconstructed emissivity (see Fig. 6.31 and Fig. 6.32).

The developed method has been also tested against random noise present in the input projections. Similarly as for the GA-based method described in the previous section, the simulated noise had the Gaussian distribution with standard deviation equal to fraction l of the signal p_k in a particular projection channel. The noise level was varied from 0.01
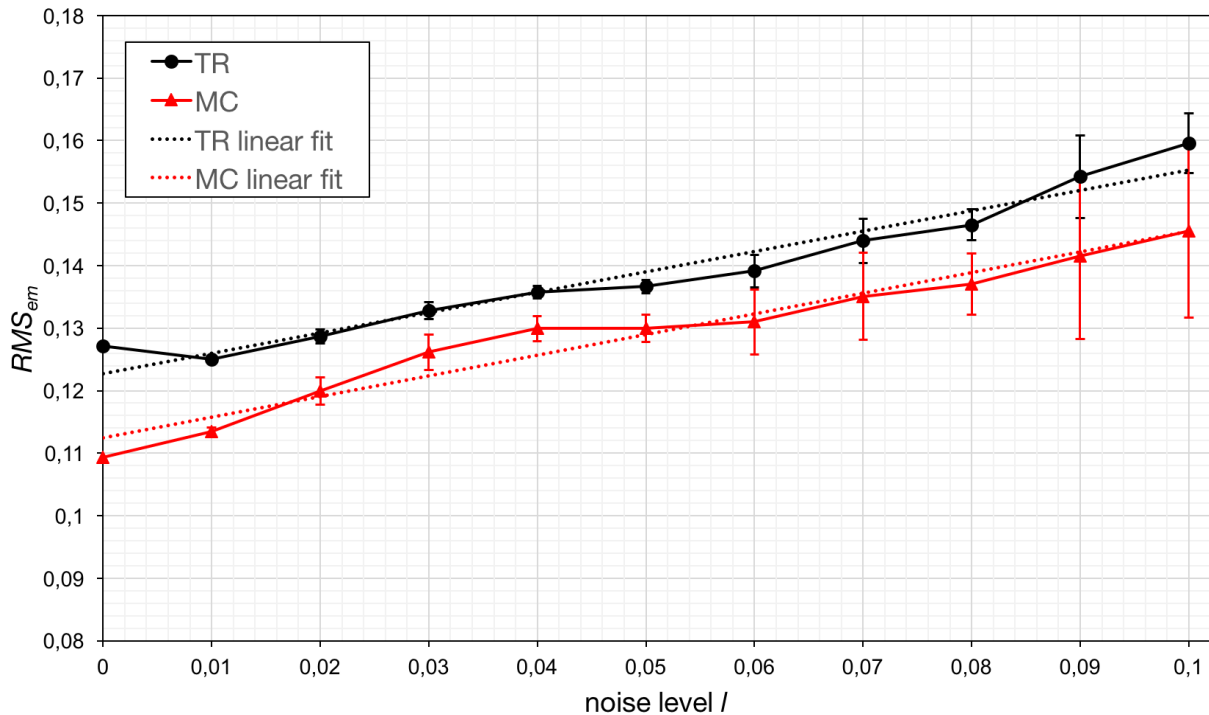
Figure 6.34 The RMS$_{em}$ as a function of the noise level l for the MC-based method (in red) and TR method (in black). Results for the small hollow phantom model. Reconstruction grid was set to 24.

to 0.1. For each noise level, the reconstruction quality, in terms of RMS_{em}, was tested by performing 10 reconstructions of the small hollow phantom (grid size = 24) using synthetic projections affected by the noise. The results of this test are shown in Figure 6.34, where RMS_{em} is plotted as a function of the noise level l. As a reference, the results from TR method are also included in the figure. Similarly to the GA-based method, the developed MC method features almost linear increase of RMS_{em} with noise level l. However, in case of the MC method, the slope is much greater (~ 0.3) when compared to the GA-based method (~0.05), which means that the method is much more sensitive to noise present in the input data.

As it was stated in the previous section, the computational time depends on many factors. However, again in order to give at least a rough estimation of the reconstruction speed of the method, the number of iterations required to archived the convergence and the time spent on the computations is presented in Figure 6.35 for the three phantom models (large size).
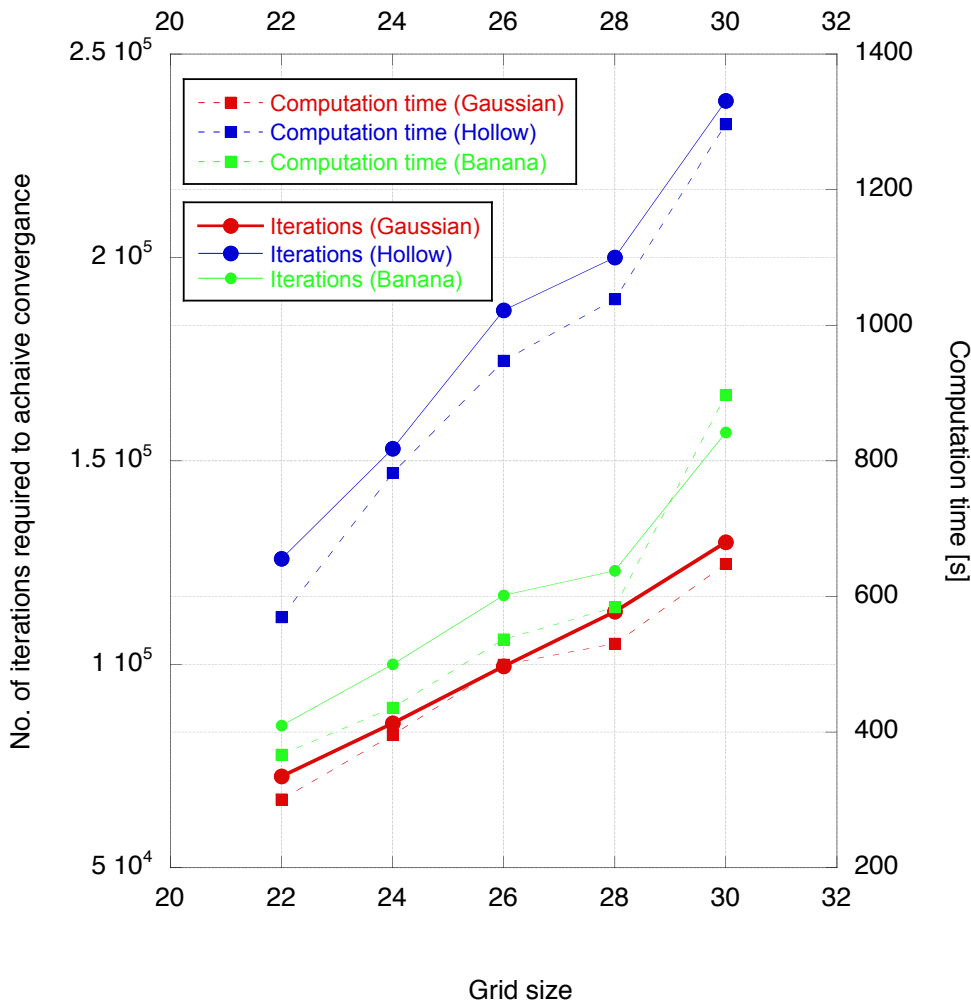
Figure 6.35 Computational time and number of iterations required to achieve convergence for reconstruction of the three phantom models using the MC-based method.

The presented results are the average values obtained from 10 independent runs (error bars are of the size of the symbols). In the investigated range of the grid size parameter, both computational time and number of required iterations feature approximately linear dependence. Reconstruction of the hollow model is the most computationally demanding. Less computation time is needed to reconstruct banana model, while the simple Gaussian model requires the lowest number of iterations to obtain the convergence and hence it consumes the lowest computational time.

Another MC method for neutron and gamma emissivity reconstruction has been developed by Craciunescu et al. [Craciunescu 2009]. The authors called this method *Monte Carlo Back-projection Technique*. It is based on a simple iterative scheme and, for complex shapes of numerically simulated emissivity distributions, provides usually poorer results than TR or Minimum Likelihood method [Craciunescu 2009].

6.11 Gamma-ray emissivity tomographic reconstructions for Three-Ion Scenario Experiments at JET

Based on Ye. Kazakov, (...), J. Bielecki, et.al., Nature Physics 13, 973 (2017).

This section shows an application of the gamma-ray tomographic reconstruction in recent and pioneering research with efficient acceleration of ^{3}He ions to high energies in dedicated hydrogen–deuterium mixtures (so-called 'three-ion scenario') at JET tokamak. The goal of the study was to validate that, in properly chosen multi-ion plasmas, electromagnetic ion cyclotron waves can be effectively absorbed by a very low number of resonant ions. This technique opens the possibility of highly-efficient generation of energetic ions in magnetised plasma, allowing for effective plasma heating. It turns out that the tomographic reconstruction methods can be of great help also in this study.

The charged plasma particles gyrate around the magnetic field lines with their characteristic cyclotron frequency $\omega_{ci} = q_s B/m_s$, where q_s is the particle's charge, m_s is the particle's mass, and B is the local magnitude of the magnetic field.
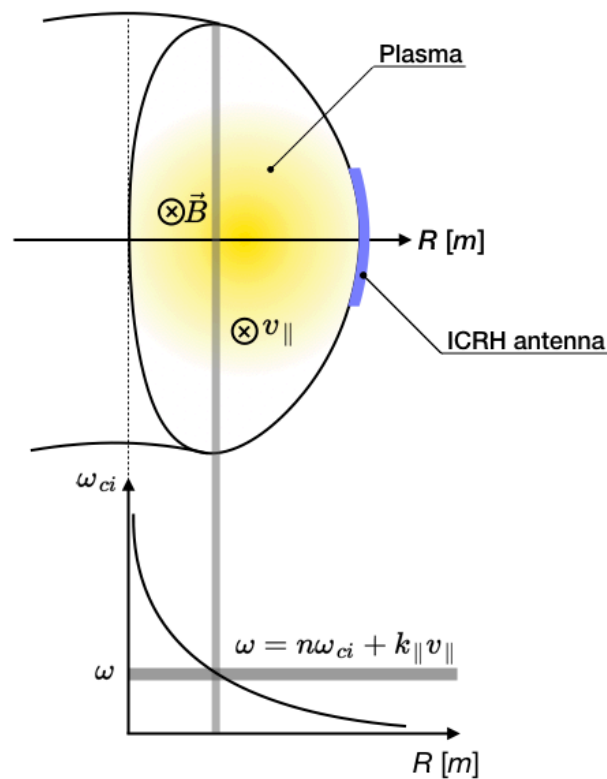

Figure 6.36. Illustration of the wave-particle resonance phenomenon during ICRH.

Transfer of energy from the waves emitted by the ICRH antenna to plasma particles is possible when the oscillations of the externally applied electromagnetic field are in resonance with the cyclotron frequency of the particles or harmonics thereof:

$$\omega = n\omega_{ci} + k_{\parallel}v_{\parallel}, \tag{6.11.1}$$

where n=1,2..., ω is the frequency of the wave and the $k_{\parallel}v_{\parallel}$ term is a classical Doppler shift due to ions velocity, where $k_{\parallel}$ and $v_{\parallel}$ are the components parallel to the magnetic field **B** of the wave-vector **k** and ion velocity **v**, respectively. Due to the fact that the magnitude of magnetic field in the plasma region decreases with the major radius R (see Fig. 6.36), there are well-defined regions where the wave-particle resonance can occur. Since there is a finite distribution of $v_{\parallel}$, these regions have finite widths. This is schematically illustrated in Figure 6.36.

In order to find a dispersion relation for the waves that can be excited in the ion cyclotron range of frequencies, the following differential wave equation (obtained from the Maxwell's equations) has to be considered:

$$\nabla \times \nabla \times \mathbf{E} - k_0^2 \frac{\epsilon_p}{\epsilon_0}\mathbf{E} = 0, \tag{6.11.2}$$

where **E** is the electric field vector, $k_0 = \dfrac{\omega}{c}$, with ω denoting the angular wave frequency and c the speed of light in vacuum. The plasma permittivity tensor in Eq. 6.11.2 is given as:

$$\frac{\epsilon_p}{\epsilon_0} = \begin{bmatrix} \epsilon_1 & i\epsilon_2 & 0 \\ -i\epsilon_2 & \epsilon_1 & 0 \\ 0 & 0 & \epsilon_3 \end{bmatrix}, \tag{6.11.3}$$

$$\epsilon_1 = 1 - \frac{\omega_{pe}^2}{\omega^2 - \omega_{ce}^2} - \sum_i \frac{\omega_{pi}^2}{\omega^2 - \omega_{ci}^2}, \quad \epsilon_2 = \frac{\omega_{ce}}{\omega}\frac{\omega_{pe}^2}{\omega^2 - \omega_{ce}^2} - \sum_i \frac{\omega_{ci}}{\omega}\frac{\omega_{pi}^2}{\omega^2 - \omega_{ci}^2}, \quad \epsilon_3 = 1 - \frac{\omega_{pe}^2}{\omega^2} - \sum_i \frac{\omega_{pi}^2}{\omega^2}.$$

The elements of the tensor contain ion cyclotron angular frequencies $\omega_{ci} = \dfrac{Z_i|q_e|B}{m_i}$, electron cyclotron angular frequencies $\omega_{ce} = \dfrac{|q_e|B}{m_e}$ as well as plasma ion $\omega_{pe}^2 = \dfrac{q_e^2 n_e}{m_e\epsilon_0}$ and electron $\omega_{pi}^2 = \dfrac{Z_i^2 q_e^2 n_i}{m_i\epsilon_0}$ angular frequencies. For simplicity, we consider here the case of a cold homogenous plasma and we assume that z axis is chosen along the direction of **B**.

The dispersion relations for the waves that can be excited in a plasma, obtained from the condition that the determinant of the set of three scalar equations deduced from Eq. 6.11.2 must be zero for non-trivial solution to exist, can be approximated as [Stix 1992]:

$$k_{\perp,FW}^2 = \frac{(k_0^2 \epsilon_R - k_\parallel^2)(k_0^2 \epsilon_L - k_\parallel^2)}{(k_0^2 \epsilon_S - k_\parallel^2)}, \tag{6.11.4}$$

$$k_{\perp,SW}^2 = \frac{k_0^2 \epsilon_3}{\epsilon_S}(k_0^2 \epsilon_S - k_\parallel^2), \tag{6.11.5}$$

where $\epsilon_L = \epsilon_1 + \epsilon_2$, $\epsilon_R = \epsilon_1 - \epsilon_2$, $\epsilon_S = \epsilon_1$, $k_\perp$ and $k_\parallel$ are the components of wave propagation vector **k** perpendicular to the magnetic filed **B** and parallel to it, respectively. The subscripts FW and SW correspond to fast wave (magnetosconic wave) and slow wave, respectively. These two types of wave are usually decoupled from each other, because the magnitude of their wave vectors is more than one order of magnitude different. However, confluences between these modes occur near the singularity of Eq. 6.11.4, when $k_0^2 \epsilon_S = k_\parallel^2$. This phenomenon is called *mode conversion*.

In general, the fast wave is elliptically polarised. The electric field can be thus written as a linear combination of a left-hand polarised component $E_+ = E_x + iE_y$ and a right-hand polarised one $E_- = E_x - iE_y$. It can be shown that power absorbed by the ions when passing through a cyclotron resonance is given by [Stix 1992]:

$$P_{abs} \propto |E_+ J_{n-1}(k_\perp \rho_L) + E_- J_{n+1}(k_\perp \rho_L)|^2, \tag{6.11.6}$$

where ρ_L is the Larmor radius of the resonant ion and *n* is the harmonic number of the cyclotron frequency, J_m is the Bessel function of the first kind. Since $k_\perp \rho_L << 1$ ($k_\perp \sim m^{-1}$, $\rho_L \sim mm$), it can be noted that for the fundamental heating (i.e. *n=1*) the absorbed power is proportional to $|E_+|^2$.

In recent decades, several efficient ICRH scenarios were identified theoretically and verified experimentally [Noterdaeme 2008]. These heating scenarios are intended to increase the energy content of the plasma. Recently, a new type of 'three-ion scenario' has been identified for multi-ion plasma. The scheme relies on matching the cyclotron layer of the third ions with the mode conversion layer. The fast wave mode conversion leads to an intense left-hand polarised electric field component E_+ favourable for radio-frequency absorption by the ions. The location of the mode conversion layer can be controlled by adjusting the concentration of the main plasma ions (e.g. H and D).

The optimal concentrations, normalised to electron density, of the main plasma ions $X_1 = n_1/n_e$, $X_2 = n_2/n_e$ are given as [Kazakov 2015]:

$$X_1 = \frac{1}{Z_1} \frac{(Z/A)_1 - (Z/A)_3}{(Z/A)_1 - (Z/A)_2}, \quad X_2 = \frac{1}{Z_2} \frac{(Z/A)_3 - (Z/A)_2}{(Z/A)_1 - (Z/A)_2}, \tag{6.11.7}$$

where Z_i and A_i are the charge state and the atomic mass of ion species, respectively. The index $i = 1$ and $i = 2$ refers to the main plasma ions, and $i = 3$ refers to the absorbing minority. An important practical application of three-ion heating scenarios will be the extension to D-T plasmas, foreseen as a fuel mix in future fusion reactors. Various impurity ions can be utilised in this case to efficiently absorb RF power, but perhaps the most useful will be Beryllium impurities.

To validate the applicability of three-ion heating scenarios, a series of dedicated experiments have been performed on JET and Alcator C-Mod tokamaks [Kazakov 2017]. The goal of these experiments was to demonstrate that indeed a small amount of ^{3}He ions can efficiently absorb RF power in H–D mixtures. In JET experiments, the edge isotopic ratio $H/(H + D)$ was varied between 0.73 and 0.92 and the ^{3}He concentration between 0.1% and 1.5%. The JET experiments were run at central electron densities $n_e \approx 4 \times 10^{19} \, m^{-3}$ and toroidal magnetic field $B = 3.2 \, T$ at a plasma current $I_p = 2 \, MA$. In order to evaluate the effectiveness of three-ion scenario, the so-called scaling laws (ITERL96-P and IPB98(y,2)) for the thermal energy confinement time τ_E were used. The results confirmed that three-ion scenarios offer an alternative, attractive and still mostly unexplored way for strong damping of electromagnetic waves in magnetised fusion plasmas [Kazakov 2017].
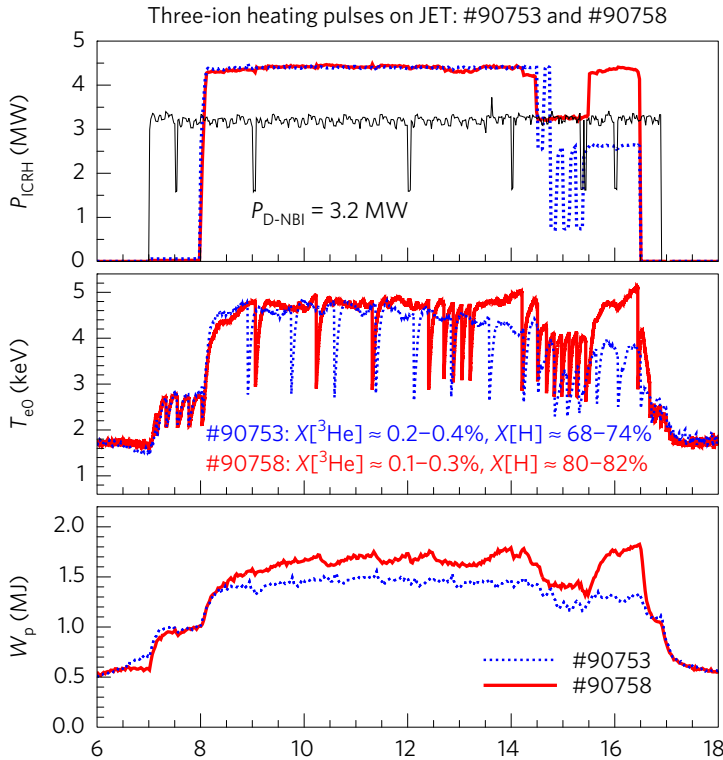

Figure 6.37 Illustration of the performance of the D–(^{3}He)–H three-ion ICRH scenario on JET tokamak. Upper panel: ICRH power P_{ICRH}, middle panel: electron temperature T_e, bottom panel: plasma stored energy W_P [Kazakov 2017].

Additional indication of the creation of energetic ions by RF waves was the observation of long-period sawtooth oscillations, as the presence of fast ions in a plasma is well-known to have a stabilising effect on sawteeth. In Figure 6.37 fast repetitive drops in electron temperature T_e (i.e. sawtooth oscillations) with a period of ≈ 0.2 s occur during the NBI-only heating phase of the JET pulse #90753 & #90758 (t = 7−8 s). The period of these oscillations increases dramatically up to ≈ 1.0 s when ICRH is applied on top of NBI heating.

An independent confirmation of accelerating ³He ions to high energies is provided by gamma-ray emission spectroscopy. Figure 6.38 shows the gamma-ray spectrum for pulse #90753 during t = 8–14 s (P_{ICRH} = 4.4 MW), recorded with the LaBr₃ spectrometer [Nocente 2013]. The observed lines originate from $^9Be(^3He, p\gamma)^{11}B$ and $^9Be(^3He, n\gamma)^{11}C$ nuclear reactions between fast ³He ions and beryllium (⁹Be) impurities. These impurities are intrinsically present in JET plasmas with the ITER-like wall. The reported plasmas were contaminated with ~0.5% ⁹Be, as estimated by charge exchange measurements. The observation of the $E_\gamma \approx 4.44$ MeV line implies immediately the presence of confined fast ³He ions with energies >0.9 MeV. Alpha particles, born in concurrent ³He + D fusion reactions, also contribute to the gamma-emission at this energy through ⁴He + ⁹Be reactions. Also, a number of characteristic gamma lines at E_γ > 4.44 MeV, originating from transitions between higher excited states of ¹¹B and ¹¹C nuclei (products of ³He + ⁹Be reactions) are observed. The excitation efficiency for such high-energy levels increases by a factor of ten when the energy of the projectile ³He ions increases from 1 MeV to 2 MeV. For comparison, the gamma ray spectrum recorded in JET pulse #91323, in which ³He ions ($\approx$1–2%) were heated as a minority with up to 7.6 MW of ICRH
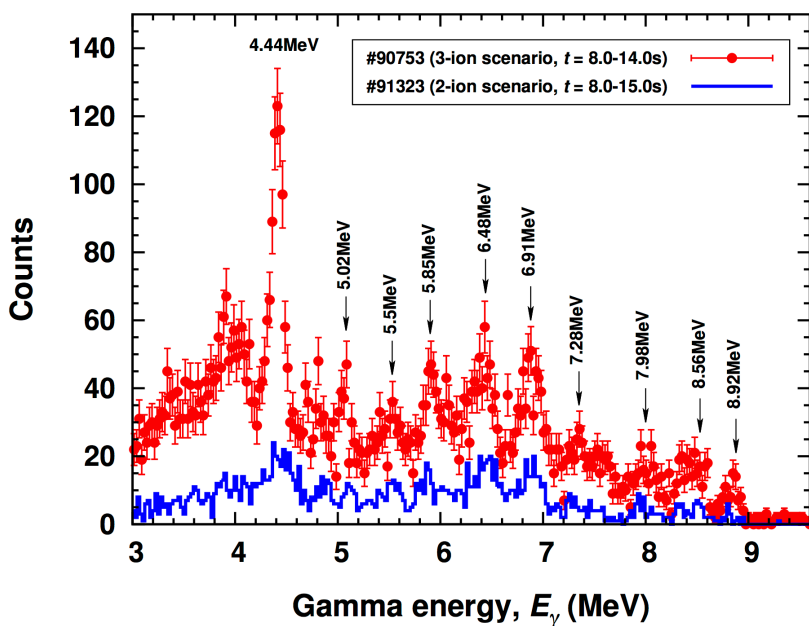

Figure 6.38 Gamma-ray spectra measured in JET pulse #90753 (three-ion scenario, in red) and in pulse #91323 ((³He)–H scenario, in blue). The error bars represent the square root of the number of counts in each channel of the spectrum and arise from the underlying Poisson statistics of the gamma-ray detection process [Kazakov 2017].
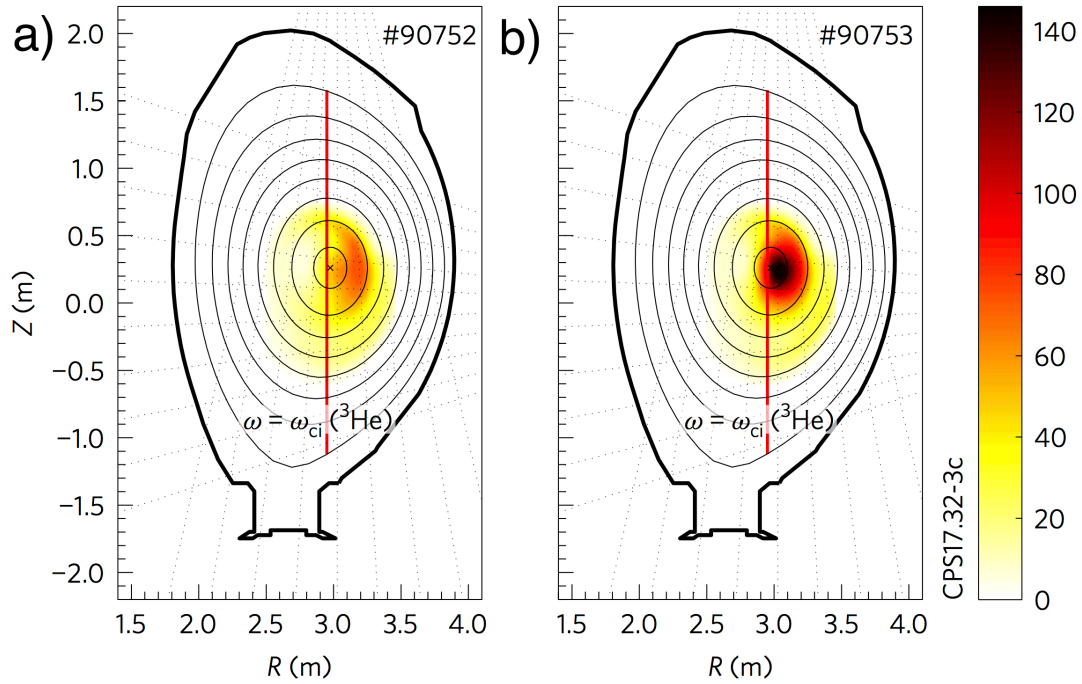
Figure 6.39 The JET plasma cross-section and 19 lines-of-sight of the neutron/gamma camera. The reconstructed high-energy gamma-ray emission ($E_\gamma \in (4.5, 9.0)$ MeV) visualises the population of the confined energetic ^{3}He ions ($E(^3He) > 1$ MeV). Pulses #90752 (a) and #90753 (b) had a nearly identical plasma composition and RF heating power except for the ICRH antenna phasing. A factor-of-two increase in the gamma-ray emissivity was observed in pulse #90753, in which 2 MW of RF power was coupled to the plasma with $+\pi/2$ phasing. Results presented in arbitrary units [Kazakov 2017].

in an almost pure H plasma is also displayed (so-called 'two-ion scenario'). Clearly, higher gamma-count rates for the three-ion pulse #90753 is observed, even though less ICRH power (a factor of two) was injected into the plasma.

The efficiency of fast-ion generation was further enhanced by changing the configuration of ICRH antenna from dipole to $+\pi/2$ phasing. This is where tomographic reconstruction methods were of special usefulness. The ICRH antenna at JET is a phased array of 4 poloidal straps. Controlling the phase between straps allows waves to be launched with different $k_\parallel$ spectra. Thus, the antenna phasing defines the dominant $k_\parallel$ (i.e. the wavenumber parallel to the magnetic field) and the spectrum of emitted waves. The $+\pi/2$ phasing (i.e. relative phasing of the four elements: $[0, \frac{\pi}{2}, \pi, -\frac{\pi}{2}]$) launches waves predominantly in the direction of the plasma current with typical values $|k_\parallel^{(ant)}| \approx 3.4 \ m^{-1}$, which is two times smaller then for dipole phasing ($|k_\parallel^{(ant)}| \approx 6.7 \ m^{-1}$). Since the width

of the absorption zone scales with $|k_\parallel|$, reducing it has the advantage of increasing the absorbed RF power per ion. Furthermore, the $+\pi/2$ phasing allows one to exploit the RF-induced pinch effect, beneficial to localise the energetic ions towards the plasma core [Mantsinen 2002]. The results of two-dimensional tomographic reconstruction of the $E_\gamma \in (4.5,\ 9.0)$ MeV gamma-ray emission for two comparable three-ion heating pulses #90752 and #90753 are shown in Figure 6.39. For the reconstruction, data from JET neutron/gamma camera equipped with 19 CsI detectors has been used (see Sec 6.2). For both pulses, plasma had a nearly identical composition (X[H] $\approx$ 70 – 75%, X[^{3}He] $\approx$ 0.2 – 0.3%) and RF conditions (P_{ICRH} = 4.2 MW). However, in pulse #90752 ICRH power was applied using dipole phasing solely, while in pulse #90753 about half of the ICRH power (2.1 MW) was launched with $+\pi/2$ phasing.

The reconstructed high-energy gamma-ray emission ($E_\gamma \in (4.5,9.0)$ MeV) allows to visualise the population of the confined energetic ^{3}He ions (E(^{3}He) > 1 MeV). It can be clearly seen that the energetic ^{3}He ions are more centrally located and the number of gamma-ray counts increases by a factor of two in pulse #90753. The same holds for the period of the sawtooth oscillations. This example demonstrates the power and usefulness of tomographic methods in fusion science - in this case gamma-ray emissivity reconstruction.

7. Recent advances in plasma tomography

Based on: M. Riva, (...), J. Bielecki, et al., Fus. Eng Des. 123, 873 (2017),
G. Boltroczuk, (...), J. Bielecki, et al., Fus. Eng Des. 123, 940 (2017),
J. Bielecki et al., Fus Eng. Des. 112, 646 (2016).

Over recent years a lot of progress has been made in the field of plasma tomography diagnostics. New tomographic techniques have been developed, as it was shown in the previous sections, but also new instrumentation and measurement techniques have been applied. Perhaps it is fair to claim that a large part of the progress in this field was stimulated by two factors: the construction of ITER and its diagnostics and the preparation for the second DT campaign (DT2) at JET. Since the first topic is definitely outside the scope of this monograph, the interested Reader is referred to a series of articles [Chugunov 2011, Petrizzi 2007]. The long-term preparation for DT2 at JET resulted in modifications of both gamma and neutron tomographic systems. In this chapter the advances in plasma tomography, made during the preparations for DT2, are presented and supplemented with the information on new plasma tomography techniques elaborated outside of the tokamak plasma field. At the end of the chapter, modern trends in plasma tomography are outlined.

During DT2, a particular attention will be paid to 4.44 MeV gamma-rays emitted in the $^9Be(\alpha, n\gamma)^{12}C$ reaction, providing the profile of fast confined α-particles [Kiptily 2005]. In addition, tomography of the measured hard X-ray emission (bremsstrahlung radiation) can provide detailed data on the temporal evolution and spatial structure of runaway electron beams during expected disruptions. The gamma-ray detection system, dedicated for measurements in DT plasma, has to be able to register spectra at high count rates, up to approximately 500 kHz. At the same time, the detectors should be characterised by a full width at half maximum (FWHM) of about a few percent for 3 - 6 MeV gamma-rays. The upgraded Gamma-ray Camera at JET features a set of new LaBr$_3$:Ce scintillators, with a fast light output decay (~20 ns) and energy resolution of a few percent, coupled to photodetectors with a fast response time - Multi-Pixel Photon Counters (MPPC) [Zychor 2016]. The previously installed CsI:Tl scintillators were coupled to PIN photodiodes in the camera. PIN photodetectors are characterised by small dimensions, low operating voltage and immunity to a magnetic field. However, the main drawback of PIN diodes is a low gain coefficient of ~1, requiring the usage of a preamplifier for spectrometry measurements. This resulted in a relatively slow response time which is not suitable for measurements at high count rates expected during DT2 experiments. Contrary, the MPPC features fast response time, high gain coefficient and high photon detection efficiency, resulting in good energy resolution, and still maintaining the immunity to magnetic field and small dimensions. The device also features a low bias voltage in

comparison with photomultiplier tubes. However, the main drawback of MPPC is a gain sensitivity to temperature and voltage. To reduce the influence of bias voltage fluctuations, a high quality voltage supply with a voltage ripple less than 3 mV is exploited to bias the MPPC. To reduce the noise pick-up by the detector, μ-metal shielded signal cables with additional electromagnetic shielding are used. A limited dynamic range and non-linearity of a signal response are another drawbacks when bright and fast scintillators are in use. Thus, the gain of the device is repeatedly monitored using a gamma-ray source available inside the JET gamma-ray camera. Due to a very strong voltage-temperature dependence for MPPC-based detectors, a device for real-time temperature monitoring and MPPC gain stabilisation was designed and constructed in National Centre For Nuclear Research (NCBJ) [Zychor 2016]. The device controlled by a personal computer uses a measured dependence of a breakdown voltage on temperature to maintain a constant value of the MPPC gain. Using the device, the gain fluctuations can be kept at the level of 1% [Zychor 2016]. Since the detectors used in experiments will be exposed high count rates during DT2, they should operate with a short pulse duration to minimise the number of pile-up events. Thus, the output signals are additionally shortened using a resistance-capacitance passive differentiator circuit with a pole zero cancellation. With the signal shortening system, the total length of a signal is ~120 ns, with a rise time of ~17 ns and a fall time of ~90 ns.

The LaBr$_3$:Ce scintillator contains long-lived naturally occurring ^{138}La isotope. The abundance of this isotope is 0.0902% and its half-life is 1.05×10^{11} years. ^{138}La has two decay channels: by electron capture into ^{138}Ba with 66.4% probability and by beta decay into ^{138}Ce. The daughter nucleus emits 1436 and 789 keV gamma-rays, respectively. For ^{138}Ba, the K – shell and L+M – shell X-ray binding energies are 37.4 keV and 5.6 keV, respectively. Due to non-proportional response effects, an equivalent energy, i.e. the energy that is detected by LaBr$_3$:Ce, is only 35.5 and 4.5 keV. K and L+M cascade peaks are detected as pile ups with the 1436 keV gamma-ray of the ^{138}Ba de-excitation, therefore 1472 and 1440 keV gamma lines are observed. Thus, ^{138}La is a source of an additional intrinsic gamma-ray background and beta self-contamination of the crystal. On one hand, such an intrinsic activity poses a serious limit for the application in low count rate experiments. On the other hand, the intrinsic lines can be used for on-line gain monitoring and calibration.

The neutron detection system for tomographic applications during DT2 also required a thorough upgrade. During the first DT campaign in 1997, the BC418 neutron detectors worked up to ~1.2×10^6 cps (counts above 10 MeV threshold). However, the presence of higher NBI power in future DT campaigns might imply higher rates and a demanding value of ~2×10^6 cps has been set as a target for the neutron camera diagnostic. Moreover, the BC418 neutron detectors worked with an analogue DAQ having several limitations (no possibility of accurate pulse height spectra measurements, no raw data storage, complex

calibration procedure etc.). To overcome the above mentioned limitations during DT2 campaign, an upgrade project was launched with the main objective of increasing the performance and reliability of the 14 MeV neutron measurements performed by BC418 detectors.

The objective was achieved by installation of a cutting edge dedicated digital data acquisition system. The system features high throughput and is able to perform on-line data pre-processing. The raw data (i.e. pulses from the photomultiplier tubes coupled to BC418 detectors) are stored on local computers and can be further processed and analysed off-line. The off-line analysis includes pile-up rejection, pulse height spectra processing, calibration, DT neutron count rate estimation, etc. The hardware architecture selected for the neutron camera acquisition system is based on a set of rack-mounted units shown in Figure 7.1a. Each unit is equipped with a 4-slots backplane (Figure 7.1b) hosting up to 4 PC boards (Figure 7.1c) and each PC board accommodates a two-channel digitiser through a PCIe×8 carrier board. Two rack units with all backplane slots occupied (16 acquisition channels) and one rack unit with 2 backplane slots occupied (4 acquisition channels) are used to provide full coverage of the neutron camera LoS and a spare acquisition channel. The 10 two-channel digitisers (X6-400M, Innovative Integration, US) are equipped with a FPGA, external clock and trigger; each channel features a 14 bit ADCs with software selectable sampling rate up to 400MS/s. The FPGA board is mounted on the PCIe×8 carrier as a high speed Switch Mezzanine Card (XMC), as shown in Figure 7.1d. Some specific design solutions were made in order to cope with the high data throughput foreseen in the future DT2 campaign. Large on-board RAM and use of a fast bus for FPGA ensure proper data buffering and fast data transfer. The resources available per acquisition channel have been maximised by application of a single FPGA and a single PC for each couple of acquisition channels. This solution ensures that the system is robust
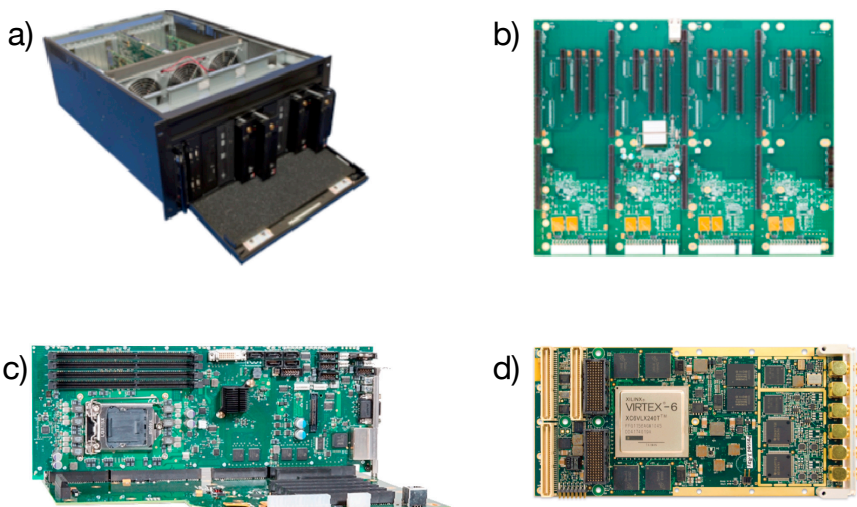

Figure 7.1 Elements of the upgraded Neutron Camera DAQ. a) 5U-rack units, b) a 4-slots backplane, c) a PC board mounted on the backplane, d) a two-channel digitiser (X6-400M) with FPGA board [Riva 2017].

against data overload on the FPGA/CPU and minimises the risk of acquisition board/PC failure. Sampling rate can be flexibly adjusted. The possibility of downgrading the sample rate via software allows to easily select between high performance settings (in terms of energy resolution, pile-up analysis etc.) or data reduction. The custom FPGA firmware, specifically dedicated to pulse acquisition and pre-processing, has been designed in ENEA [Riva 2007]. The firmware takes advantage of a non-continuous acquisition mode in which a selectable number of samples (data window) are acquired when a pulse is detected and the size of the window is dynamically extended depending on the presence of additional pulses. Such a procedure reduces the amount of stored data and increases the maximum count rate sustainable by the system. Figure 7.2 shows a layout of the whole system. Each detector signal passes through a fast amplifier and is then split in two paths, the first connected to the digital system and the other to the old analogue system. The reference CLOCK/GATE signals and network are routed to each acquisition board/PC by means of dedicated distribution units.
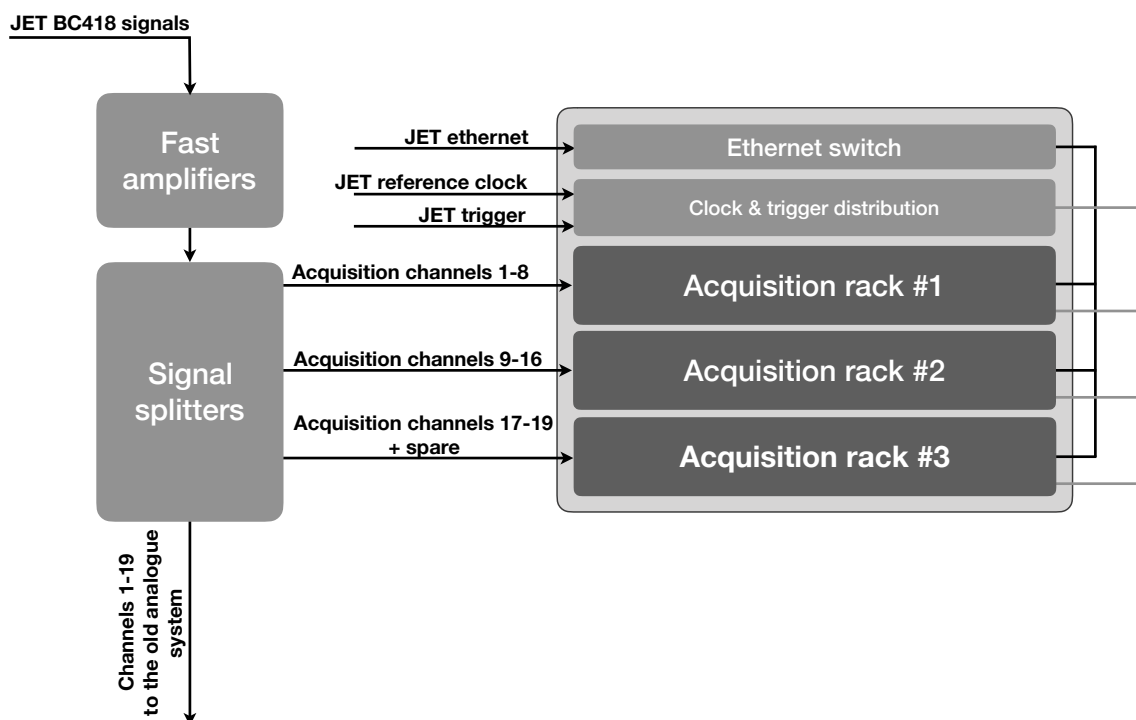
Figure 7.2 Block diagram of the JET neutron camera data acquisition system.

The new system was at first tested and calibrated with ^{22}Na gamma sources embedded in the neutron camera detector boxes. Further tests were conducted with Frascati Neutron Generator and the final tests were performed by registering neutrons from ~50 DD plasma discharges at JET (#87291 - #87595). Pulse height spectra from these discharges were summed up in order to obtain satisfactory statistics for 14 MeV burn-up neutrons.

Figure 7.3 shows the collected pulse height spectrum with highlighted different regions related to DD neutrons, DT neutrons and gamma rays. Indeed, since BC418 detectors have no neutron gamma discrimination capabilities, 14 MeV neutron detection is obtained by setting a threshold (typically 10 MeV) on the energy. Above this threshold, the counts in the spectra are considered as originating solely from 14 MeV neutrons.
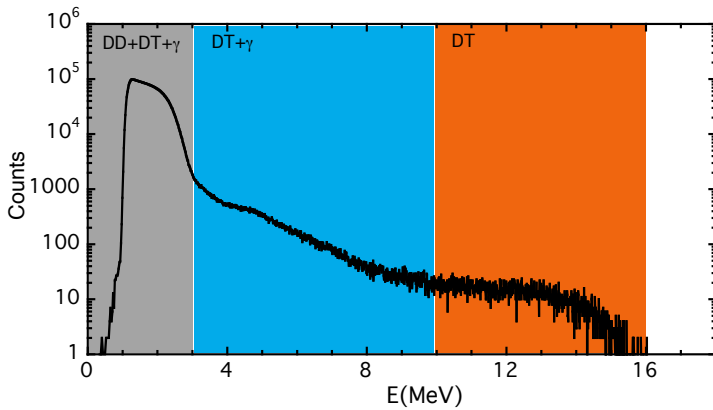
Figure 7.3 Pulse height spectrum of neutrons collected from ~50 DD JET plasma discharges. Three regions related to DD and DT neutrons as well as to gamma rays are highlighted [Riva 2017].

Since SXR and HXR emitted from a plasma provide complementary information, it is beneficial to construct a detector capable of a simultaneous registration of radiation in both energy regions. Recently a conceptual design of such a detector has been proposed for studying of SXR and HXR emission from dense magnetised plasma in the Plasma Focus PF-24 device (PF-24) [Bielecki 2016]. In order to reconstruct the SXR and HXR emissivity in a radial cross-section of the plasma column, the experimental setup

Figure 7.4 The geometrical layout of the tomographic setup designed for PF-24 device [Bielecki 2016].

composed of three X-ray pinhole cameras has been designed. The geometrical layout of the setup is shown in Figure 7.4. Each of the three cameras with a magnification factor = 2 and a horizontal field of view (FoV) ≈ 5° is equipped with a pair of 16-element Si photodiode linear arrays arranged in two layers. This layout of th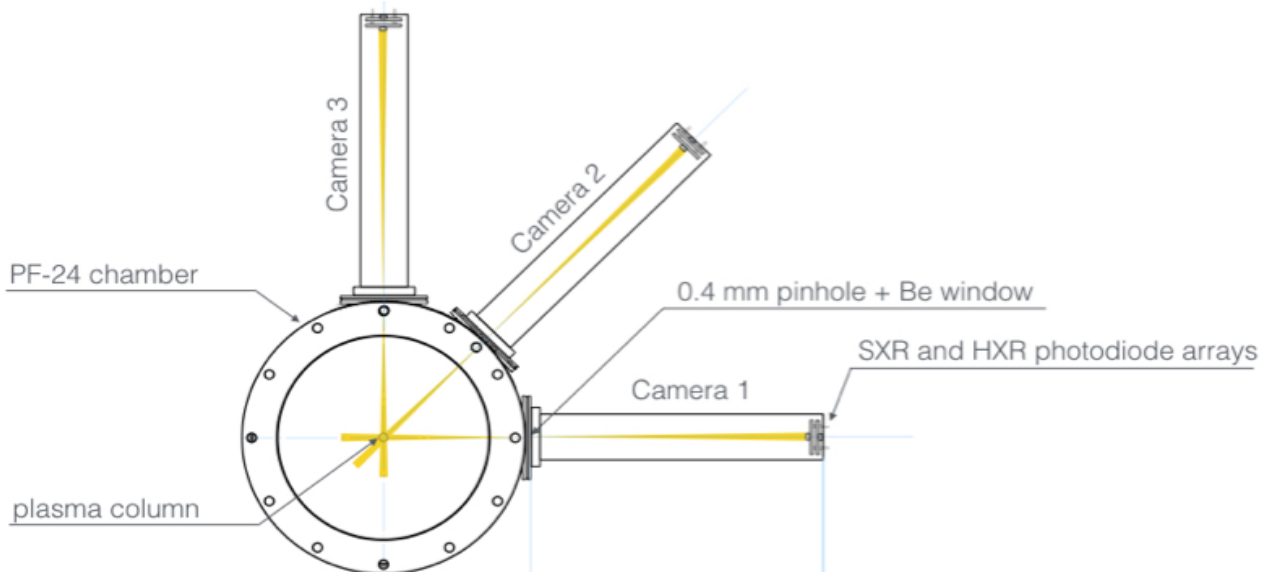e detectors enables a dual-energy imaging (i.e. registration of the line-integrated signals of SXR and HXR during a single discharge of the plasma focus device [Bielecki 2015b]) and a tomographic inversion of X-ray emission in 2D cross-section of the plasma column. The pinhole diameter of the cameras has been chosen to be 0.4 mm. This implies the spatial resolution of 0.6 mm and the geometrical blur of a point source = 1.2 mm. The geometrical blur is comparable to the dimensions of a single sensitive element of the array (1.2 mm × 2 mm). The design of the camera's detection system is shown in Figure 7.5. The soft X-ray detector is based on a 16-element Si photodiode array without any additional scintillation element, while for HXR detection a similar photodiode array covered by a layer of NaI(Tl) scintillator (common for each element of the array) is used. The applied Si photodiode arrays exhibit low optical and electrical cross-talk between the neighbour elements, what ensures signal purity.
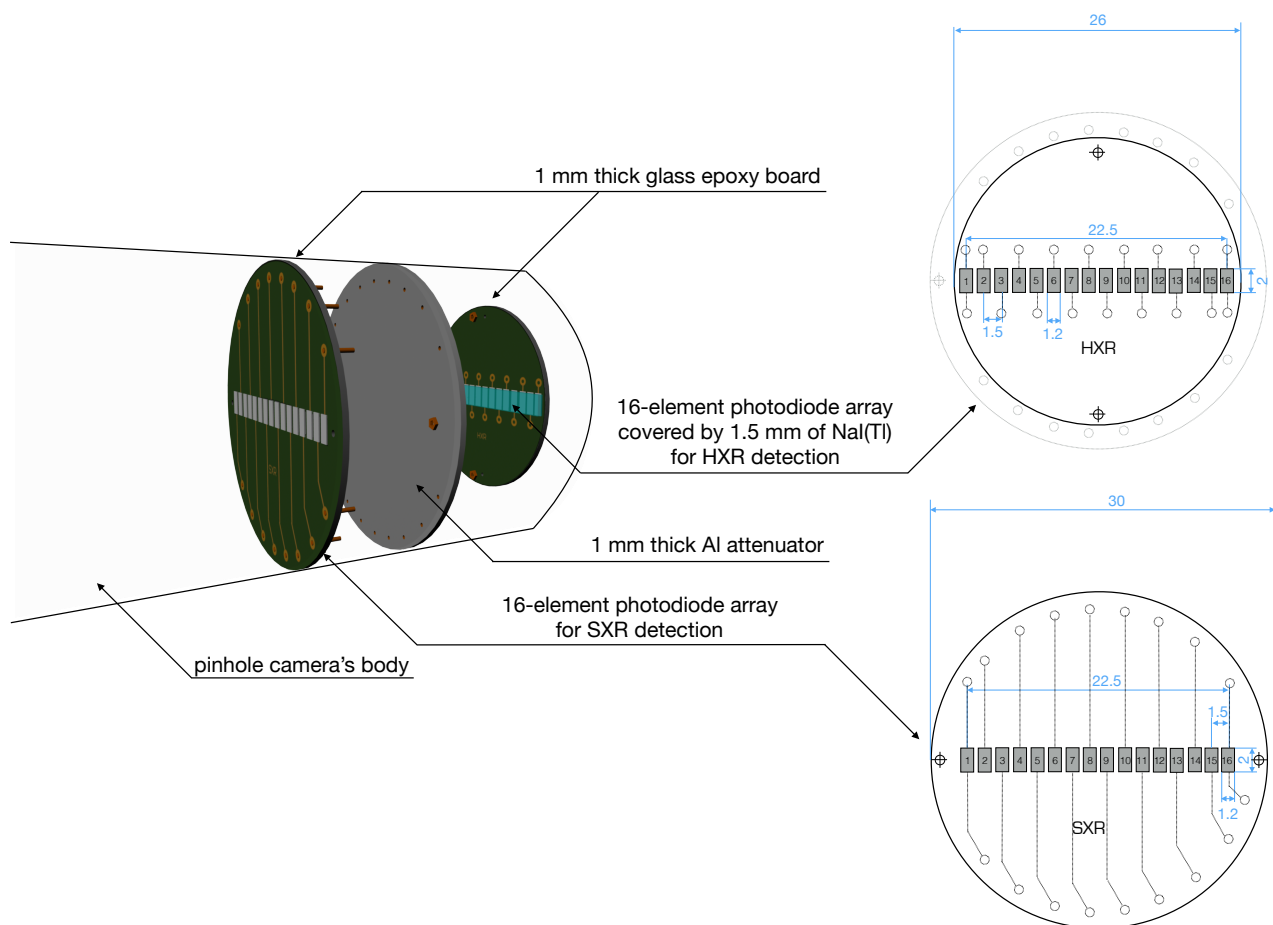

Figure 7.5 The design of the dual-energy detection system [Bielecki 2016].

In order to prevent the attenuation of SXR, all three cameras are designed to operate in vacuum. The walls of the camera must be opaque for the X-rays generated by the plasma focus device. These conditions are fulfilled adequately when walls of the camera are shielded by 4 mm of lead (~1.5% transmittance for 200 keV X-rays). In order to reduce the thickness of pinhole structure and consequently to suppress the additional blurring effect, the pinhole plate is designed to be made of 0.5 mm thick Bi, ensuring ~1%, ~6% and ~60% transmittance for 50, 100 and 200 keV X-rays, respectively. Moreover, the diameter of the pinhole plate is kept small (2 mm) to prevent entering of the penetrating HXR radiation from the outside of the pinhole into the camera. The X-rays emitted by the plasma are transferred from the PF-24 experimental chamber to each of the cameras by an 8 μm thick Be window. The thickness of the Be windows was selected to ensure a transmittance >0.4 for the 1 keV X-rays and the necessary mechanical strength in the conditions of shock wave influence. The parameters of the detection system have been chosen and optimised by means of the Geant4 calculations [Bielecki 2016]. The dedicated signal processing integrate circuits have been also designed. The photodiode arrays, managed by commercial driver circuits, are coupled to a read-out system based on a FPGA development board and an analog I/O module. The tomographic system can be used with the reconstruction method based on the Tikhonov regularisation to study spatially- and temporally-resolved simultaneous emission of SXR and HXR from a plasma pinch [Bielecki 2016].

The current trends in plasma tomography seem to point toward the real-time reconstructions for on-line control of a fusion device or to mitigate MHD instabilities [Loffelmann 2016]. The real-time capabilities of inversion techniques go hand in hand with hardware developments. To make such reconstructions possible it is necessary to utilise dedicated machines (e.g. based on FPGA or GPUs) or high-performance computing clusters. In [Carvalho 2008] a tomographic method based on the Fourier-Bessel series expansion was implemented into a dedicated FPGA, for a real-time (i.e. reconstruction time < 0.1 ms) plasma control in the ISTTOK tokamak. Techniques for real-time tomographic reconstruction from sparse data sets based on neural networks seem to be computationally less demanding. However, neural networks require a well-prepared, sufficiently large and general training set. When the network is properly trained, the subsequent inversion is rapid. In [Ronchi 2010], the authors proposed a method based on neural networks for real-time tomographic inversion of neutron emissivity at JET tokamak. Neural networks were also applied, with a perspective of real time application, for bolometric tomography at JET [Barana 2002]. Recently, Matos and co-authors applied deep learning techniques for plasma tomography using the bolometer system at JET [Matos 2017].

8. Summary

Computed tomography methods have been in use for over 40 years and completely changed the approach to medical imaging and diagnostics. Further developments in CT technology have led to a widening of its area of use: from its primary medical application to many areas like material science, archaeology, geophysics, atmospheric science, oceanography, and other fields. Also, plasma physics and fusion research benefit from these advances. As it was shown, the methods specific to plasma tomography inherit some features from medical CT, however due to the different nature of measurement systems available for fusion devices, some dedicated approaches have to be developed. Very often the reconstruction process is based on regularisation. This regularisation is performed either explicitly, as it was presented in Sec. 6.6 and Sec. 6.7, or using other methods that utilise e.g. Tikhonov-like objective function (Sec. 6.9 and Sec. 6.10). In this monograph a few novel and original approaches to plasma tomography have been presented (e.g. novel approach to Tikhonov regularisation, application of genetic algorithms or Metropolis-Hasting Monte Carlo method) along with their applications.

It was shown that the plasma tomographic methods are invaluable tools in modern tokamak experiments. Neutron plasma tomography provides information on spatially resolved reaction rates and alpha particle profile birth. Gamma tomography played the crucial role in 'three-ion scenario' experiment where the spatial distribution of energetic ions was reconstructed, allowing for evaluation of the efficiency of radio-frequency resonance heating (Sec. 6.11). Soft X-ray plasma tomography provides valuable information on particle transport as shown in Sec. 6.7. Complementary, hard X-ray plasma tomography gives an insight into the energy distribution function of runaway electrons.

A lot of effort has been recently devoted to test, validate and compare results obtained with different methods. This is because the problem of tomographic inversion in plasma physics is usually highly ill-posed and it is never possible to obtain exact solutions. Thus, the presented methods can be used in a complementary manner. For instance, as it was show in Sec. 6.6 and Sec. 6.7, using two methods based on Tikhonov reconstruction, but with different forms of the functional, can lead to enhancement of different features of the reconstructed emissivity.

A researcher who develops or uses a tomographic method in plasma research must be critical towards the results and must try different approaches to understand which kind of reliable information can be obtained. It was shown that the most crucial element of a reliable inversion method is the choice of objective function and the included *a priori*

knowledge. It seems to be beneficial to base this knowledge on results of physical measurements from other available plasma diagnostics (as shown in Sec. 6.6). Then, an objective function that describes a physical property together with optimisation that takes knowledge of the experiment into account (e.g. estimated noise level) can help to obtain physically meaningful solutions.

Although the choice of the regularisation parameter may be seemingly quite arbitrary, it is another important factor for a successful retrieving of the plasma emissivity. Again, when the standard methods fail, physical information from other diagnostics can be helpful (Sec. 6.6.) Furthermore, a special care has to be taken with the discretisation because a limited effort (e.g. better numerical implementation) can lead to large computational gains. On the contrary, too fine discretisation grid can significantly increase computational demands without significant improvement of the solution.

Similarly, special care has to be taken during construction of new tomographic diagnostics. An engineer or a scientist who designs and constructs such a system must take into consideration the geometrical aspects of LoS, adequate knowledge the LoS layout as well as alignment and calibration of the instrumentation to avoid channel cross-talks and correlated drifts.

The development and application of new detectors enhanced capabilities of the plasma tomographic systems. Both, count-rate capabilities, and higher energy resolution have been achieved. The rapid development in electronics and computer science allowed to build fast data acquisition systems. In plasma tomography, application of such systems opened possibilities of real-time data acquisition and processing. However, at the same time, a progress in development of real-time reconstruction methods must be made. This process has already started and a few new approaches appeared (e.g. fast implementation of Tikhonov regularisation or application of neural networks).

I strongly believe that the progress in both plasma tomography instrumentation and plasma tomography inversion methods will continue and speed up. Upcoming ITER operation will bring new challenges. Some knowledge and experience on plasma tomography, gained at the existing tokamaks, will be certainly utilised at ITER. However, ITER will work in completely different conditions, i.e. it is a much bigger device (major radius = 6.2 m), with higher magnetic field (toroidal field = 5.3 T) and much higher expected neutron flux (fusion power up to 400 MW) [Aymar 2002]. This implies much more harsh environment for measurements which will result in higher radiation background, increased noise from high-power heating systems, requirement of additional shielding against the tokamak magnetic field and backscattered radiation, etc. Some of these aspects will be partly tested and mitigated based on the experience from the upcoming second DT campaign at JET. Some of them will have to be overcome during future operation of ITER.

9. Appendices

9.1 Convolution theorem

The convolution of functions $f(x, y)$ and $h(x, y)$ is given by:

$$g(x, y) = \iint_{-\infty}^{\infty} h(x - t, y - s)f(t, s)dtds = h * f, \tag{9.1.1}$$

where * denotes convolution of functions.

Let $F(\xi, \eta)$ be the Fourier transform of $f(x, y)$:

$$F(\xi, \eta) = \iint_{-\infty}^{\infty} f(x, y)e^{(-2\pi i(\xi x + \eta y))}dxdy = \mathscr{F}(f(x, y)), \tag{9.1.2}$$

and $H(\xi, \eta)$ be the Fourier transform of $h(x, y)$:

$$H(\xi, \eta) = \iint_{-\infty}^{\infty} h(x, y)e^{(-2\pi i(\xi x + \eta y))}dxdy = \mathscr{F}(h(x, y)), \tag{9.1.3}$$

then the Fourier transform of $g(x, y)$ is given as:

$$G(\xi, \eta) = \iint_{-\infty}^{\infty} g(x, y)e^{(-2\pi i(\xi x + \eta y))dxdy} = \iint_{-\infty}^{\infty} \left[\iint_{-\infty}^{\infty} h(x - t, y - s)f(t, s)dtds\right]e^{(-2\pi i(\xi x + \eta y))}dxdy =$$

$$= \iint_{-\infty}^{\infty} f(t, s)e^{(-2\pi i(\xi t + \eta s))}\left[\iint_{-\infty}^{\infty} h(x - t, y - s)e^{(-2\pi i(\xi(x-t)+\eta(y-s)))}dxdy\right]dtds =$$

$$= \iint_{-\infty}^{\infty} f(t, s)e^{(-2\pi i(\xi t + \eta s))}H(\xi, \eta)dtds = H(\xi, \eta)F(\xi, \eta) = \mathscr{F}(h(x, y) * f(x, y)) \tag{9.1.4}$$

Thus, the Fourier transform of the convolution of functions $f(x, y)$ and $h(x, y)$ is the pointwise product of Fourier transforms $F(\xi, \eta)$ and $H(\xi, \eta)$.

∎

9.2 Proof of relationship 4.8.9

$$\mathscr{F}\big(g(r,\theta)\big) = \mathscr{F}\left(\frac{1}{|r|}\big(h(\theta+\pi/2)mod\pi\big)\right) = \int_0^\pi \int_{-\infty}^\infty g(r,\theta)e^{-i2\pi r\rho\cos(\theta-\Theta)}|r|\,dr\,d\theta =$$

$$= \int_0^\pi h(\theta+\pi/2)mod\pi)\left[\int_{-\infty}^\infty e^{-i2\pi\rho\cos(\theta-\Theta)}dr\right]d\theta = \int_0^\pi h((\theta+pi/2)mod\pi)\delta(\rho\cos(\theta-\Theta)d\theta =$$

$$= \frac{1}{|\rho|}\int_0^\pi h(\theta')\delta(\sin(\theta'-\Theta))d\theta' = \frac{1}{|\rho|}h(\Theta), \qquad (9.2.1)$$

where $\theta' = (\theta+\pi/2)mod\pi$ and the following property of Dirac delta was used:

$$\delta(\sin(t)) = \sum_k \delta(t+\pi k). \qquad (9.2.2)$$

■

The above proof is not strict since the function $1/|r|$ is not square integrable in 2D, so its 2D Fourier transform exists only in the sense of distributions.

9.3 Filter functions commonly used in CT

Ram-Lak: $A(\nu) = rect\left(\dfrac{\nu}{2\nu_0}\right)$ (9.3.1)

Shepp-Logan: $A(\nu) = |\,Sinc\left(\dfrac{\nu}{2\nu_0}\right)|$ (9.3.2)

Henning: $A(\nu) = \dfrac{1}{2} + \dfrac{1}{2}cos(\pi\nu/\nu_0)rect\left(\dfrac{\nu}{2\nu_0}\right)$ (9.3.3)

Hamming:

$A(\nu) = 0.54 + 0.46cos(\pi\nu/\nu_0)rect\left(\dfrac{\nu}{2\nu_0}\right)$ (9.3.4)

Butterworth: $A(\nu) = \dfrac{1}{\sqrt{1 + (\nu/\nu_0)^{2n}}}, \, n \geq 0$ (9.3.5)

Parzen: $A(\nu) = \begin{cases} 1 - 6(\nu/\nu_0)^2(1 - |\nu|/\nu_0); & |\nu| \leq \nu_0/2 \\ 2(1 - |\nu|/\nu_0)^3; & \nu_0/2 \leq |\nu| \leq |\nu_0 \\ 0; & \text{otherwise} \end{cases}$ (9.3.6)
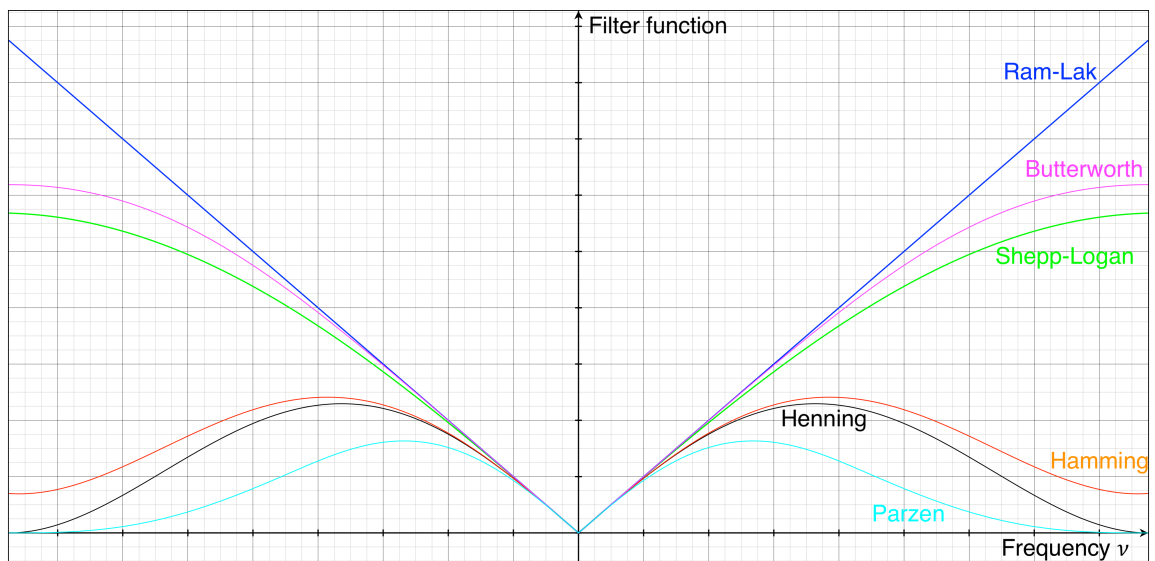

Figure 9.1 Plot of the filter functions multiplied by the ramp function |ν| in the frequency domain

9.4 Tuy's condition

The FDK reconstruction algorithm presented in Sec. 4.13 is exact only when the source trajectory Γ in $\mathbb{R}^3$ satisfies the Tuy's condition relative to the object, i.e. if every plane which intersects the object also intersects Γ transversely.

The conventional single planar orbit (Fig. 9.2a) obviously does not satisfy this condition, whereas two orbits arranged as illustrated in Figure 9.2b, as well as a helical orbit in Figure 9.2c do satisfy the condition. The use of FDK algorithm with planar orbit can introduce some artefacts. In fact, in this case only the central plane is reconstructed exactly.
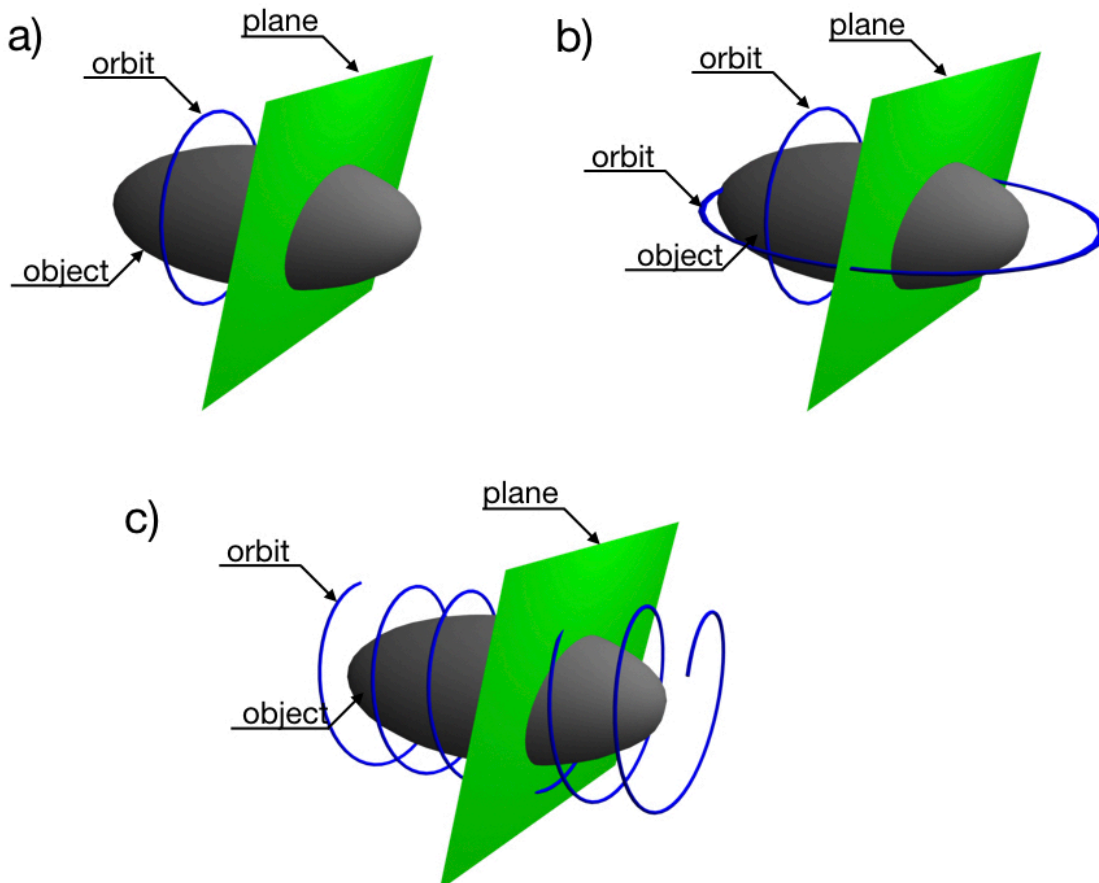

Figure 9.2 Illustration of Tuy's conditions. a) circular orbit does not satisfy the Tuy condition, b) two orbits satisfying the condition and c) helical orbit also satisfying the condition.

9.5 Singular Value Decomposition (SVD) and Generalised Singular Value Decomposition (GSVD)

An $m \times n$ $(m > n)$ real matrix $\mathbf{A}$ can be written as the so-called Singular Value Decomposition of the form:

$$\mathbf{A} = \mathbf{USV}^{-1}, \tag{9.5.1}$$

where in general $\mathbf{U}$ is an $m \times p$ orthogonal matrix, $\mathbf{S}$ is an $p \times p$ diagonal matrix and $\mathbf{V}$ is an $p \times n$ orthogonal matrix. A pictorial representation of the SVD is shown in Figure 9.3. The diagonal elements of matrix $\mathbf{S}$ are singular values σ_i of the original matrix $\mathbf{A}$. The singular values are non-negative and arranged in descending order:

$$0 \leq \sigma_1 \leq \sigma_2 \leq \ldots \leq \sigma_p \leq 1. \tag{9.5.2}$$

Columns of $\mathbf{U}$ are the left singular vectors and $\mathbf{V}^{\mathbf{T}}$ are the right singular vectors. The SVD represents an expression of the original matrix $\mathbf{A}$ in the coordinate system where the covariance matrix is diagonal. Calculating the SVD consists of finding the eigenvalues and eigenvectors of $\mathbf{AA}^{\mathbf{T}}$ and $\mathbf{A}^{\mathbf{T}}\mathbf{A}$. The eigenvectors of $\mathbf{A}^{\mathbf{T}}\mathbf{A}$ make up the columns of $\mathbf{V}$ while the eigenvectors of $\mathbf{AA}^{\mathbf{T}}$ make up the columns of $\mathbf{U}$. Also, the singular values σ_i in $\mathbf{S}$ matrix are square roots of eigenvalues from $\mathbf{AA}^{\mathbf{T}}$ or $\mathbf{A}^{\mathbf{T}}\mathbf{A}$.
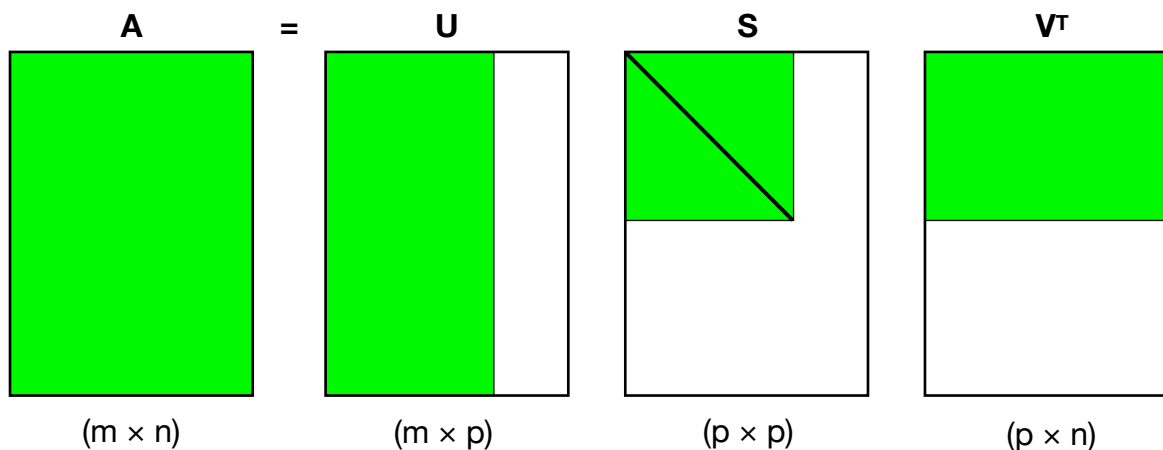

Figure 9.3 A pictorial representation of the SVD.

The generalisation of SVD for an $m \times n$ $(m > n)$ real matrix $\bar{\mathbf{A}}$ and a $p \times n$ matrix $\bar{\mathbf{B}}$ ($m \geq n \geq p$ and $rank\,\bar{\mathbf{A}} = p$) is the following decomposition (Generalised Singular Value Decomposition):

$$\bar{\mathbf{A}} = \bar{\mathbf{U}}\begin{pmatrix} \bar{\mathbf{S}} & \mathbf{0} \\ \mathbf{0} & \mathbf{I}_{n-p} \end{pmatrix}\bar{\mathbf{X}}^{-1}, \qquad \bar{\mathbf{B}} = \bar{\mathbf{V}}(\mathbf{M}\ \mathbf{0})\bar{\mathbf{X}}^{-1}. \tag{9.5.3}$$

In the above equation $\mathbf{I}_{n-p}$ is an $(n-p) \times (n-p)$ identity matrix, $\bar{\mathbf{U}}$ is an $m \times n$ orthogonal matrix, $\bar{\mathbf{V}}$ is a $p \times p$ orthogonal matrix and $\bar{\mathbf{X}}$ is an $n \times n$ non-singular matrix. $\bar{\mathbf{S}}$ is a $p \times p$ diagonal matrix with elements λ_i such that:

$$0 \leq \lambda_1 \leq \lambda_2 \leq \ldots \leq \lambda_p \leq 1. \tag{9.5.4}$$

$\bar{\mathbf{M}}$ is a $p \times p$ diagonal matrix with elements μ_i such that:

$$1 \geq \mu_1 \geq \mu_2 \geq \ldots \geq \mu_p \geq 0. \tag{9.5.5}$$

The values of λ_i and μ_i are normalised, i.e.:

$$\lambda_i^2 + \mu_i^2 = 1, \quad i = 1,2,...,p. \tag{9.5.6}$$

The generalised singular values of $(\bar{\mathbf{A}}, \bar{\mathbf{B}})$ pair are defined as the following ratios:

$$\gamma_i = \frac{\lambda_i}{\mu_i}. \tag{9.5.7}$$

Moreover, the following conditions hold for $\bar{\mathbf{A}}$, $\bar{\mathbf{B}}$ and $\bar{\mathbf{X}}$ matrices:

$$\bar{\mathbf{X}}^{\mathrm{T}}\bar{\mathbf{A}}^{\mathrm{T}}\bar{\mathbf{A}}\bar{\mathbf{X}} = \begin{pmatrix} \bar{\mathbf{S}}^2 & \mathbf{0} \\ \mathbf{0} & \mathbf{I} \end{pmatrix}, \quad \bar{\mathbf{X}}^{\mathrm{T}}\bar{\mathbf{B}}^{\mathrm{T}}\bar{\mathbf{B}}\bar{\mathbf{X}} = \begin{pmatrix} \bar{\mathbf{M}}^2 & \mathbf{0} \\ \mathbf{0} & \mathbf{0} \end{pmatrix} \tag{9.5.8}$$

Note that the example of GSVD application presented in Sec. 6.6 was a special case when $p = n$.

9.6 Discrete Laplace operator

On an $m \times n$ grid, the second-order centred-difference approximation of the Laplace operator acting on a function **f** can be written as:

$$\nabla^2 \mathbf{f} = \frac{f_{i+1,j} - 2f_{i,j} + f_{i-1,j}}{\Delta x^2} + \frac{f_{i,j+1} - 2f_{i,j} + f_{i,j-1}}{\Delta y^2},$$

(9.6.1)

where *(i,j)* specify the grid point and Δx and Δy are grid spacing in *x* and *y* directions, respectively. If $\Delta x = \Delta y$ (uniform grid), then Eq. 9.6.1 can be written as:

$$\nabla^2 \mathbf{f} = \frac{1}{\Delta x^2}(f_{i+1,j} + f_{i-1,j} + f_{i,j+1} + f_{i,j-1} - 4f_{i,j}),$$

(9.6.2)

where $2 \leq i \leq m - 1$ and $2 \leq j \leq n - 1$.

Assuming the following ordering of **f** vector elements:

$$\mathbf{f} = [f_{11}, f_{21}, \ldots, f_{m1}, f_{12}, f_{22}, \ldots, f_{m2}, \ldots, f_{mn}]^T,$$

(9.6.3)

the discrete representation of the Laplace operator is:

$$\nabla^2 = \begin{bmatrix} \mathbf{T} & -\mathbf{I} & 0 & \ldots & 0 \\ -\mathbf{I} & \mathbf{T} & -\mathbf{I} & \ldots & 0 \\ 0 & -\mathbf{I} & \mathbf{T} & \ldots & 0 \\ 0 & 0 & -\mathbf{I} & \ldots & 0 \\ \ldots & \ldots & \ldots & \ldots & \ldots \\ 0 & 0 & 0 & \ldots & \mathbf{T} \end{bmatrix},$$

(9.6.4)

where $\mathbf{I}$ is an $m \times m$ identity matrix and $\mathbf{T}$ is the following $m \times m$ matrix:

$$\mathbf{T} = \begin{bmatrix} -4 & -1 & 0 & \ldots & 0 \\ -1 & -4 & -1 & \ldots & 0 \\ 0 & -1 & -4 & \ldots & 0 \\ 0 & 0 & -1 & \ldots & 0 \\ \ldots & \ldots & \ldots & \ldots & \ldots \\ 0 & 0 & 0 & \ldots & -4 \end{bmatrix}.$$

(9.6.5)

10. Afterword

After I finished this book I have had a strong feeling that much more information could still be included, existing chapters could forever be tinkered with and the overall content could be improved. There is always something that could be changed or added. But at some point it is necessary to say *stop.* In fact, the topic of plasma tomography is so wide that it can be divided in a series of monographs. The interested Reader may wish to consult some of books and articles listed in references as further readings.

There is no real ending. It's just the place where you stop the story.

— Frank Herbert

11. References

[Adams 1993] J. Adams et al., Nucl. Instrum. Methods Phys. Res., Sect. A 329, 277 (1993).

[Andersen 1984] A. H. Andersen et al., Ultrason. Imaging, 6, 81 (1984).

[Anderson 2009] I. Anderson et al., Neutron Imaging and Applications - A Reference for the Imaging Community, Springer US (2009).

[Anton 1996] M. Anton et al., Plasma Phys. Control. Fusion 38,1849 (1996).

[Aymar 2002] R. Aymar et al., Plasma Phys. Control. Fusion 44, 519 (2002).

[Barana 2002] O. Barana et al., Rev. Sci. Instrum., 73, 2038 (2002).

[Beckmann 1995] Beckmann et al., Hasylab Annu. Rep. 2, 691 (1995).

[Bielecki 2009] J. Bielecki et al., Acta Phys. Pol. A,115, 537 (2009).

[Bielecki 2012] J. Bielecki et al., Acta Phys. Pol. A 121, 474 (2012).

[Bielecki 2013] J. Bielecki et al., Rad. Phys. Chem. 93, 59 (2013).

[Bielecki 2015] J. Bielecki et al., Rev. Sci. Instrum. 86, 093505 (2015).

[Bielecki 2015b] J. Bielecki et al., Eur. Phys. J. Plus 130 (2015).

[Bielecki 2016] J. Bielecki et al., Fus. Eng. Des.112, 646 (2016).

[Bielecki 2018] J. Bielecki, Fus. Eng. Des.127, 160 (2018).

[Boltruczyk 2017] G. Boltruczyk, et al., Fusion Eng. and Des. 123, 940 (2017).

[Bonse 1965] U. Bonse et al., Appl. Phys. Lett. 6, 155 (1965).

[Brigham 2002] E. Brigham, The Fast Fourier Transform, Prentice-Hall, New York (2002).

[Brown 2003] B. Brown, J. Med. Eng. Technol. 27, 97 (2003).

[Bushong 2014] S. Bushong, Magnetic Resonance Imaging: Physical and Biological Principles, Mosby 4 edition (2014).

[Carvalho 2008] P. Carvalho et al., Rev.Sci. Instr. 79, 10F329 (2008).

[Ceruzzi 2003] P. Ceruzzi, A History of Modern Computing, Second Edition, MIT Press (2003).

[Cormack 1963] A. Cormack, J. Appl. Phys. 34, 2722 (1963).

[Cormack 1973] A. Cormack, Phys. Med. Biol. 18, 195 (1973).

[Craciunescu 2008] T. Craciunescu et al., Nucl. Instrum. Methods Phys. Res., Sect. A 595, 623 (2008).

[Craciunescu 2009] T. Craciunescu et al., Nucl. Instrum. Methods Phys. Res., Sect. A 605, 374 (2009).

[Chugunov 2011] I. Chugunov et al., Nucl. Fusion 51, 083010 (2011).

[Deans 1978] S. Deans, Phys. Med. Biol. 23, 1173 (1978).

[Dickson 1997] D. Dickson, Nature 390, 5 (1997).

[Doyle 1986] E. Doyle et al., Rev. Sci. Instrum. 57, 1945 (1986).

[Ercius 2015] P. Ercius et al., Adv Mater. 27, 5638 (2015).

[Eriksson 2014] J. Eriksson et al., Rev. Sci. Instrum. 85, 11E106 (2014).

[Feldkamp 1984] L. Feldkamp et al., J. Opt. Soc. Amer. 6, 612 (1984).

[Fessler 2014] J. Fessler, Reference Module in Biomedical Sciences Comprehensive Biomedical Physics in Comprehensive Biomedical Physics, 2 (2014).

[Fischer 2008] B. Fischer at al., Inverse Probl. 24, 034008 (2008).

[Gemmeke 2007] H. Gemmeke et al., Nucl. Instrum. Methods Phys. Res., Sect. A 580, 1057, (2007).

[Giacomelli 2014] L. Giacomelli et al., Rev. Sci. Instrum. 85, 023505 (2014).

[Gnesin 2008] S. Gnesin et al., Rev Sci Instrum. 79,10F504 (2008).

[Godel, 1931] K. Gödel, Monatshefte für Mathematik Physik, 38, 173 (1931).

[Golub 1979] G. Golub et al., Technometrics, 21, 215 (1979).

[Goswami 2014] M. Goswami, Fus. Eng. and Des. 89, 2659 (2014).

[Gowers 2002] C. Gowers, et al., Advanced Diagnostics for Magnetic and Inertial Fusion, Springer, US, (2002).

[Granetz 1985] R. Granetz et al., Nucl. Fusion 25, 727 (1985).

[Granetz 1988] R. Granetz et al., Nucl. Fusion 28, 457 (1988).

[Hadamard 1902] J. Hadamard, Princeton University Bulletin, 13, 49 (1902).

[Hamacher 2001] T. Hamacher et al., Fusion as a Future Power Source: Recent Achievements and Prospects, Proceedings of the 18th World Energy Congress (2001).

[Hansen 1992] P. Hansen, SIAM Rev. 34, 561 (1992).

[Hashemi 2003] R. Hashemi, William G. Bradley, Christopher J. Lisanti MRI: The Basics Lippincott Williams & Wilkins, Edition 2, (2003).

[Hasting 1970] W. Hasting, Biometrika 57, 97 (1970).

[Helgason 1999] S. Helgason, The Radon Transform in Progress in Mathematics, Birkhäuser Basel, (1999).

[Horowitz 2014] J. Horowitz, Annu. Rev. Econ. 6, 21 (2014).

[Hsiao 2001] C. Hsiao et al., J. Comput. Phys. 173, 433 (2001).

[Ingesson 1998] L. Ingesson et al. Nucl. Fusion, 38, 1675 (1998).

[Iwama 1989] N. Iwama et al., Appl. Phys. Lett. 54, 502 (1989).

[Jacquinot 1991] J. Jacquinot, Plasma Phys. Control. Fusion 33, 1657 (1991).

[Jardin 2016] A. Jardin et al., Phys. Scr. 91, 044007 (2016).

[Johnston 2017] H. Johnston, Phys. World 30, 11 (2017).

[Kaczmarz 1937] S. Kaczmarz, Bull. Int. Acad. Polon. Sci. Lett. Ser. A, 35, 335 (1937).

[Kak 2001] A. Kak and M. Slaney, Principles of Computerized Tomographic Imaging, Society of Industrial and Applied Mathematics (2001).

[Kazakov 2015] Y. Kazakov et al., Nucl. Fusion 55, 032001 (2015).

[Kazakov 2017] Y. Kazakov et.al., Nature Physics 13, 973 (2017).

[Kihm 1996] K. Kihm et al., Exp. Fluids. 22, 137 (1996).

[Kiptily 2005] V. Kiptily et al., Nucl. Fusion 45, L21 (2005).

[Kiptily 2006] V. Kiptily et al., Plasma Phys. Control. Fusion 48, R59 (2006).

[Kitchen 2007] M. Kitchen, Phys Med Biol., 52, 4171 (2007).

[Konoshima 2001] S. Konoshima et al., Plasma Phys. Control. Fusion 43, 959 (2001).

[Lavrent'ev 1986] M. Lavrent'ev, et al., Ill-posed problems of mathematical physics and analysis, Amer. Math. Soc. (1986).

[Lawson 1957] J. Lawson, Proceedings of the Physical Society B 70, 6 (1957).

[Lee 2010] S. Lee et al., Curr. Appl. Phys. 10, 893 (2010).

[Lee 2014] S. Lee et al., Rev. Sci Instrum. 85, 11E827 (2014).

[Loffelmann 2016] V. Loffelmann et al., Fusion Sci. Technol. 69, 505 (2016).

[Mantsinen 2002] M. Mantsinen et al., Phys. Rev. Lett. 89, 115004 (2002).

[Maslov 2013] M. Maslov et al., J. Instrum. 8, C11009 (2013).

[Matos 2017] F. Matos at al., Fus. Eng. Des. 114, 18 (2017).

[Mazon 2008] D. Mazon et al., Rev. Sci. Instrum. 79, 10E321 (2008).

[McCall 2005] J. McCall, J. Comput. Appl. Math. 184, 205 (2005).

[Metropolis 1953] N. Metropolis et al., Journal of Chemical Physics, 21 1087 (1953).

[Miller 2004] G. Miller et al., Nucl. Fusion 44, S228 (2004).

[Mlynar 2012] J. Mlynar et al., Rev. Sci. Instrum. 83, 10E531 (2012).

[Momose 1995] A. Momose, Med. Phys. 22, 375 (1995).

[Momose 2006] A. Momose, Japanese Journal of Applied Physics, 45, 5254 (2006)

[Morozov 1984] V. Morozov, Methods for solving incorrectly posed problems, Springer (1984).

[Neu, 2009] R. Neu et al., Phys. Scr. 2009, 014038 (2009).

[Nocente 2013] M. Nocente et al., IEEE Trans. Nucl. Sci. 60, 1408 (2013).

[Noterdaeme 2008] J. Noterdaeme, et al., Fusion Sci. Tech. 53, 1103 (2008).

[NPL 2017] National Physical Laboratory, Kaye&Laby. Tables of Physical & Chemical Constant, Chapter 4, Section 4.7, Subsect. 4.7.4 Nuclear Fusion. Available online: http://www.kayelaby.npl.co.uk/atomic_and_nuclear_physics/4_7/4_7_4.html (accessed on 23 November 2017).

[Nugent 2007] K. Nugent, J. Opt. Soc. Am. A 24, 536 (2007).

[O'Brien 1992] D. O'Brien et al., Nucl. Fusion 32, 1351 (1992).

[Odstrčil 2016] T. Odstrčil, Rev. Sci.Instr. 87, 123505 (2016).

[Olmi, 2000] R. Olmi et al., IEEE Trans. Evolut. Comput., 4, 83 (2000).

[Ongena 2016] J. Ongena et al., Nature Physics 12, 398 (2016).

[Perrone 2014] A. Perrone et al., Earth-Science Reviews 135, 65 (2014).

[Petrizzi 2007] L. Petrizzi et al., Fusion Eng. and Des. 82, 1309 (2007).

[Peysson 2001] Y. Peysson et al., Nucl. Instrum. Methods Phys. Res., Sect. A 458, 269 (2001).

[Ramachandran 1971] G. Ramachandran et al., Proc. Nat. Acad. Sci. 68, 2236 (1971).

[Riva 2007] M. Riva et al., Fus. Eng. and Des. 82, 1245 (2007).

[Riva 2017] M. Riva et al., Fus. Eng Des. 123, 873 (2017).

[Ronchi 2010] E. Ronchi et al., Nucl. Instrum. Methods Phys. Res. A 613, 295 (2010).

[Shepp 1974] L. Shepp et al., IEEE Trans. Nucl, Sci. 21, 21 (1974).

[Shevelev 2013] A. Shevelev et al., Nucl. Fusion 53, 123004 (2013).

[Stix 1992] T. Stix, Waves in plasmas, AIP, New York, (1992).

[Swinhoe 1984] M. Swinhoe et al., Nucl. Instrum. Methods Phys. Res. 221, 460 (1984).

[Tanabe 1971] K. Tanabe et al., Numer. Math. 17, 203 (1971).

[Terasaki 1999] N. Terasaki, et al., Systems and Computers in Japan 30, 85 (1999).

[Teukolsky 2007] W. Teukolsky, et al., Numerical Recipes: The Art of Scientific Computing, 3rd ed., Cambridge University Press, New York, (2007).

[Tikhonov 1943] A. Tikhonov, Об устойчивости обратных задач (On the stability of inverse problems), Doklady Akademii Nauk SSSR, 39, 195 (1943).

[Turing 1936] A. Turing, Proceedings of the London Mathematical Society, Series 2, 42 230, (1936).

[Tuy 1983] H. Tuy, SIAMJ. Appl. Math 43, 546 (1983).

[Vezinet 2014] D. Vezinet et al., Nucl. Fusion 54, 083011 (2014).

[Wakatani, 1998] M. Wakatani, Stellarator and Heliotron devices, Oxford University Press, New York and Oxford (1998).

[Waterstram-Rich 2016] K. Waterstram-Rich et al., Nuclear Medicine and PET/CT - Technology and Techniques, Elsevier Health Sciences (2016).

[Wernick 2004] M. Wernick, et al., Emission Tomography - The Fundamentals of PET and SPECT, Academic Press (2004).

[Westbrook 2011] Catherine Westbrook et al., MRI in Practice, Wiley-Blackwell; 4th Revised edition (2011).

[Wingen 2015] A. Wingen et al., J. Comput. Phys. 289, 83 (2015).

[Xu 2012] L. Xu et al., Phys. Plasmas 19, 122504 (2012).

[Xu 2016] Y. Xu et al., Meas. Sci. Technol. 27 114002 (2016).

[Yang 2014] X. Yang et al., Powder Technol. 253, 626 (2014).

[Zaprazny 2012] Z. Zaprazny, et al., J. Instrum. 7, C0300 (2012).

[Zhdanov 2002] M. Zhdanov, Geophysical Inverse Theory and Regularization Problems. In Ser. Methods in Geochemistry and Geophysics 36, Elsevier, Amsterdam (2002).

[Zychor 2016] I. Zychor et al., Phys. Scr. 91 064003 (2016).